TUDelft

THESIS

Reduction of Cross Polarization Level in Connected Slot Arrays using Artificial Dielectric Layers with Vertical Metallic Inclusions.

Caspar G. van Wamel

October 30, 2020 - July 15, 2021

Reduction of Cross Polarization Level in Connected Slot Arrays using Artificial Dielectric Layers with Vertical Metallic Inclusions.

Reduction of Cross Polarization Level in Connected Slot Arrays using Artificial Dielectric Layers with Vertical Metallic Inclusions

by

Caspar Gerardus van Wamel

to obtain the degree of MASTER OF SCIENCE
at the Delft University of Technology,
to be defended publicly on Thursday July 15, 2021 at 09:00.

i

Contents

Chapter 1

Introduction

1.1 The Need for Wideband Wide-Scan Arrays

The need for phased array antennas is expanding in modern society. Besides the long-lasting widespread employment in military radar systems, more recently phased arrays are finding use also in communication systems, e.g. for satellite data links [1] and 5G wireless networks [2]. These applications can benefit from the key advantages of phased arrays, such as high gain, agile beam steering, multi-beam capability, low profile and conformability to platform dimensions. However, for both radar and communication applications, a major bottleneck has become the limited space available on the platforms to host a large number of antennas required for different functions.

More specifically, to meet the progressively more stringent requirements in the area of radar surveillance and tracking, modern military ships and aircrafts are populated by an ever increasing number of sensors. The installation of a large number of antennas systems not only increases the cost and weight, but also becomes impractical in environments where there is limited space at hand. The evolving role of small platforms also dictate a shrinkage of the space available for each antenna system (e.g., the increased use of unmanned aerial vehicle and small drones with similar capabilities of larger aircrafts). Also commercial applications, like wireless communications, promise to provide a range of services that use several different frequency bands within the electromagnetic spectrum. Given the severe space and cost constraints, it is challenging or even unfeasible to incorporate many narrow-band arrays, each covering a different function and/or frequency band, on the same platform.

To overcome this problem, there has been a growing interest, in the last decade, in the development of phased-array antennas with very large frequency range of operation and good scan performance over wide angular ranges. An antenna system with such characteristics can support multi-functional operation and combine different radar and communication functions in a single radiating aperture, allowing to reduce the total number of antennas on complex military platforms [3,4]. Similarly, for wireless communications, an ultra-wideband array can cover simultaneously different bands. These ultra-wideband arrays provide a significant reduction of the overall cost and also reduce the volume required. Besides the broad bandwidth, these antennas are typically required to steer their beam over a wide field of view with minimal performance degradation.

In this thesis, the considered application is satellite communication (satcom), for which it is favorable to use a wideband array covering simultaneously different bands, especially for aircraft
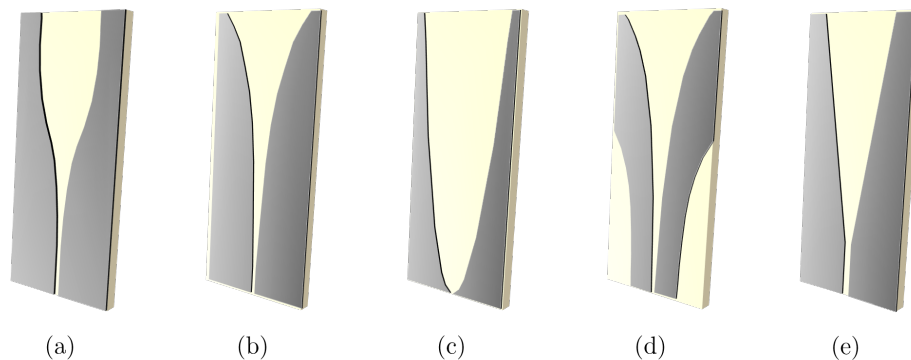
Figure 1.1: Differently shaped tapered-slot antennas: (a) Nonlinear taper, (b) Exponential taper (Vivaldi), (c) Fermi or Parabolic taper, (d) Dual exponential taper, (b) Linear taper.

terminal antennas. The work described here refers to a satcom antenna array covering both the Ku- and the Ka-transmit [5], for in-flight entertainment applications via satellite. This antenna should also be able to scan to very large angles (at least $\pm$ 60 degrees), to guarantee agile connections to different satellites.

1.2 State of the Art

Several solutions have been proposed to realize wideband wide scan arrays. The state-of-the-art designs can be grouped into two large families: (1) tapered slot antenna arrays and (2) connected arrays, also referred to as tightly-coupled arrays.

1.2.1 Tapered Slot Arrays

Tapered slot and flared notch antenna arrays have been successfully used as ultra-wideband phased arrays for over four decades due to their excellent matching performance, simple feeding and well-known design guidelines [6–15]. Although different flaring profile of the slots have been investigated (Fig. 1.1), the most common elements are Vivaldi antennas, which indicate exponentially tapered slot antennas.

Typical implementation of dual-polarized Vivaldi arrays involve complex assembly of a set of vertical printed circuit boards (PCBs) intersecting in an egg-crate configuration, as shown in Fig. 1.2(a). For this reason, alternative all-metal implementations have been proposed, based on metal machining in [13] (see Fig. 1.2(b)) or body of revolution elements in [11].

However, tapered slot and flared notch arrays are characterized by large vertical dimension compared to the wavelength. The bandwidth of the array can be enlarged by increasing the length of the antenna elements, but elements pattern may suffer from scan blindness due to common-mode resonances propagating on the flared vertical edges [16]. Another drawback of this type of arrays is the relatively high cross polarization when scanning in the diagonal planes [17–19]. The high cross-polar levels of the radiated field originate from the vertical component of the current distribution propagating on the flared edges of the tapered slot.
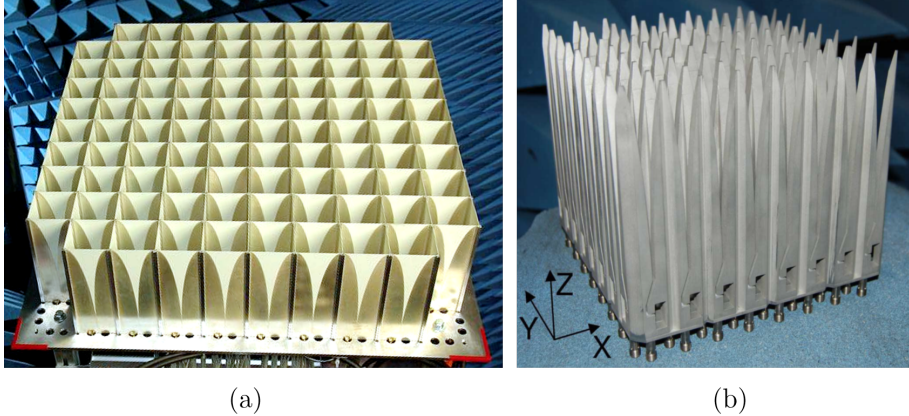
2

Figure 1.2: 8x8 dual-polarized planar array of flared-notch antennas: (a) vertical PCB arrangement [20] and (b) all-metal implementation [13].

Vivaldi arrays with reduced cross-polarization have been recently proposed in [21]. However, this design is still based on a vertical and electrically long PCB, resulting in a high profile and a complex and costly assembly.

1.2.2 Connected Arrays

The second large category of wideband arrays is referred to connected or tightly-coupled array. This concept finds its origin in the current sheet array proposed by Wheeler in [22]. The Wheeler current is an infinite planar current distribution with constant amplitude and linear phase. Since the phase variation is continuous, the Wheeler current is equivalent to a phased array where the inter-element spacing is infinitely small. Such ideal current, when radiating in free space, exhibits an input impedance that is frequency independent and varies with the scan angle θ directly or inversely proportional to $\cos \theta$ for scanning in the E- and H-plane, respectively.

The first connected array was introduced by Baum in 1999 [23]. He was studying the radiation from an array of bow-tie dipoles, where each element was electrically connected to the neighboring elements, i.e. the arms of the adjacent dipoles are touching. He showed that such an array could achieve a huge bandwidth and could be used to transmit very short time-domain pulses without adding distortion. The array of Baum effectively implemented an approximation of the Wheeler current.

Another attempt to realize a Wheeler current sheet was given by Munk [24], who initiated a parallel development in this field. The idea was to use arrays of dipoles that were strongly coupled to each other by means of a capacitance, rather than electrically connected. The role of the capacitance is similar to the electrical connection between elements, i.e. it allows the current to flow from one element to the neighboring one. In fact, "connected arrays" are often also referred to as "tightly coupled array" and these terms can be essentially used as synonyms.

The term "connected array" was introduced for the first time by R.C. Hansen in [25]. He studied the current distributions in linear arrays of dipoles when the edges are connected. The first important study on the theory of connected arrays was presented in [26] by Neto and Lee. They
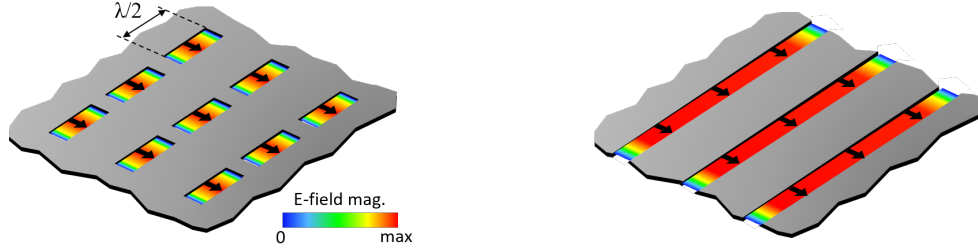
3

Figure 1.3: (a) A resonant conventional array of slots and (b) a connected slot array [5]

derived closed form expressions for the impedance of connected arrays of slots based on spectral methods, showing that the bandwidth is theoretically "infinite" for periodic arrays in free space.

For a long time, conventional array design was based on optimizing first the performance of a single antenna element in isolation, and then using this element in array configuration, trying to minimize mutual coupling. If the mutual coupling is very low, the element in array configuration would behave similarly to the isolated element. This approach has been completely changed with the introduction of connected arrays. The idea in connected arrays is to intentionally increase mutual coupling between array elements to provide wideband operation.

In arrays of resonant slots, as in Fig. 1.3(a), the electric field distribution on the slots is sinusoidal and frequency dependent. The antennas radiate efficiently only at the frequency at which they are half wavelength, thus they are narrow-band. Connected arrays are obtained by electrically connecting the slots, as shown in Fig. 1.3(b). This creates arrays of long slots, fed at periodic locations. Since the elements are not truncated, the field distributions remain nearly constant with the frequency, resulting in wideband behavior. Moreover, since the currents are planar and do not have vertical components as in Vivaldi arrays, connected arrays can achieve better cross polarization.

Designs of tightly-coupled dipole arrays have been demonstrated in [27–29]. However, most of these designs are also based on array configurations similar to Vivaldi arrays, where the radiating elements and the feed structures are printed on vertical (PCBs). The vertical PCB construction is functional to the realization of the feed lines, which are too long to be realized through standard via-hole technology.

A planar implementation of the array can greatly reduces cost and complexity of the array. For this reason, there have been attempts to realize planar connected arrays, where only a single multi-layer horizontal PCB is used for the entire dual-polarized array [30], [31]. To enable the planar implementation, the distance between the radiating elements and the ground plane has to be reduced to realize the feed lines with vias. Unfortunately, reducing the distance from the ground plane causes a degradation of the bandwidth and the scanning performance.

To greatly increase the frequency range, the array can be loaded with one or multiple dielectric slabs that reduce the resonance effects of the ground plane, by enhancing the upward radiation. However, dielectric slabs are known to support surface waves that would cause efficiency loss and scan blindness. To solve the surface-wave problem, artificial dielectrics were used in place of real dielectrics in [32], [33]. This results in the concept of connected slots with artificial dielectric layers, which will be described in the next section and will considered as the antenna element for the design presented in this thesis.
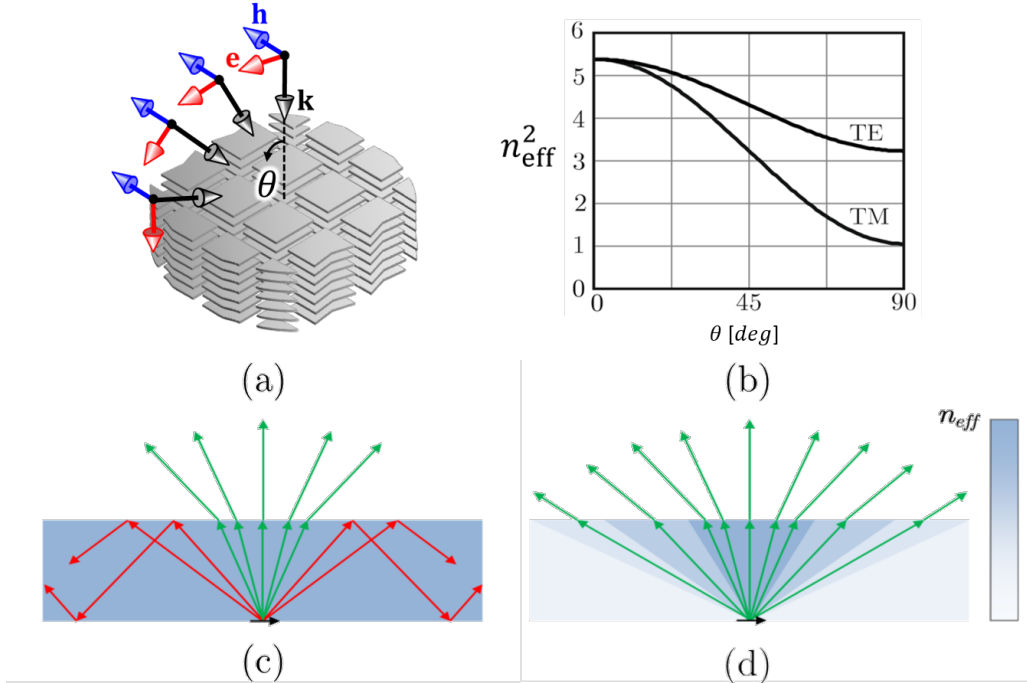
4

Figure 1.4: (a) schematic view of ADL layer with (b) a impression of the refraction index for transverse electric (TE) and transverse magnetic (TM) incident wave, in (c) a dielectric with a surface wave in contrast to (d) an ADL which suppresses the surface wave.

1.2.3 Connected Slot Array with Artificial Dielectric

Recently, a novel concept has been developed at TU Delft [32], [33], to improve the performance of wideband wide-scan phased arrays, while reducing the costs and complexity of the array: this consists of a connected slots with artificial dielectric layers (ADLs).

An artificial dielectric (AD) comprises of periodic metallic patches, which are small with respect to the wavelength, placed horizontally in a host material(Fig. 1.4(a)). These horizontal inclusions can be implemented as one layer or multiple stacked layers. The aim of the artificial dielectric layer (ADL) is to create an equivalent material with modified properties. The equivalent electromagnetic parameters of the artificial material can be designed by properly determining the spatial density of the horizontal metallic patches. An AD offers one main advantage over real dielectric which is the anisotropy, i.e. the effective refractive index of the ADLs decreases with the angle of incidence of a plane wave propagating through the material, as shown in Fig. 1.4(b). This key property results in a structure with a suppression of the excitation of surface waves. An isotropic dielectric slab supports surface waves when it is placed above a radiating array while scanning. The surface wave is caused by the total internal reflection at the top surface of the slab(Fig. 1.4(c)). On the contrary, ADL slabs exhibit a lower and lower permittivity for increasing angles of incidence, in order for the critical angle never to occur at their interface with free space (Fig. 1.4(d)). This in turn prevents scan blindness even at large scan angles.
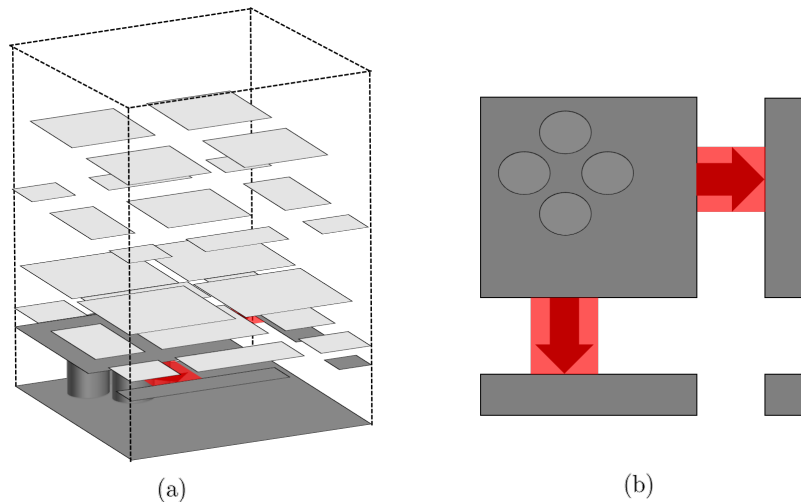
5

Figure 1.5: Dual-polarized connected slot array with a Artificial dielectric (a) unit cell sketch and (b) slot plane two dimensional sketch designed in [5]

The overall array unit cell is schematically shown in Fig. 1.5. The radiating element is a dual-polarized connected slots excited with a delta gap generators and backed by a grounded slab. Vias are placed in the slab to avoid the propagation of modes guided between the slot plane and the backing reflector. To compensate for the frequency dependence due to the distance to the backing reflector, ADLs are placed above the slot. The ADLs are fabricated to achieve an gradually decreasing refractive indices and are engineered for the implementation of wideband matching between the antenna feed and free space. The artificial dielectric solutions demonstrated a very wide bandwidth, with stable active impedance within a scan range exceeding ±60 degrees.

However, artificial dielectrics generate high cross-polarization (X-pol) in the radiated signals, when used over ultra-wide bandwidths. The polarization purity is an important requirement in communication applications, especially when using a dual-polarized array that is required to operate in circular or slant linear polarization. The design in [1], aiming at covering simultaneously the Ku- and Ka- satcom transmit bands, was shown to achieve a cross polarization level as high as -5 dB, when scanning in the diagonal plane (D-plane, azimuth plane $\phi = 45°$) to $\theta = 60°$.

One approach to reducing the cross polarization level is to combine the feed of the two orthogonal slots with proper weights to cancel the cross polarization for a certain frequency and scan angle [5]. This requires calibration lookup tables for adjusting beamforming weights on dual-polarized element channels to correct polarimetric beam properties. Despite the cancellation was shown to be effective, the high intrinsic cross-polarization of connected slots with artificial dielectrics remains the main limitation of this concept. In fact, a lower intrinsic cross-polarization would result in simpler calibration procedures or could allow the transmission of two independent data streams doubling the capacity in communication applications.

1.3 Objective of the Thesis

The main goal of this thesis is to introduce a new class of artificial dielectrics, with non-uniform or non-planar characteristics, with the goal of reducing the cross polarization. Unlike the ADLs used in previous designs, which only considered horizontal patches, here vias are included in the structure to support vertical currents. The introduction of the vertical wires gives an additional degree of freedom to control effective tensor permittivity of the artificial dielectric.

An investigation of the cross-polarization properties of connected arrays with artificial dielectrics is carried out in the thesis, with emphasis on the comparison between connected slots and dipoles. Both homogeneous isotropic dielectrics and artificial dielectrics are considered in the analysis. It is shown that artificial dielectric, because of their different behavior under transverse electric (TE) and transverse magnetic (TM) plane-wave incidence, yield increased levels of X-pol when compared with isotropic homogeneous dielectrics. The vertical wires are used to increase the z-component of the equivalent permittivity tensor, resulting in more similar effective TE and TM refractive index, and in turns in a lower X-pol.

As an example, to validate the concept, the unit cell introduced in [1] is considered. This consists of an array with a wide bandwidth exceeding 2:1, from 13.75 GHz to 31 GHz, to accommodate both the Ku- and Ka- satcom transmit bands. Different designs of the ADLs, with and without vias, are presented and compared to demonstrate the effectiveness of the vias in reducing the X-pol.

Moreover, an optimization of the unit cell is performed in this work, that advances the preliminary design in [1]. The optimization involves the inclusion of realistic materials for the fabrication, such as dielectric and bonding layers in the ADL and in the slot array PCBs, and the modification of the geometrical parameters in accordance with manufacturing constraints. The modified stratification also require a fine tuning of the feeding structure.

1.4 Outline of the Thesis

In **chapter 2** the concept of connected slot arrays and artificial dielectric layers is discussed. The analytical expressions are presented for both the connected slot array and the artificial dielectric layer. In addition, the incorporation of a backing reflector in the model with vertical walls is described. In **chapter 3** a study on cross polarization level is performed of connected slot and connected dipole arrays. Moreover, the addition of dielectric superstrates and substrates is discussed. Lastly in chapter 3, the impact of the use of artificial dielectrics on the cross polarization is presented along with an indication on the method of reducing the cross polarization. In **chapter 4** a Method of Moments(MoM) analysis for vertical rods is performed in order to reduce the cross polarization level. Moreover, the relations between the parameters of the wire and the z-component of the permittivity tensor are described. For practical implementation of the wire medium into the ADL a new category of the wire medium is introduced: the Top-hat loaded wire medium. Finally, the wire medium is implemented in an example to show its effectiveness. In **chapter 5** a design of a connected slot array for communication in the Ku- and Ka-frequency band is shown with a reduced cross polarization level. In addition to the implementation of the wire medium, a dielectric slab is introduced in the ADL. In order to be able to manufacture the array, the unit cell design is adapted for fabrication by PCB methods with realistic materials. Lastly, **chapter 6** provides a conclusion on the cross polarization and the use of the wire medium. It also offers recommendations for future work.

Chapter 2

Connected Slot Arrays and Artificial Dielectrics

2.1   Connected Slot Array

As described in chapter 1, connected arrays offer a good solution to realize wideband arrays. Analytical expressions for the active input impedance of connected arrays were derived in [26, 34]. In this section the main expressions used for the modeling and the design of the unit cell are reported.

2.1.1   Connected Slot Active Input Impedance

The geometry of a connected slot array is shown in Fig. 2.1. The array is infinitely periodic in both $\hat{x}$ and $\hat{y}$, it is build up out of unit cells with a size of $d_x = d_y$ and each unit cell contains one δ-gap feed with a length of δ_s. The width of the slot is defined by w_s.
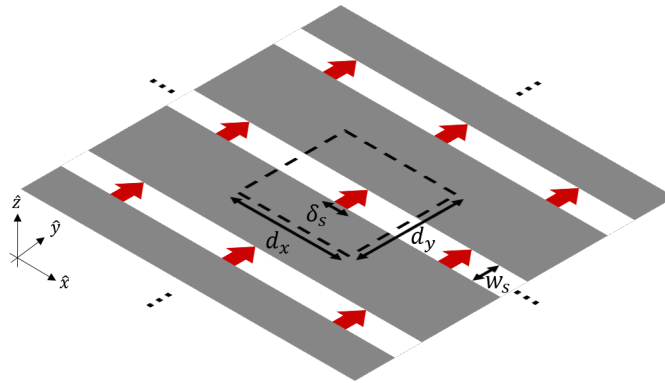

Figure 2.1: Geomerty of connected slot array.

The active input impedance at one of the feeding gaps can be expressed as a spectral Floquet expansion [35]:

$$Z_a = -\frac{1}{d_x} \sum_{m_x=-\infty}^{\infty} \frac{\text{sinc}\left(\frac{k_{xm}\delta_s}{2}\right)^2}{D_\infty(k_{xm})} \tag{2.1}$$

where $k_{xm} = k_{x0} - (2\pi m_x)/dx$ are the Floquet wavenumbers with indexes m_x, to account for the periodicity along the x-axis, and $k_{x0} = k\sin\theta\cos\phi$ if the array is scanning to the angular direction θ,ϕ. The function at the numerator $\text{sinc}(k_{xm}\delta_s/2)$ represent the Fourier transform of the impressed electric field in the slot, which is constant over the region of the feed, according to the delta-gap generator assumption. The function $D_\infty(k_{xm})$ represents the longitudinal connected array Green's function [36] that accounts for the infinite periodicity of the slots in the y-direction and can be written as the following Floquet mode expansion:

$$D_\infty(k_{xm}) = \frac{1}{d_y} \sum_{m_y=-\infty}^{\infty} G_{xx}(k_{xm}, k_{ym}) J_0\left(\frac{k_{ym}w_s}{2}\right) \tag{2.2}$$

where $k_{ym} = k_{y0} - (2\pi m_y)/dy$ are the Floquet wavenumbers with indexes m_y, to account for the periodicity along the y-axis, with $k_{y0} = k\sin\theta\sin\phi$. G_{xx} is the xx-component of the spectral dyadic Green's function, that account for the generic medium stratification along z, and relates the radiated magnetic field to the magnetic sources. The Bessel function of the first kind of order zero J_0 is the Fourier transform of the transverse distribution of the magnetic current on the slot, assumed to be edge singular.

The spectral Green's function can be found as a function of the current solutions I_{TE} and I_{TM} of the transmission line models representing the stratified medium above and below the slot plane, for transverse electric (TE) and transverse magnetic (TM) modes, respectively [37]:

$$G_{xx}(k_x, k_y) = G_{xx}^{up}(k_x, k_y) + G_{xx}^{down}(k_x, k_y) = -\frac{I_{TE}^{up}k_x^2 + I_{TM}^{up}k_y^2}{k_x^2 + k_y^2} - \frac{I_{TE}^{down}k_x^2 + I_{TM}^{down}k_y^2}{k_x^2 + k_y^2} \tag{2.3}$$

For the calculation of the active impedance, the currents can be found as the inverse of the transmission line input impedance for the stratification above and below the slot, i.e. $I_{TE}^{up} = 1/Z_{TE}^{up}$, $I_{TM}^{up} = 1/Z_{TM}^{up}$, $I_{TE}^{down} = 1/Z_{TE}^{down}$, $I_{TM}^{down} = 1/Z_{TM}^{down}$. The transmission lines for TE and TM components have characteristic impedances $Z_{0TE} = \zeta k/k_{zm}$ and $Z_{0TM} = \zeta k_{zm}/k$, respectively, and propagation constant $k_{zm} = (k^2 - k_{xm}^2 - k_{xm}^2)^{1/2}$, with ζ being the medium impedance.

2.1.2 Example of Validation

As an example of validation for the given expressions for the active input impedance, a simulation of the unit cell is performed with a commercial full wave solver. For a connected slot unit cell in free space is considered, with the parameters $w_s = 0.1\lambda_0$, $\delta_s = 0.1\lambda_0$, $d_x = d_y = 0.5\lambda_0$, with λ_0 being the wavelength at the frequency $f_0 = 10$ GHz. In Fig. 2.2(a) the input impedance for broadside is shown, while in Fig. 2.2(b) the input impedance refers to scanning to $\theta = 60°$ in the H-plane ($\phi = 0°$). The analytical spectral equations and the simulations agree well, however while scanning some oscillations are observed in the input impedance from the commercial solver. Those
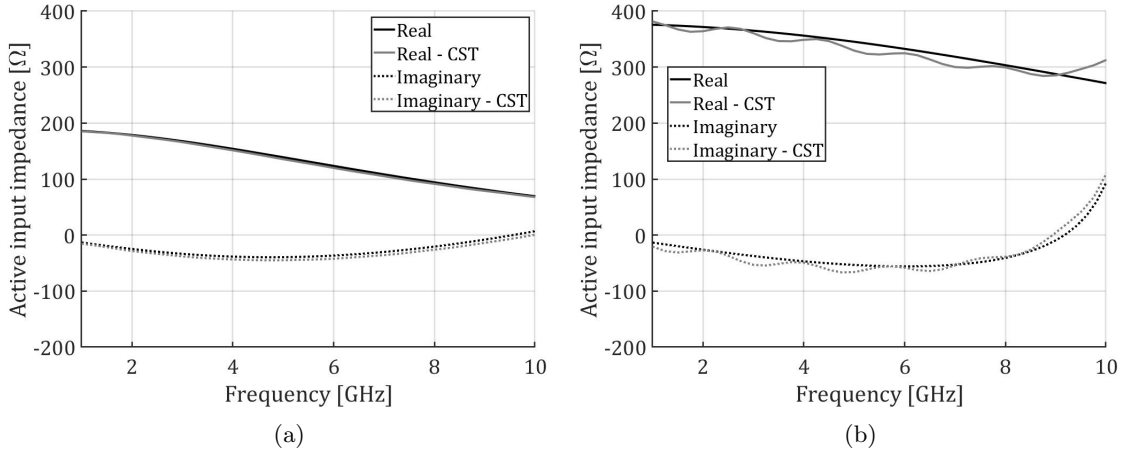
Figure 2.2: Input impedance of connected slot array in free space with $w_s = 0.1\lambda_0$, $\delta_s = 0.1\lambda_0$, $d_x = d_y = 0.5\lambda_0$ for (a) broadside and (b) scanning to $\theta = 60°$ in the H-plane.

oscillations are introduced by the set-up in the solver and are thus an artifact of the simulation, often related to a non perfectly absorbing boundary conditions for large-angle oblique incidence.

Finally, the active reflection coefficient is obtained with a known line impedance, Z_{line}, feeding the infinite slot array, as

$$\Gamma_a = \frac{Z_a - Z_{line}}{Z_a + Z_{line}} . \tag{2.4}$$

Although the example of validation is done for free space, the expressions are valid for any generic dielectric stratification, which can be accounted for by changing only the spectral Green's function computation in Equation 2.3.

2.2 Artificial Dielectric Layers

As introduced in the Chapter 1, artificial dielectric layers (ADLs) are multi-layer structures comprising of a host medium filled with periodic horizontal metallic patches that are small compared to the wavelength. Analytical expressions for the aligned ADLs were derived in [38,39], see Fig. 2.3(a). The method has also evolved to include nonaligned layers [40], as depicted in Fig. 2.3(b). The shift between layers has the advantage that less layers can be used to obtain the same effective permittivity, compared to the aligned case. In addition, a spectral domain method to describe non-aligned and non-periodic patches was derived in [41], as shown in Fig. 2.3(c). This last solution is reported here.

2.2.1 Analytical Model for Non-Periodic ADLs

An ADL slab consists of a host medium with N metal layers. Each layer is a periodic square lattice of PEC patches, but the geometrical parameters of each layer can be different, as in Fig. 2.3(c).
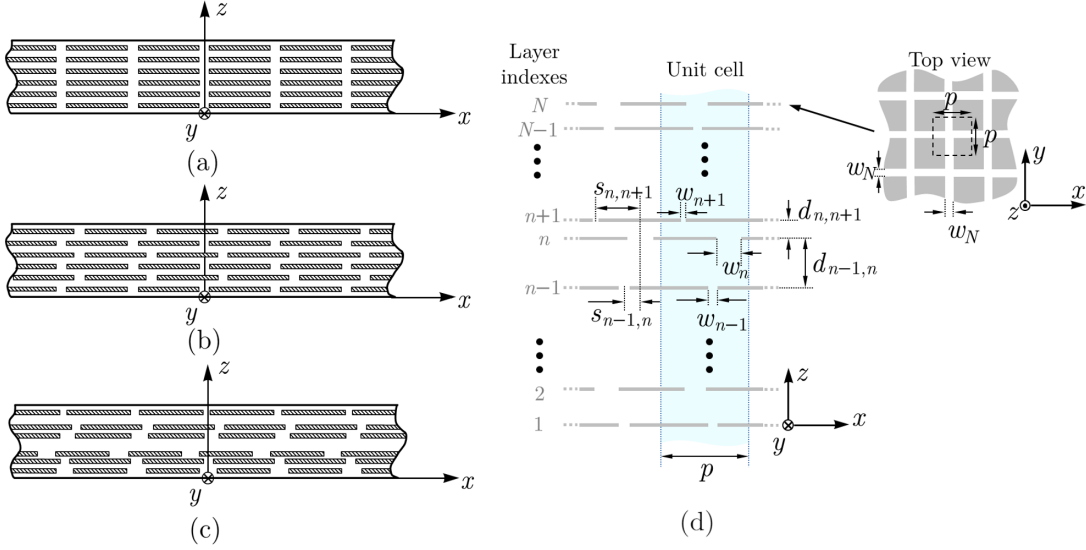
10

Figure 2.3: Two dimensional artificial dielectric layer arrangements (a) aligned (b) shifted and (c) non periodic layers and (d) an overview of all parameters [40].

More in detail, the structure under analysis is shown in Fig. 2.3(d). The different layers are indicated by an index ranging from 1 to N. Each metal patch is infinitely thin, thus it has no currents in the z-direction. For this analysis it is also assumed that the ADL is infinitely large, with the patches periodic in the square lattice along $\hat{x}$ and $\hat{y}$ with the same period p. The patches of the n-th layer have a, edge-to-edge distance of w_n between them, which is equal for the $\hat{x}$ and $\hat{y}$ directions. This distance is also referred to as the gap width. Additionally, each layer can have a shift with respect to the previous, $s_{n,n-1}$, and to the next layer, $s_{n,n+1}$, as show in Fig. 2.3(d). Lastly, each layer has a distance to the previous, $d_{n,n-1}$, and to the next layer, $d_{n,n+1}$, except the first and the Nth layers, which will be discussed separately. New in [41] compared to the previous formulations is the possibility for the shift and the distance between layers to be non-periodic, i.e., in general $s_{n,n-1} \neq s_{n,n+1}$ and $d_{n,n-1} \neq d_{n,n+1}$.

Following the procedure in [41], the equivalent susceptance of the internal n-th ADL layer is given by

$$
\begin{aligned}
B_n = \frac{jp\varepsilon_{host}}{\zeta_0 \lambda_0} \sum_{m \neq 0} &[S_m(w_n)\left(f_m(d_{n,n+1}) + f_m(d_{n-1,n})\right) \\
&+ S_m(w_{n+1})g_m(s_{n,n+1}, d_{n,n+1} + S_m(w_{n-1})g_m(s_{n-1,n}, d_{n-1,n})]
\end{aligned}
\tag{2.5}
$$

where ε_{host} is the relative permittivity of the medium surrounding the layer and the functions $S_m(w)$, $f_m(d)$ and $g_m(s,d)$ are defined as

$$
S_m(w) = \frac{\left|\text{sinc}\left(\frac{\pi m w}{p}\right)\right|^2}{|m|}
\tag{2.6}
$$

11

$$f_m(d) = -\cot\left(-\frac{2j\pi|m|d}{p}\right) \tag{2.7}$$

$$g_m(s,d) = e^{\frac{j2\pi ms}{p}}\csc\left(-\frac{2j\pi|m|d}{p}\right). \tag{2.8}$$

This procedure provides a large flexibility in the design of these ADL slabs, although it still dictates that the period of the patches in the ADL, p, is equal for all layers in the slab. Lastly, the first and last layer only have adjacent layers on one side, therefore the susceptance of the first and last layers become

$$B_1 = \frac{jp\varepsilon_{host}}{\zeta_0\lambda_0}\sum_{m\neq 0}[S_m(w_1)\left(f_m(d_{1,2})-j\right)+S_m(w_2)g_m(s_{1,2},d_{1,2})] \tag{2.9}$$

$$B_N = \frac{jp\varepsilon_{host}}{\zeta_0\lambda_0}\sum_{m\neq 0}[S_m(w_N)\left(-j+f_m(d_{N-1,N})\right)+S_m(w_{N-1})g_m(s_{N-1,N},d_{N-1,N})]. \tag{2.10}$$

Note that the result for the bottom and top layer can be also obtained by taking the expression of the inner layers and setting one of the distance to the next or previous layers to ∞. The function in Equation 2.7 becomes $\lim_{d\to\infty}f_m(d) = -j$ and the function in Equation 2.8 results in $\lim_{d\to\infty}g_m(s,d) = 0$.

All the formulas for the layer susceptance include the interaction between layers due to higher-order Floquet modes, thus remain valid for arbitrarily small electrical distance between layers. When a generic plane wave is incident on the multi-layer artificial dielectric, the equivalent transmission lines for the TE and TM components can be constructed as shown in Fig. 2.4.

For this procedure the susceptance of the layer is only related to the capacitive and reactive effects of the layer, therefore the Floquet modes for the susceptance is an infinite sum not including the fundamental mode. The fundamental mode is the radiating mode and is modeled by the transmission lines. The equivalent reactance of the individual layers are presented in Equation 2.11 and 2.12. For the transmission line model the incident plane wave is split into the TE- and TM-components, with θ the angle of the incident plane wave.

$$Z_{n,TM} = \frac{-j}{B_n} \tag{2.11}$$

$$Z_{n,TE} = \frac{-j}{B_n\left(1-\frac{\sin^2\theta}{2}\right)}. \tag{2.12}$$

2.2.2 Combination of Several Layers

The transmissions line model of the ADLs can be seen as a cascade of transmission line sections and shunt reactances. The most convenient way to cascade two-port networks is by representing each block as an ABCD matrix. The total ABCD matrix for the entire ADL structure can be then expressed as a product of the individual ABCD matrixes.

The dielectric spacer between two layers can be described as a transmission line, whose ABCD matrix representing is presented in Equation 2.13 and 2.14, respectively for the TM- and the TE-components. In the equations, L is the length of the line section, $k_d = k_0\sqrt{\varepsilon_r}$ is the wavenumber
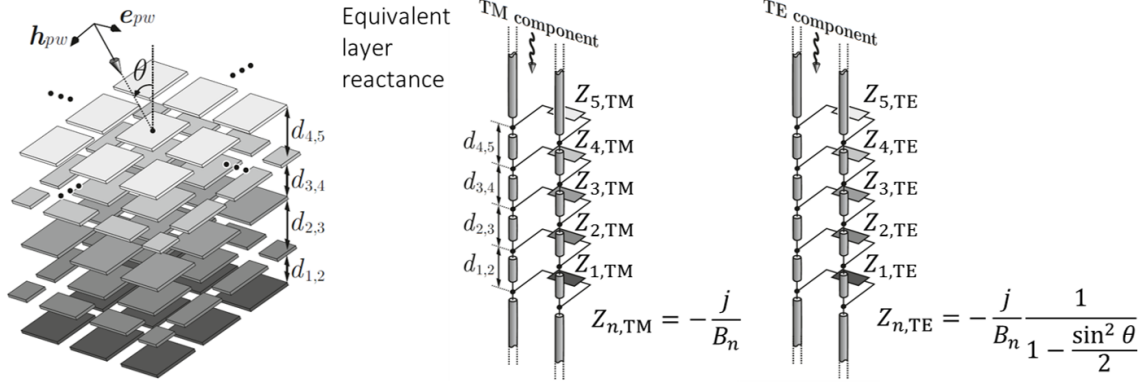
Figure 2.4: Equivalent transmission line of the artificial dielectric layers for plane wave incidence.

in the medium, k_{zd} is the z-component of the propagation in the medium $k_{zd} = \sqrt{k_d^2 - k_0^2 \sin^2 \theta}$, where *theta* is the incident angle of the plane wave impinging from free space and $Z_d = \zeta_0/\sqrt{\varepsilon_r}$ is the characteristic impedance of the medium. k_0 and *zeta*$_0$ are the wavenumber and the intrinsic impedance of vacuum, respectively.

$$ABCD_{line,TM} = \begin{bmatrix} \cos(k_{zd}L) & j\frac{Z_d k_{zd}}{k_d} \sin(k_{zd}L) \\ j\frac{k_d L}{Z_d} \text{sinc}(k_{zd}L) & \cos(k_{zd}L) \end{bmatrix} \tag{2.13}$$

$$ABCD_{line,TE} = \begin{bmatrix} \cos(k_{zd}L) & jZ_d k_d L \text{sinc}(k_{zd}L) \\ j\frac{k_{zd}}{Z_d k_d} \sin(k_{zd}L) & \cos(k_{zd}L) \end{bmatrix} \tag{2.14}$$

Similar matrixes can be obtained for the shunt admittances $Y = 1/Z$ using the well known formula:

$$ABCD_{ADL,TM} = \begin{bmatrix} 1 & 0 \\ jB_n & 1 \end{bmatrix} \tag{2.15}$$

$$ABCD_{ADL,TE} = \begin{bmatrix} 1 & 0 \\ j\frac{B_n}{1-(\sin^2 \theta)/2} & 1 \end{bmatrix} = \begin{bmatrix} 1 & 0 \\ j\frac{B_n}{1-k_\rho^2/(2k_{layer})} & 1 \end{bmatrix} \tag{2.16}$$

where $k_l ayer$ is an average wavenumber of the dielectric media above and below the patch layer. It is convenient to rewrite the admittance for the TE component in terms of x and y components of the wave number, $k_\rho = \sqrt{k_x^2 + k_y^2}$, because the internal incident angle of the wave for each individual layer is unknown and also because the wave impinging could be inhomogeneous as part of the non-visible spectrum of a near field source.

Cascading all N ABCD matrixes is done as follows:

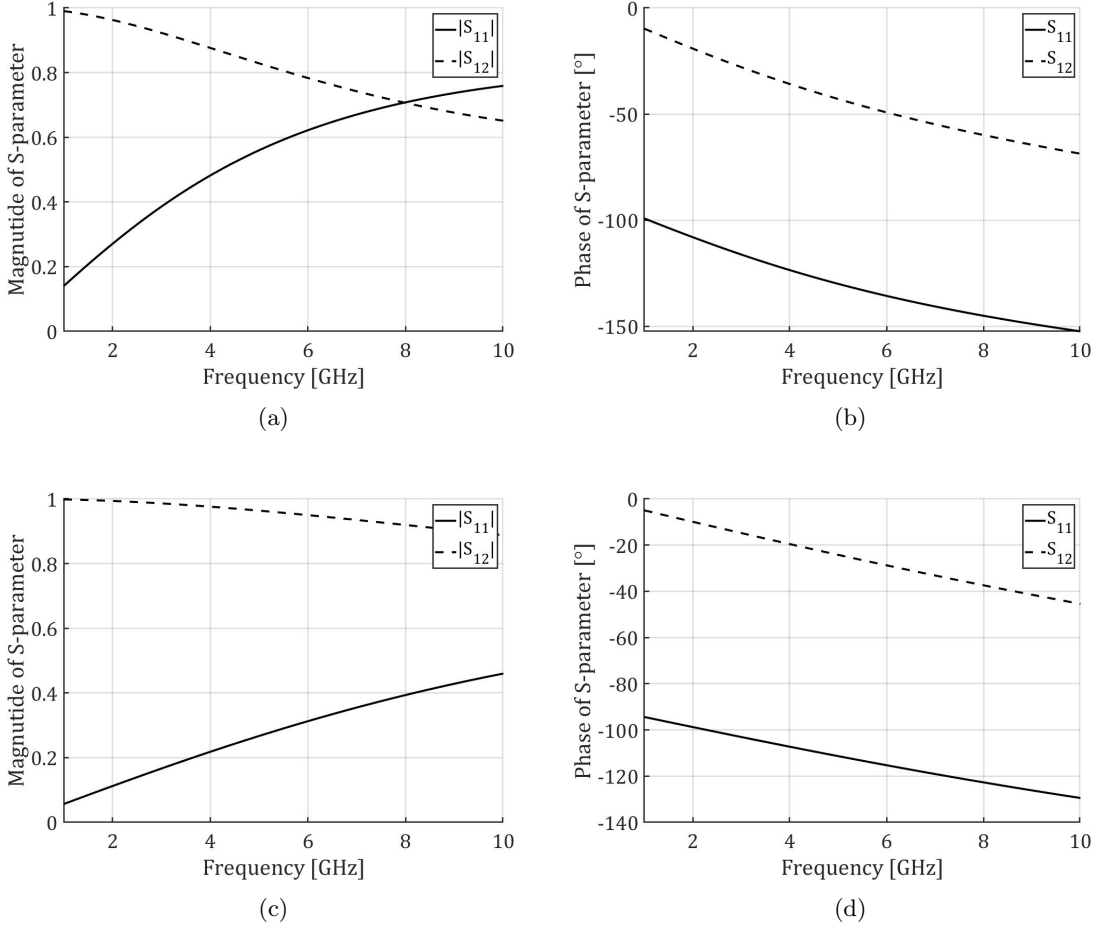$$ABCD_{total} = \prod_{i=1}^{N} [ABCD]_i. \tag{2.17}$$

13

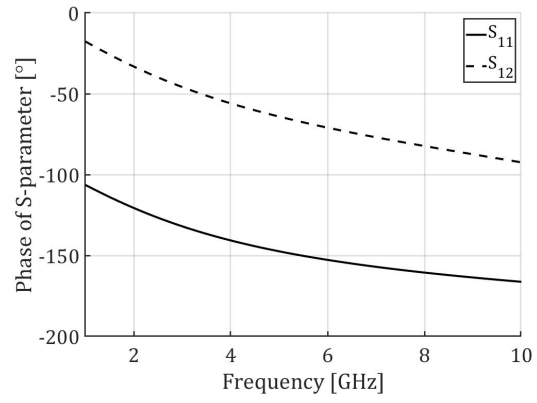Figure 2.5: Validation case 1: (a) magnitude TE, (b) phase TE, (c) magnitude TM and (d) phase TM.

2.2.3 Examples of ADL Slabs

For completeness, to check the correct implementation of the method, two cases are considered. Both cases describe an ADL slab presented in [41]. In the first case the ADL slab consits of 5 layers with equal spacing,$d_{n,n+1} = d_{n-1,n} = 0.012\lambda_0$ between them, no shift and a period of $p = 0.0785\lambda_0$. However, the with of the slot is varied in each layer, $w = [0.01\lambda_0, 0.015\lambda_0, 0.02\lambda_0, 0.025\lambda_0, 0.03\lambda_0]$. The reflection and transmission coefficient obtained for the TE and TM incident waves are presented in Fig. 2.5 and are consistent with the results found in [41], where the authors compared the results with a full wave simulation to validate the method.
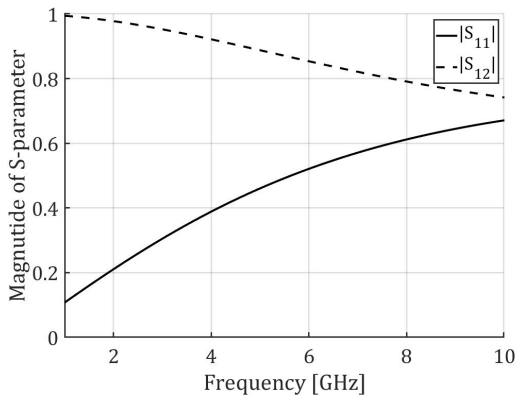
The second case varies all the parameters of the ADL slab except for the period which is required to stay constant for this method. In case 2 the parameters of the 5 layers are $d_{n,n+1} = [0.01\lambda_0, 0.015\lambda_0, 0.02\lambda_0, 0.025\lambda_0]$, $w_{n,n+1} = [0.01\lambda_0, 0.015\lambda_0, 0.02\lambda_0, 0.025\lambda_0, 0.03\lambda_0]$ and $s_{n,n+1} = [0.4p, 0.3p, 0.1p, 0]$. The results in Fig. 2.6 also compare well to the results obtained in [41].
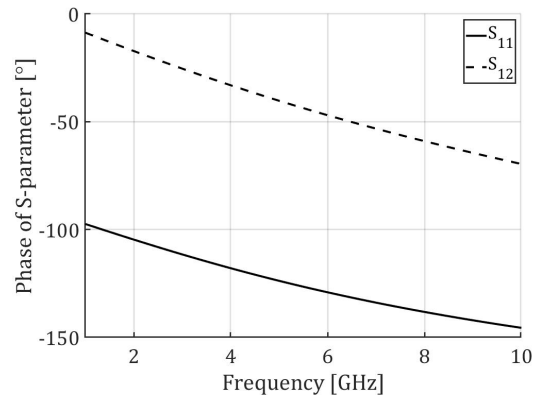
14
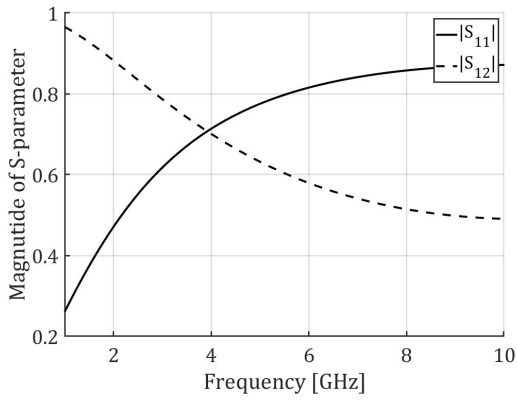
Figure 2.6: Validation case 2: (a) magnitude TE, (b) phase TE, (c) magnitude TM and (d) phase TM.
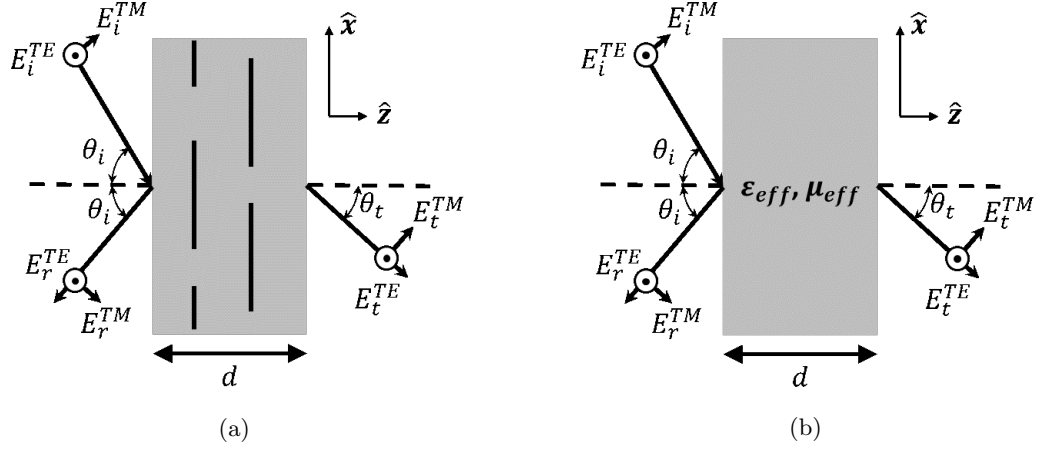
Figure 2.7: Geometry of homogenization method from Cohen [42] with a) the ADL and b) the effective dielectric slab

2.2.4 Homogenization of ADL Slab

Like an isotropic homogeneous dielectric, the ADL slab behaves, for a plane wave propagating through the slab, in such a way that the TE and TM wave are decoupled from each other. This is a known property of artificial dielectric with square symmetry, if the period is small compared to the wavelength. Despite the two modes are decoupled, the propagation through the slab behaves differently for the TE and TM-waves. This behavior of the ADL slab can be characterized in terms of effective constitutive parameters.

It is then useful to derive an equivalent homogenized anisotropic material that approximates the artificial dielectric. A method that can be used for this purpose utilizes the S-parameters from an incident plane wave from broadside and an oblique angle to obtain the effective permittivity and permeability tensors of the material [42]. The effective parameters are used to derive an homogeneous anisotropic slab with the same behavior as the ADL. The relative permittivity and the permeability of the ADL can be represented with diagonal tensors as follows:

$$\underline{\underline{\varepsilon}}_{eff} = \begin{bmatrix} \varepsilon_x & 0 & 0 \\ 0 & \varepsilon_y & 0 \\ 0 & 0 & \varepsilon_z \end{bmatrix} \tag{2.18}$$

and

$$\underline{\underline{\mu}}_{eff} = \begin{bmatrix} \mu_x & 0 & 0 \\ 0 & \mu_y & 0 \\ 0 & 0 & \mu_z \end{bmatrix} . \tag{2.19}$$

The procedure is valid for any incident plane wave, as presented by Fig. 2.7. The method of extraction is further described in Appendix A. For this section an example ADL is used to identify some key features of the ADL slab.

The example slab under test is an ADL slab with seven layers, with a unit cell size of $p = 1.5$ mm. All the parameters are shown in Tab. 2.1. A maximum shift, $s = 0.5p$, is applied between
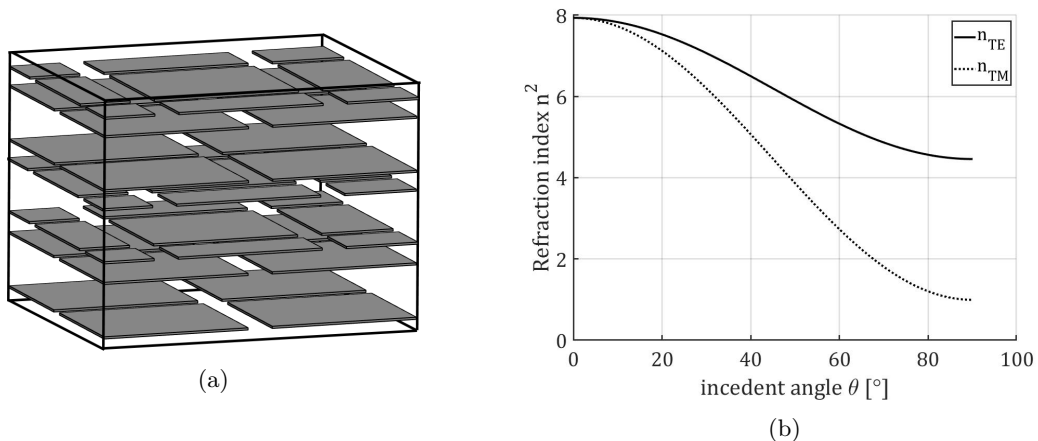
Figure 2.8: a) Example of Unit cell of an ADL slab for homogenization and b) its refraction index

sets of layers with an alternating spacing of $d_z/2 = (d/7)/2$ and $3d_z/2 = 3(d/7)/2$, where d is the height of the entire structure, which is determined to be a quarter wavelength $d \approx 2.66$ mm. Lastly, the width of the slot in between patches is set to reach the desired permittivity. The ADL slab is shown in Fig. 2.8(a). The equivalent refractive index is calculated with the method in [42] for both TE and TM waves, by knowing the S-parameters under plane wave incidence from the equivalent transmission line model of the ADLs (Fig. 2.8(b)).

From Fig. 2.8(b) it is seen that the refraction index decreases while increasing the incident angle. Specifically for the TM case, for extremely large incident angles ($\theta_i = 90°$) the refraction index tends to that of the host medium, which is free space in this case thus $n_{TM}|_{\theta=90°} = n_{host}$. This behavior can be interpreted with the fact that the patches are purely horizontal and thus the z-component of the incident wave does not interact with the structure. This is the key property of ADLs, since the decrease mitigates the surface waves otherwise present in the structure and still offers impedance matching at wide scan angle. For the TE wave, the refractive index still decreases with frequency but it tends to a value higher than the host medium, since even for $\theta = 90°$ the electric field is horizontally oriented and interacts with the patches.

Table 2.1: Simulation parameters for ADL.

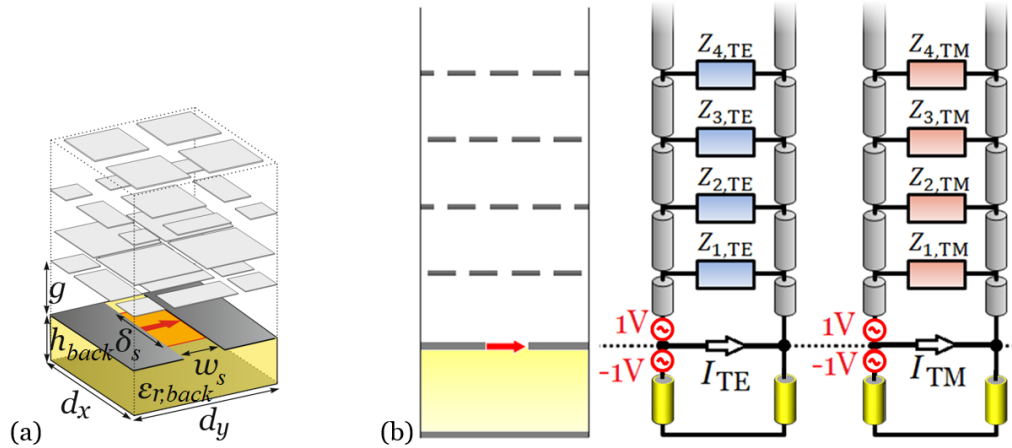| Parameter	Value
f_0	10 GHz
p	$0.05\lambda_0$
$\varepsilon_x = \varepsilon_y$	8
d	$0.25\lambda_0/\sqrt{\varepsilon_x}$
d_z	$d/7$
d_{adl}	$[3d_z/2, d_z/2, 3d_z/2, d_z/2, 3d_z/2, d_z/2]$
s_{adl}	$[0, p/2, 0, p/2, 0, p/2]$
w_{adl}	$p/10$

17

Figure 2.9: (a) Connected slot unit cell loaded with artificial dielectrics; (b) Equivalent transmission line model to find the spectral Green's function.

The effective constitutive parameters of the ADL slab are determined from these refraction index for both waves. From Fig. 2.8a it is seen that the structure is symmetric in $\hat{x}$ and $\hat{y}$, therefore the x and y components of the permittivity and the permeability are equivalent as well: $\varepsilon_x = \varepsilon_y = 8$ and $\mu_x = \mu_y = 1$. In addition, the structure is planar, thus no currents can run in the $\hat{z}$ direction, neither along z or in a closed loop, therefore the x and y components of the permeability and the z-component of the permittivity are equal to those of the host medium $\mu_x = \mu_y = 1$ and $\varepsilon_z = 1$. However, due to a loop current on the patch in the xy-plane, the z-component of the permeability is less than 1 ($\mu_z = 0.22$). These characteristics are inherent of the ADL structure.

2.3 Combination of ADLs and Connected Slot Array

As mentioned earlier, dielectrics and ADL slabs can be used to improve the front-to-back ratio of the antenna arrays. This increase of the ratio is desired to reduce the distance from the backing reflector, which is often added to the antenna to ensure that the radiation occur only to one direction. In this section the procedure of combining the three elements, connected slot array, backing reflector and an ADL slab, is discussed. The method for the active input impedance of a connected array described in Sec. 2.1 is employed. For this method a transmission line model as in Fig. 2.9 is used, as described in [43].

2.3.1 Adding Superstrate and Backing Reflector to the Connected Array

First, recall the split of the Green's function into the lower and upper half space with the connected slot array at $z = 0$, defined in Equation 2.3. All operations in section 2.1 are linear operations, therefore the spectral Green's function can also be represented in terms of these two separate problems. In addition, the spectral Green's function can be described as the solution of a transmission line model with two unknown currents I_{Ti}^{up} and I_{Ti}^{down} for both the TE- and TM- waves, here Ti represents either the TE- of the TM-wave. In the case of a connected array with grounded substrate

and ADL superstrate, the current are solution of transmission lines in Fig. 2.9b.

The unknown currents at $z = 0$ are obtained as $I_{Ti}^{up} = 1/Z_{Ti}^{up}$ and $I_{Ti}^{down} = 1/Z_{Ti}^{down}$. The impedance $Z_{up,Ti}$ is obtained by converting the total ABCD matrix of the entire ADL structure into a two-port impedance matrix Z_{Ti}^{up} [44]. Then the input impedance of the superstrate is calculated by terminating the output port with the load impedance which is the free space impedance $Z_{0,Ti}$:

$$Z_{Ti}^{up} = Z_{Ti,11}^{up} - \frac{Z_{Ti,12}^{up} Z_{Ti,21}^{up}}{Z_{0,Ti} + Z_{Ti,22}^{up}}. \tag{2.20}$$

For the impedance $Z_{down,Ti}$, a transmission line model which is short circuited can be used to represent the backing reflector:

$$Z_{Ti}^{down} = j Z_{d,Ti} \tan\left(k_{zd} h_{back}\right) \tag{2.21}$$

where $Z_{d,TE} = \frac{\zeta_d k_d}{k_{zd}}$, $Z_{d,TM} = \frac{\zeta_d k_{zd}}{k_d}$ and h_{back} is the distance from the array to the backing reflector as shown in Fig. 2.9a.

Implementing Equation 2.3 into the solution for the active input impedance, Equation 2.1 can be also expressed as

$$Z_a = \frac{1}{d_x} \sum_{m_x=-\infty}^{\infty} \frac{\mathrm{sinc}\left(\frac{k_{xm}\delta_s}{2}\right)^2}{D_\infty^{up}(k_{xm}) + D_\infty^{down}(k_{xm})}. \tag{2.22}$$

The validation of this method with a backing reflector is performed again with a commercial full wave solver. For the same slot as subsection 2.1.1, however now with a backing reflector at $h_{back} = \lambda_0/4$ and $\varepsilon_{r,back} = 1$. In Fig. 2.10 the corresponding active input impedance for broadside is provided and for scanning in the H-plane to 60° is provide. It is seen that the method and the simulation with commercial solver yield the same result.
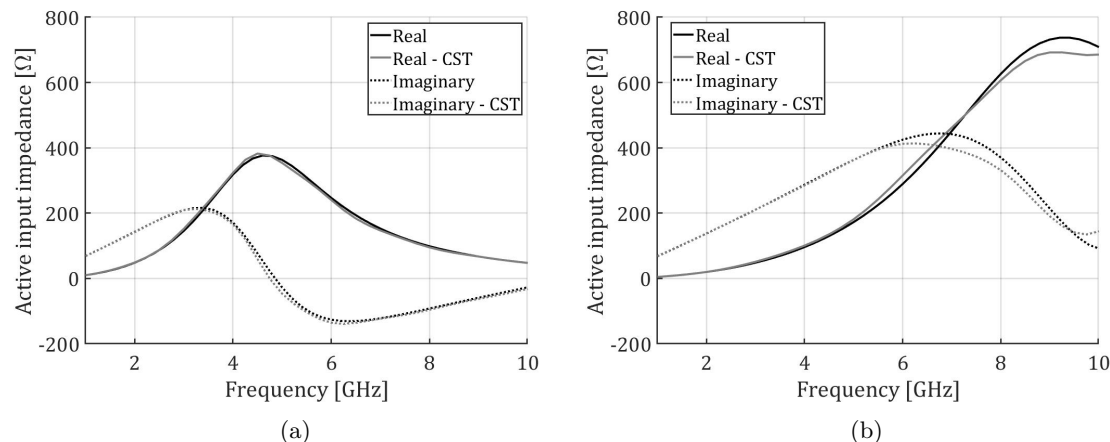

Figure 2.10: Active input impedance of connected slot array with a backing reflector where $w_s = 0.1\lambda_0$, $\delta_s = 0.1\lambda_0$, $d_x = d_y = 0.5\lambda_0$ and $h_{back} = \lambda_0/4$ for (a) broadside and (b) scanning to $\theta = 60°$ in the H-plane.

19

(a) two-dimensional
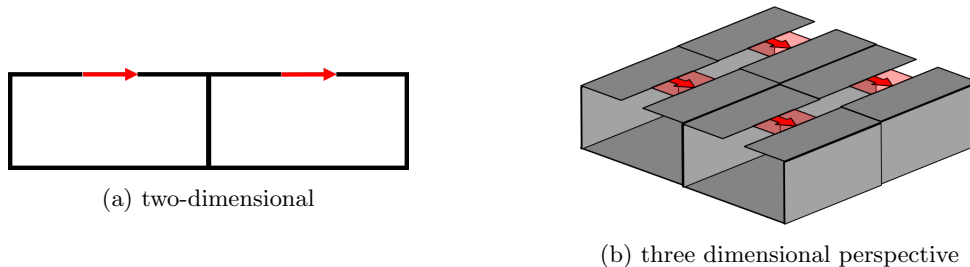

(b) three dimensional perspective

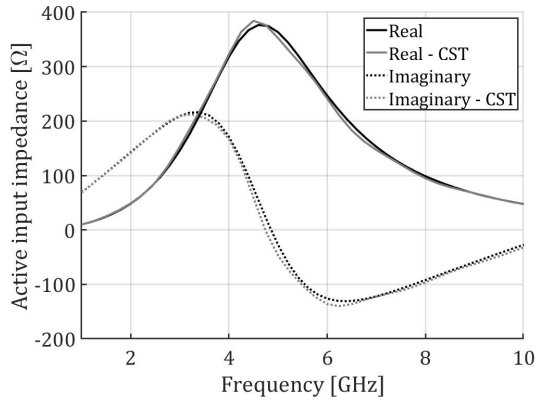Figure 2.11: Connected slot array with vertical walls.

2.3.2   Implementing Vertical Walls

The use of the backing reflector can introduce undesired effect, such as a parallel plate waveguide modes, propagating between the slot plane and the ground plane [5, 33]. To prevent these modes from propagating, vertical walls can be placed in between adjacent slots. These walls can be modeled in the transmission line model above, as shown in [5].

The vertical walls are placed in the center between two slots, vertically from the slot plane to the backing reflector. The model for the longitudinal transverse spectral Green's function, Equation 2.2, must compensate for the fact that the wave is not propagating to the next slot. The walls are periodic in the y-direction and the scan angle of the array is not relevant anymore for the propagation in the new created cavity, therefore $k_{y0} = 0$. However, the periodicity in the y-direction cannot be neglected, since the vertical walls now provide an image of the magnetic source, as stated by the image theorem. Therefore, the wave number k_{ym} becomes $-\frac{2\pi m_y}{d_y}$ and thus:

$$D_\infty^{down}(k_{xm}) = \frac{1}{d_y} \sum_{m_y=-\infty}^{\infty} J_0\left(-\frac{\pi m_y w_s}{d_y}\right) G_{xx}^{HM}\left(k_{xm}, -\frac{2\pi m_y}{d_y}\right). \tag{2.23}$$

The implementation of the vertical walls is validated with the same slot as in subsection 2.1.1 and subsection 2.3.1. The simulation and the method are in agreement, as seen in Fig. 2.12. To perform a correct validation the array is now scanned in the E-plane, because the effect of the presence of the walls is expected in that plane.

20
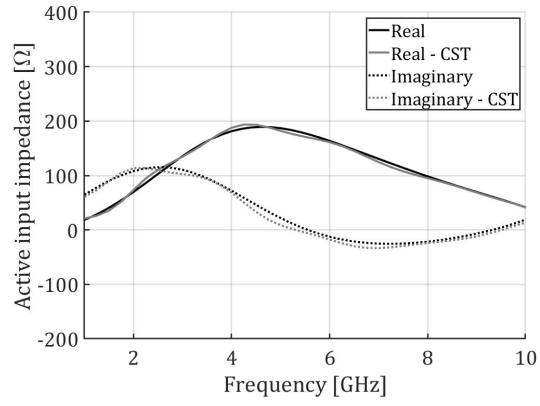
Figure 2.12: Active input impedance of connected slot array with a backing reflector and vertical walls along the slot where $w_s = 0.1\lambda_0$, $\delta_s = 0.1\lambda_0$, $d_x = d_y = 0.5\lambda_0$ and $h_{back} = \lambda_0/4$ for (a) broadside and (b) scanning to $\theta = 60°$ in the E-plane.

Chapter 3

Study on Cross Polarization

3.1 Definition of Cross Polarization level

One of the common requirements for wideband wide-scanning arrays in multi-functional platforms is the polarization agility. Cross-polarization levels should be kept low within the entire field of view in dual-polarized arrays. However, polarization purity is hard to achieve especially for arrays that are designed to operate over large bandwidth.

The specific array under investigation consists of planar connected slots with artificial dielectric slabs above the antenna aperture. Despite being a key concept to achieve wide bandwidth and wide scanning, artificial dielectric superstrates tend to deteriorate the polarization performance when scanning in the diagonal planes. The reduction of the cross polarization when artificial dielectric layers are employed is still one of the main challenges in the design of these arrays.

To reduce that cross polarization, one must first understand the causes of cross polarization, as well as the typical values to be expected from connected arrays in free space, with a dielectric substrate and/or superstrate, and with an ADL slab.

In this thesis the third definition of cross polarization by Ludwig [45] is used, as it is the most common. The cross polarization is defined as the ratio between the desired component of the radiated electric field, the co-polarization, and the undesired component, the cross-polarization. In our analysis and in chapter 2 the radiating elements is a magnetic current oriented along $\hat{x}$. According to the Ludwig's third definition, the co-polarized and cross-polarized components associated with this source can be related to the θ- and phi-components as follows:

$$E_{co} = E_\theta \cos \phi - E_\phi \sin \phi \tag{3.1}$$
$$E_{cross} = E_\theta \sin \phi + E_\phi \cos \phi. \tag{3.2}$$

The cross polarization level is therefore given by:

$$X_{pol} = \left| \frac{E_{cross}}{E_{co}} \right|^2. \tag{3.3}$$

With this definition, the highest cross-polarization level for a linearly polarized source is expected in the diagonal plane (D-plane, at $\phi = 45°$) and increasing for higher and higher values of the scan angle θ.
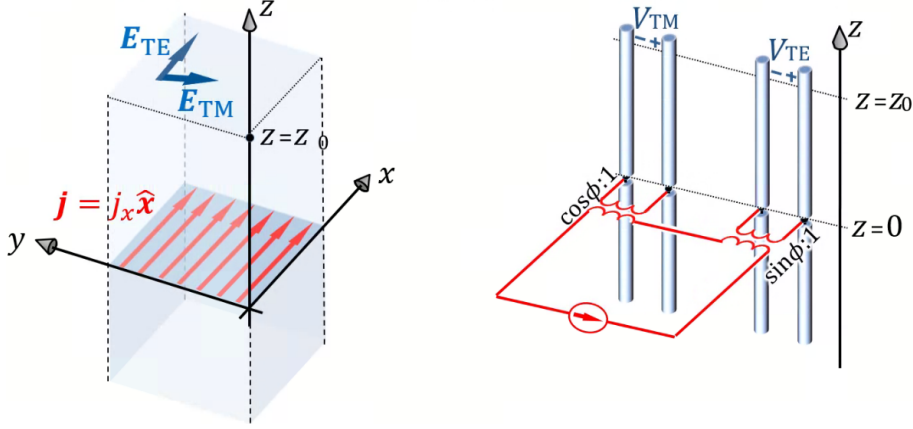
Figure 3.1: (a)Wheeler current in free space and (b) the transmission line model of that current.

3.2 Cross Polarization of Connected Arrays

Designs of connected arrays can be of two types: (1) connected dipole array and (2) the connected slot array. Therefore, it is necessary to assess the polarization purity of both arrays. Although, the two structures are complementary and behave in the same way in terms of impedance properties, they do not necessarily exhibit the same polarization properties when radiating in a generic dielectric stratification. To better understand how the cross polarization is affected by the presence of real or artificial dielectrics above or below the radiating aperture, it is convenient to first introduce the polarization characteristics of an ideal source. To this aim, the cross polarization of the Wheeler current is described first.

3.2.1 Wheeler Current

Let us consider an ideal x-oriented Wheeler current sheet [46], [22], radiating in free space, as shown in Fig. 3.1(a). This represents a current with constant amplitude A over the infinite xy-plane, with a linear continuous phase distribution to point to the angle θ, ϕ:

$$\vec{j}(x,y) = j_x(x,y)\hat{x} = Ae^{-jk_{x0}x}e^{-jk_{y0}y}\hat{x}. \tag{3.4}$$

where $k_{x0} = k\sin\theta\cos\phi$, $k_{y0} = k\sin\theta\sin\phi$, and k is the free-space wavenumber. The radiated electric field can be expressed as the sum of two components, one transverse electric (TE) and one transverse magnetic (TM). One simple way to calculate the two components of the radiated field for any pointing angle is to represent the radiation with an equivalent transmission line model, as in Fig. 3.1(b). The source is a current generator with amplitude A connected to two transmission lines representing the propagation of the TE and TM components of the radiated plane-wave along z, in the upper and lower half spaces. The two transmission lines are connected to the source by means of two transformers with turn ratios $1 : \cos\phi$ and $1 : \sin\phi$ that account for the projection of the field onto the x-axis. The characteristic impedances of the two lines are given by $Z_{TE} = 120\pi/\cos\theta$ and $Z_{TM} = 120\pi\cos\theta$ while the propagation constant is $k_{z0} = k\cos\theta$. The radiated field at $z = z_0$ can be evaluated by calculating the voltages in the two transmission line at the same height $z = z_0$.
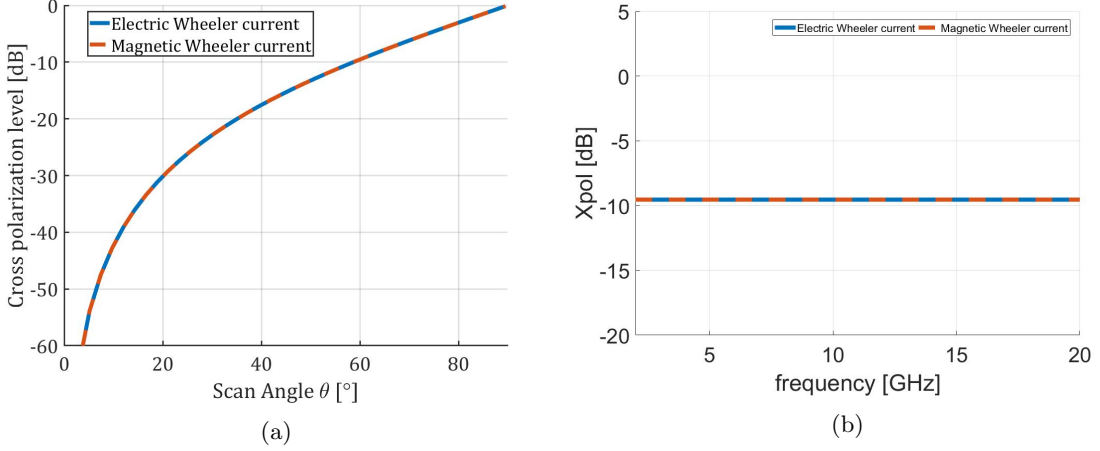
Figure 3.2: Cross polarization level of Wheeler current radiating in the D-plane ($\phi = 45°$): (a) angle dependence at f_0 and (b) frequency dependence with $\theta = 60°$.

It is then evident that, in the main planes ($\phi = 0°$ and $\phi = 90°$), the cross-polarization levels are zero, because one of the two transformer ratio is 0. On the other hand, for the diagonal plane (D-plane, $\phi = 45°$), the field propagates in both transmission lines. In this case, the cross-polarization (Xpol) levels, according to the third definition of Ludwig, can be calculated as

$$E_{co}(\theta, \phi = 45°) = -\frac{V_{TM}}{2\cos\theta} - \frac{V_{TE}}{2} \tag{3.5}$$

$$E_{cross}(\theta, \phi = 45°) = -\frac{V_{TM}}{2\cos\theta} + \frac{V_{TE}}{2} \tag{3.6}$$

$$X_{pol}(\theta, \phi = 45°) = \frac{1 - \sec\theta}{1 + \sec\theta} . \tag{3.7}$$

The expression given for the Xpol is valid for free space. More in general, in the presence of arbitrary dielectric stratifications, one can solve for the voltages V_{TE} and V_{TM} in the transmission lines above the stratified dielectrics. The voltages give in turns the different components of the radiated fields, which can be projected on the co-polar and cross-polar unit vectors.

This Xpol of the ideal Wheeler current in free space is plotted as a function of θ for scanning in the diagonal plane in Fig. 3.2(a). It is evident that the Xpol increases as a function of the scan angle and it is equal to about -9.5 dB for $\theta = 60°$, while it reaches 0 dB for $\theta = 90°$. Moreover, as expected, the cross-polarization ratio is constant as a function of the frequency, Fig. 3.2(b).

The same Xpol levels are also obtained when adding a backing reflector, with a distance of $h = 0.25\lambda_0$ with $f_0 = 10$GHz, if vacuum is consider as material between the ground plane and the array, as shown in Fig. 3.3(a). Although the presence of the backing reflector introduces a frequency dependence in the impedance, it does not affect the Xpol, which remains the same as in Fig. 3.2.

A connected array in the low-frequency limit approximates the Wheeler current. More specifically an electrical current sheet can be associated with a densely sampled connected array of dipoles, while a magnetic current sheet distributed above and below a PEC surface is equivalent to a con-
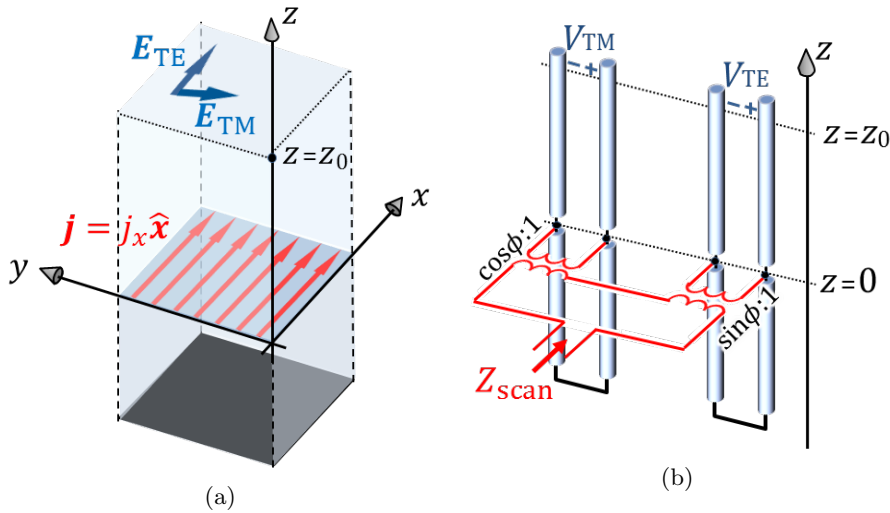
24

Figure 3.3: (a) Wheeler current with a backing reflector and (b) the corresponding transmission line model.

nected slot array. The difference between these representations is that, for connected slots, the presence of the PEC plane decouples the upper half space and lower half space, while this is not the case for connected dipoles.

3.2.2 Connected Array with Dielectric Superstrate

Substrates and superstrates made out of dielectric materials are often used to increase the antenna performance and to be able to reduce the distance to the backing reflector. However, those slabs can affect the Xpol level depending on the permittivity and the type of array. In this section the two types of connected arrays are compared based on the cross polarization alone.

Connected Dipole Arrays
Let us consider the same Wheeler current in the presence of the backing reflector, but now loaded with a dielectric superstrate, as depicted in Fig. 3.4. A practical model to approximate the Wheeler current in a commercial software can be obtained by considering a connected array of dipoles and reducing the unit cell size (d_x and d_y) to a value lower than 0.2λ at the maximum frequency of investigation. The simulated Xpol for such an array is shown in Fig. 3.5, compared with circuit model in Fig. 3.4(b), both as a function of the scan angle, for a given frequency (10 GHz), and as a function of the frequency for scanning to $\theta = 60°$ in the D-plane. A good agreement with the transmission line model is obtained when size is small compared to the wavelength, for the simulations presented the unit cell size is $d_x = d_y = 0.1\lambda_0$. Some differences are visible for scan angle close to broadside, but these are referring to very small values, below -30 dB.

The parameters of the array simulated with the commercial software are reported in Tab. 3.1, where w_d and δ_d are the width of the dipole and the size of the delta-gap, respectively, for the
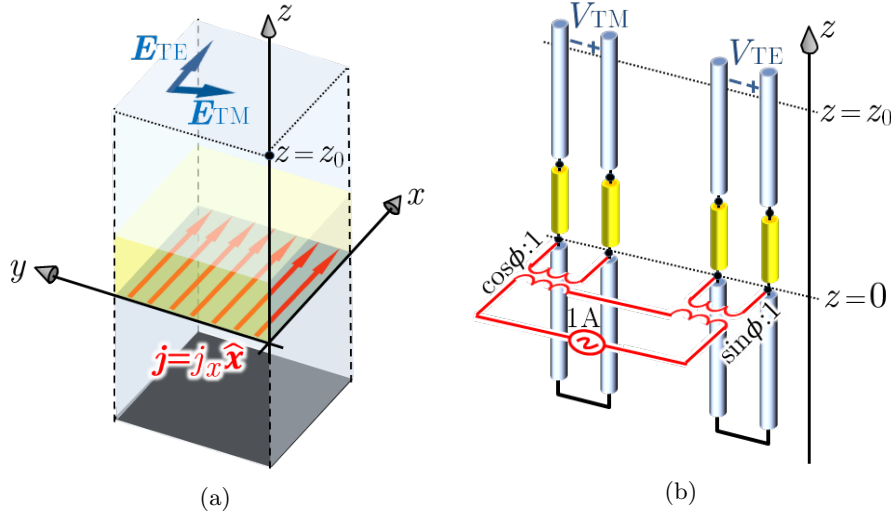
25

Figure 3.4: (a) Schematic representation of the current with the backing reflector and the superstrate with (b) the corresponding transmission line model.
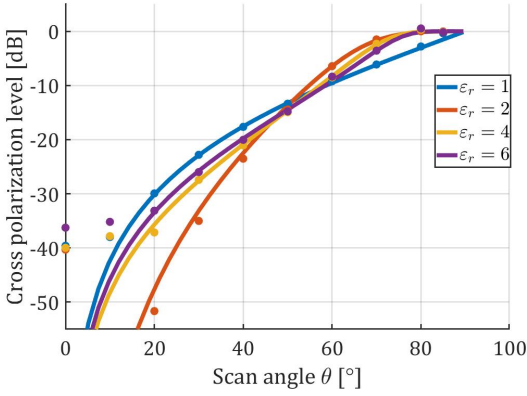
connected dipole array.

The dipole array in free space with the use of the transmission line model was already shown in the previous section. In Fig. 3.5 the agreement with the simulation is observed when a dielectric superstrate is added. Also the dielectric with a permittivity of ε_r and a thickness of $h = 0.25\lambda_0/\sqrt{\varepsilon_r}$ is placed on top of the array, as shown in Fig. 3.4. The cross polarization level at $f_0 = 10$ GHz for different scan angles in the D-plane is shown in Fig. 3.5a along with the level for a scan angle of $60°$ in the D-plane for different frequencies ranging from $0.2f_0$ to $2f_0$.

The commercial solver and the coupled transmission line model agree well. In addition, around broadside some deviation is seen between the solver and the model, however since the level is very low (< -30 dB) this deviation is of no great concern as it is most likely a result of the solver's settings. Thirdly, the cross polarization level at small scan angles ($< 50°$) is lowered by the use of the dielectric layer. However, for large scan angles the level is higher than the free space case. In this project the design is aimed to have a scan angle of at least $60°$, which makes the effect

Table 3.1: Simulation parameters for connected arrays approximating the Wheeler current

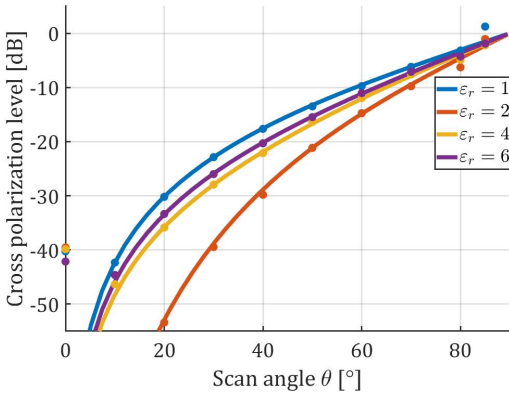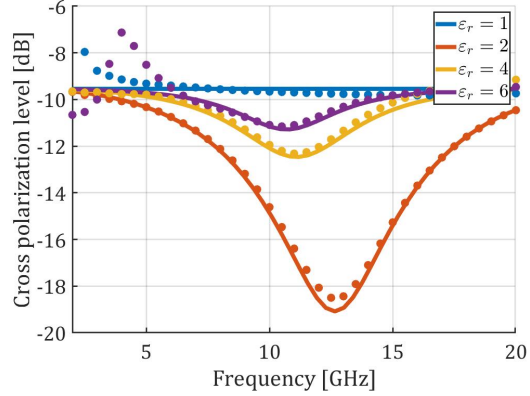| Parameter	Value
f_0	10 GHz
$d_x = d_y$	$0.1\lambda_0$
w_d	$d_x/3$
δ_d	$0.01\lambda_0$
h_{back}	$0.25\lambda_0$
w_s	$0.01\lambda_0$
δ_s	d_x

26
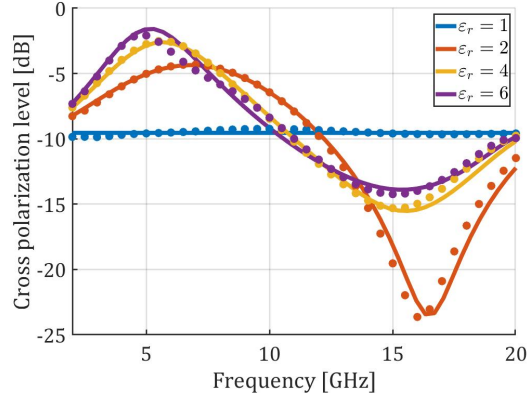
Figure 3.5: Cross polarization level (D-plane, $\theta = 60°$) of a connected dipole array and over (a) scan angle and (b) over frequency.

Figure 3.6: Cross polarization level (D-plane, $\theta = 60°$) of a connected slot array and over (a) scan angle and b) over frequency.

by the dielectric undesired. Moreover, at lower frequencies ($f < f_0$) the cross polarization is significantly higher than the free space case. Since impedance matching layers are often designed with a height of $h = 0.25\lambda_0/\sqrt{\varepsilon_r}$ it is expected that such transformers will increase the cross polarization significantly. Lastly, the cross polarization is reduced at higher frequencies. That makes the use of the dielectrics desired, however the array is typically designed in the range of $0.2f_0$ to f_0, thus the usability of the dielectrics to reduce the cross polarization is questionable with connected dipole arrays.
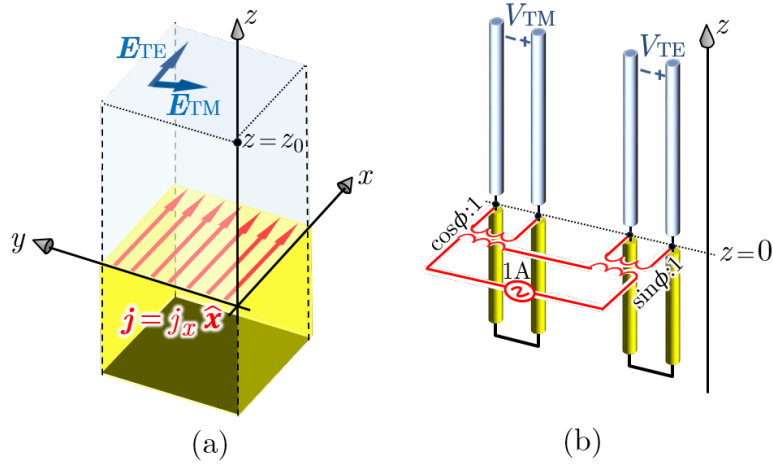
27

Figure 3.7: (a) Wheeler current with dielectric substrate and (b) the transmission line model of that current.

Connected Slot Arrays

When considering a connected slot array, one may expect similar Xpol properties, since the only difference would be the replacement of the Wheeler electric current sheet with a magnetic current. However, since in the case of connected slot arrays, the equivalent magnetic currents are located above and below a perfectly conducting metallic sheet, the radiation in the upper and lower half spaces are decoupled. The same decoupling effect does not occur in connected dipoles, and thus what is reflected by the ground plane can still influence the radiation in the upper medium.

To verify this effect, the connected slot unit cell is also implemented in the commercial solver, with the parameters reported in Tab. 3.1. The calculated Xpol levels are shown in Fig. 3.6. The impact of the decoupling is seen in the Xpol ratio, since the values are always lower or equal to those of free space case, for all scan angles and frequencies. Some discrepancy between the Wheeler ideal current and the real connected slot array with small period is visible at low frequencies in Fig. 3.6(b), for some of the permittivity values of the superstrate. The fact that the simulated Xpol values increase also for free space could likely be associated with a numerical error of the simulation. At low frequency the slot width becomes lower than $\lambda/500$ which could result in strong mismatch and loss of accuracy.

Nevertheless, it can be notices that the Xpol level of the connected slot array in Fig. 3.6(b) are lower than the values for the connected dipoles inFig. 3.5a(b), at least for single polarized arrays.

The results from this section, one could conclude that connected slot array with isotropic dielectric superstrate do not yield high Xpol levels, compared to the ideal free-space case.

3.2.3 Connected Array with Dielectric Substrate

The practical implementation of the backing reflector requires the inclusion of a substrate between the radiating current and the ground plane. The Wheeler current for grounded slab configuration
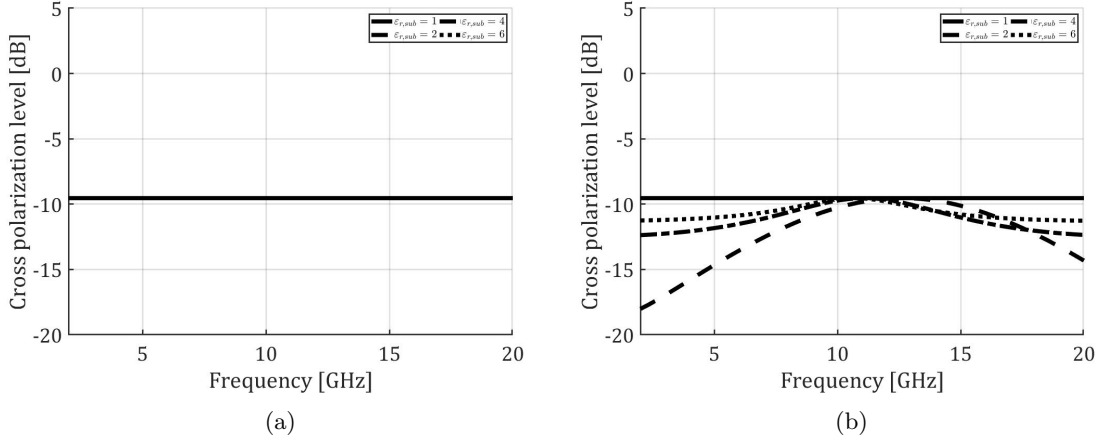
Figure 3.8: Cross polarization level (D-plane, $\theta = 60°$) of (a) a connected slot array and (b) a connected dipole array with a substrate and a backing reflector

is the one in Fig. 3.7, shown together with the equivalent transmission line model. The distance from the ground plane is assumed to be $h_{back} = 0.25\lambda_0/\sqrt{\varepsilon_{r,sub}}$, and several relative permittivities are considered in the present analysis.

The simulations of both connected dipoles and slots was carried out, and the resulting Xpol shows that the change of the dielectric substrate does not influence the cross polarization level for the connected slot. This is seen in Fig. 3.8(a), where only a single line is seen being all equal. This lack of impact is expected with the slot, since the PEC screen separates the radiation problem for the upper and lower half spaces. On the contrary, it is expected that the substrate will change the cross polarization level for the connected dipole case as the two halves are coupled. This is indeed seen in Fig. 3.8(b). The simulations show that the cross polarization is reduced by the addition of the substrate. Therefore, this is a viable simple option for the reduction of the cross polarization of connected dipole arrays. Although the analysis here focuses on the Xpol, the presence of dielectric substrate can still have a negative impact on the impedance matching of the array.

Also the case of having both substrate and superstrate with the same permittivity is investigated in Fig. 3.9. It is interesting to note that, for the connected slot case the Xpol is the same as the case of the supestrate alone, still below the ideal free-space value. On the other hand, for connected dipoles, while the superstate alone had a negative effect on the Xpol, which was shown to increase above the ideal free-space level, adding a substrate with the same permittivity as the superstrate has the beneficial effect to lower the Xpol again to values below the free space one (-9.5 dB).

In contrast to the dipole array, the level with the connected slot array is not changed. The advantage shown in case of the dipole array is not present here. Adding a substrate therefore does not yield a better result thus can't be used to reduce the cross polarization. The cross polarization is the same whether a substrate is present or not.
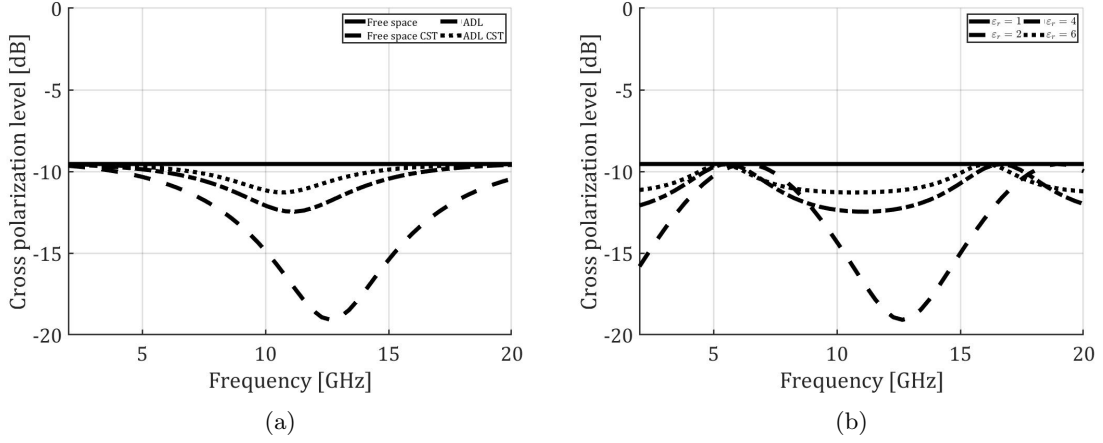
29

Figure 3.9: Cross polarization level (D-plane, $\theta = 60°$) of (a) a connected slot array and (b) a connected dipole array topped with a superstrate and a smaller distance to the backing reflector by a substrate.
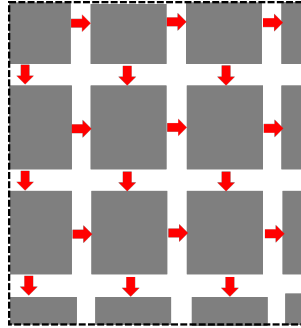

Figure 3.10: Schematic overview of infinite by infinite dual polarized slot array.

3.2.4 Cross Polarization of Dual Polarized Connected Array

From the results of the previous section it is evident that the connected slot array offers an advantage in terms of cross polarization level. However, only a single polarized slot was considered. The objective is to design a dual polarized antenna with two orthogonal slots. Therefore, it is not evident that the assumption of the two halves being decoupled with the use of the equivalence theorem is true in the case of dual polarization. When considering dual polarized slots antenna, as represented in Fig. 3.10, it is not rigorously defined if the array consists of connected slots or connected dipoles, depending if one observes the metal patches or the gasp between patches.

In the previous simulation for the connected slots, a feeding gap as large as the period was considered, thus the electric field was impressed over the entire slot region. To ensure that this assumption is not artificially reducing the Xpol level,the simulation is performed again by reducing the size of the feeding gap from d_x to $d_x/3$. The resulting Xpol is shown in Fig. 3.11(a) and it is seen that this reduction in the feed length does not change the results.
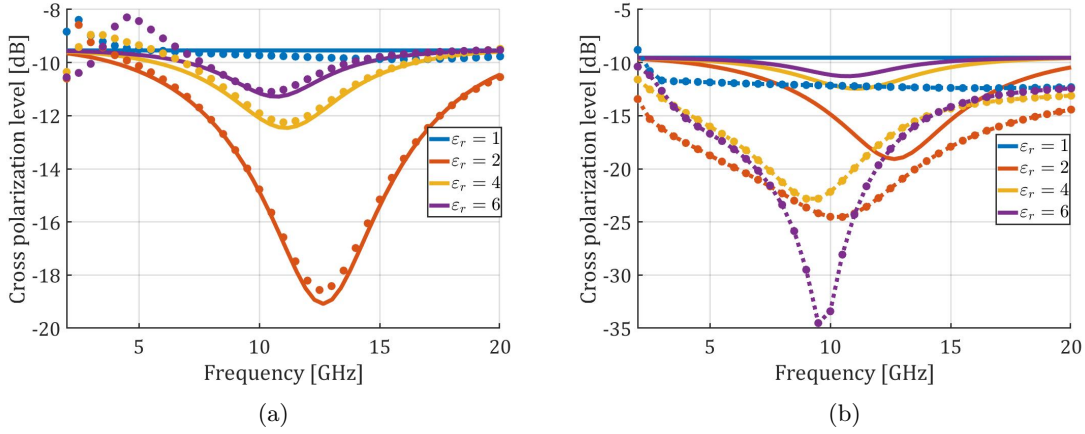
Figure 3.11: Cross polarization levels of (a) single polarized connected array with smaller feed size and (b) dual polarized connected slot array with superstrate.

Extending the array to a dual polarized configuration with the geometrical parameters as in Tab. 3.1, except for the reduced length of the feeding gap, yields the Xpol levels shown in Fig. 3.11(b). The Xpol ratio is even lower than the one associated with the single polarized slot. This effect is due to the mutual coupling between the two orthogonal feeds. The electric field from one slot can turn and reach the orthogonal slot. For broadside radiation, because of symmetry, two parallel feeds would generate electric fields that cancel out in correspondence of the orthogonal feed, as shown in Fig. 3.12. However, for scanning in the diagonal plane, the cancellation is not anymore occurring, and the power coupled to the orthogonal feed can be re-radiated with opposite phase compared to the original Xpol, thus reducing the Xpol level.

If the orthogonal feed is removed the array becomes essentially a fat connected dipole array. Then the Xpol is observed to increase again as the case of connected dipoles in the previous section (Fig. 3.5(b)).
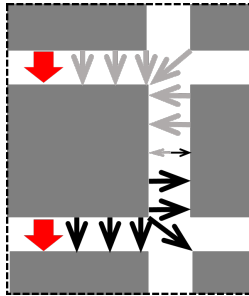

Figure 3.12: Schematic of dual polarized slot array canceling the cross polarization in the orthogonal slot for broadside radiation.
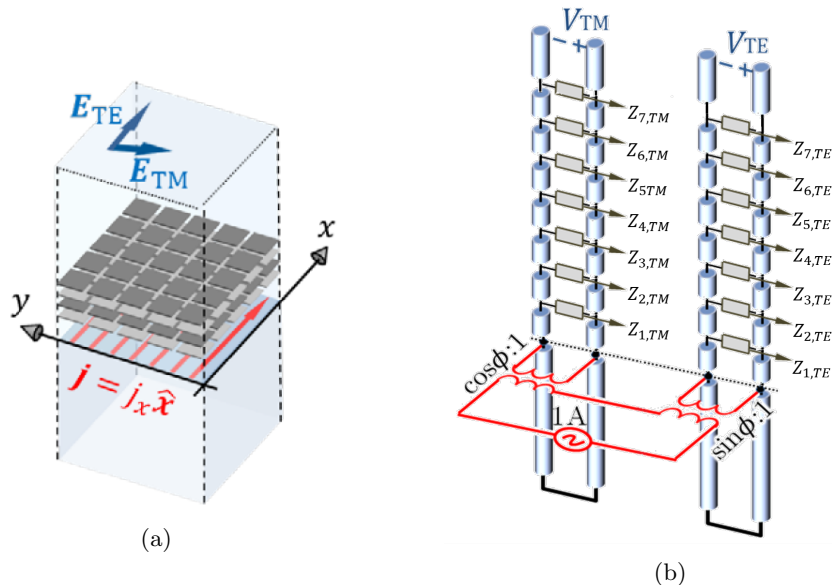
Figure 3.13: (a) Wheeler current with artificial dielectric superstrate and (b) the transmission line model of that current.
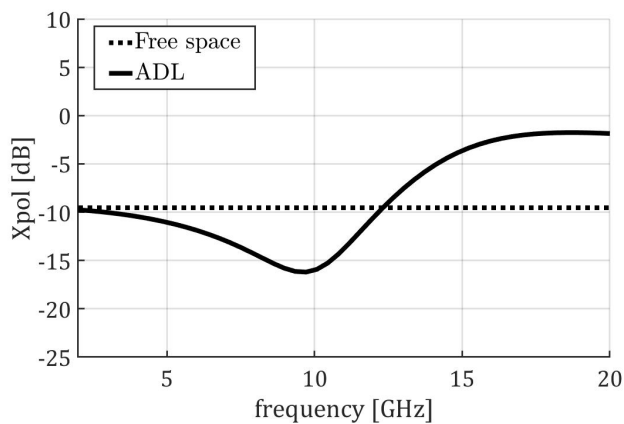

Figure 3.14: Cross polarization level in the diagonal plane with $\theta = 60°$ for an ADL above a Wheeler electric current.

3.3 Cross Polarization of Connected Arrays with ADL Superstrate

Artificial dielectrics have been introduced in Chapter 1 as a solution to improve the bandwidth and scanning performance of connected arrays. As discussed in section 2.2, these structures exhibit an

32
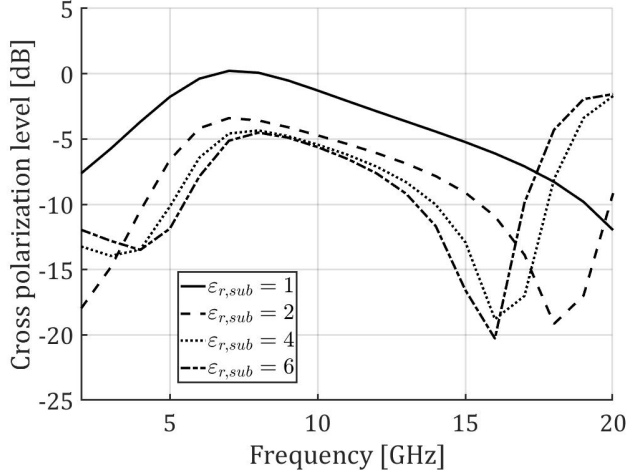
Figure 3.15: Cross polarization level of a connected dipole array topped by the ADL described in Tab. 2.1 and a backing reflector with a substrate of $\varepsilon_{r,sub}$.

anisotropic behavior, which results in a different refraction index for the TE and TM components. In addition, an ADL slab is not homogeneous. Those two factors may lead to an increase in the Xpol level. Indeed, high Xpol levels were observed for connected slots with ADL superstrates in [5].

Here, the example ADL described in subsection 2.2.4 is investigate to quantify the effects of the ADLs on the Xpol. An electric Wheeler current is shown in Fig. 3.13(a) and can be modeled as the circuit in Fig. 3.13(b). The corresponding Xpol for scanning to $60°$ in the D-plane in presented Fig. 3.14. It can be observed that the ADLs, because of its different properties for TE and TM modes, increase the Xpol with respect to the free space value, in particular at higher frequencies. This type of frequency dependence of the Xpol ratio is typical of connected array with ADL designs published in previous papers, e.g. [1].

It was observed, for the connected dipoles, that a beneficial effect on the Xpol reduction can be obtained by introducing a dielectric substrate with permittivity similar to the superstrate. An investigation on this aspect is also done for the ADLs. Fig. 3.15 shows the Xpol radiated by the connected dipole array in the presence of ADLs, when a substrated with different relative permittivities is considered. It can be observed that the substrate reduces the Xpol by up to 5 dB. However, the Xpol levels are still relatively high for most practical applications. Moreover, the effective permittivity of the ADL is frequency dependent, thus the beneficial effect of the substrate is limited to certain frequency ranges.

As seen in the previous section, an isotropic superstrate does not increase the Xpol beyond the free space value. On the contrary the ADL is characterized by anisotropic properties, which result in two different refractive indexes for TE and TM modes:

$$n_{TM} = \sqrt{\varepsilon_x \mu_y + (1 - \varepsilon_x/\varepsilon_z)\sin^2(\theta)} \tag{3.8}$$

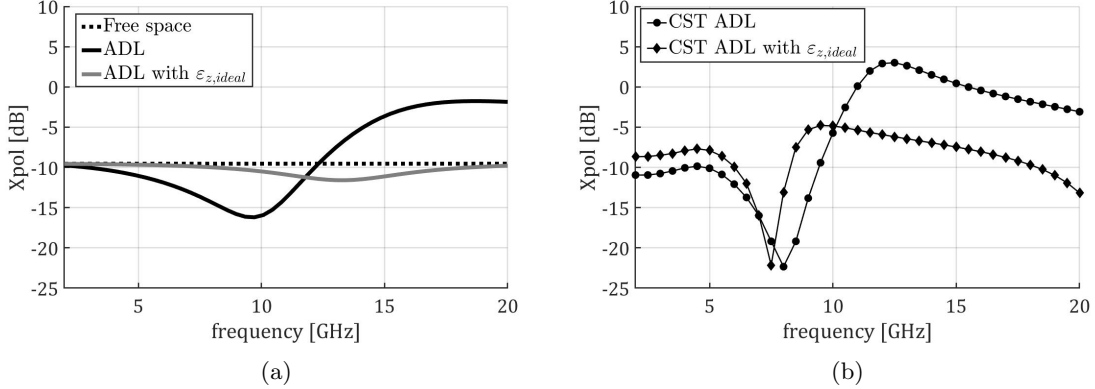$$n_{TE} = \sqrt{\varepsilon_y \mu_x + (1 - \mu_x/\mu_z)\sin^2(\theta)}. \tag{3.9}$$

33

Figure 3.16: Cross polarization level (D-plane, $\theta = 60°$) of (a) Wheeler current with and without ideal ε_z and (b) a dual-polarized connected slot array in CST with and without ideal ε_z.

These expressions are consistent with the plot in Fig. 2.8(b), which decrease as a function of the incidence angle θ. If one wishes to set n_{TM} equal to n_{TE}, the condition

$$\varepsilon_z = \varepsilon_x \mu_z = \varepsilon_y \mu_z \qquad (3.10)$$

must be verified. It can be noted that Equation 3.10 does not change n_{TE}, while it increases the values of n_{TM}, so that the two refractive indexes are equal and both decreasing with θ. The reduction of the refractive index with θ is key to prevent surface waves and thus scan blindness. Nevertheless, the TM0 surface wave is the first mode to generate scan blindness when scanning in the E-plane. Thus, if on one hand increasing n_{TM} would likely improve the polarization purity, on the other hand it will shift the surface wave resonance to lower frequencies, limiting the operating frequency or the scan range. Therefore, a trade off between Xpol and matching performance will be required when realistic designs are considered.

To demonstrate the effectiveness of the above mentioned strategy to reduce the Xpol, Fig. 3.16(a) shows the results for a Wheeler current radiating in the presence of an anisotropic slab with $\mu_x = \mu_y = 1$, $\mu_z = 0.24$, $\varepsilon_x = \varepsilon_y = 7.6$, which are the same parameters as the original ADL, but now introducing a z-component $\varepsilon_z = 1.9$, which satisfies Equation 3.10. It is apparent that the increase in Xpol due to the ADL is completely removed by the introduction of ε_z. The ideal anisotropic slab now behaves similar to an isotropic slab in terms of polarization performance.

To confirm this observation, Fig. 3.16(b) considers the ADL placed on top of the dual polarized connected slot array introduced in the previous section, simulated with the commercial solver CST Microwave Studio. The simulation in CST is carried out assuming vacuum as host medium for the ADL and changing the host medium as a non-magnetic material with $\varepsilon_x = \varepsilon_y = 1$ and $\varepsilon_z = 1.9$. The increase of ε_z causes a significant reduction of Xpol by up to 8 dB. However, the Xpol is not lower than the typical free space level of -9.5 dB. This can be explained with the fact that the curves in Fig. 3.16(a) assume constant effective parameters over the entire frequency band. However, for the large bandwidth under investigation (10:1), the effective parameters of the ADL are dispersive and cannot be considered constant with frequency. Moreover, Fig. 3.16(a) refers to single polarized current, while Fig. 3.16(b) considers dual-polarized slots, where the mutual coupling

between orthogonal port can lead to different Xpol levels.

A possible strategy to increase the value of ε_z without affecting the other parameters of the tensor is presented in the next Chapter and consists of including vertical vias, to realize a wire medium.

Chapter 4

Wire Medium

4.1 Method of Moments (MoM) Soltion for Wire Wedium

The previous Chapter described the cause of high cross-polarization level in artificial dielectrics and it also described a possible solution: increasing the z-component of effective permittivity tensor (ε_z). One possible way to control the ε_z without affecting all the other components of the tensor is by generating vertical currents. This can be achieved by vertical metallic wires interacting with the incident plane wave, such as the rod medium described in [47,48]. These rods are metallic cylinders in a host medium, however for the analysis of the medium a square rod is used as seen in Fig. 4.1(a). These rods, i.e. wires, are placed in a square lattice as shown in Fig. 4.1(b). The combination of the host medium and the wires is named the wire medium. First, a Method of Moments (MoM) analysis is performed for the retrieval of the reflection coefficients of the medium.

4.1.1 Integral Equation Definition

For the analysis, the wire is replaced by equivalent surface currents on the surface of the wire, S. The surface only supports equivalent electric currents, whereas the equivalent magnetic currents are not present as a result of the boundary conditions, which state that the tangential component of the electric field is equal to zero on a PEC surface. The total electric field is a superposition of the incident electric field without the scattering object, $\vec{e}_i$, and the scattered field by the equivalent currents, $\vec{e}_s$:

$$\vec{e}_{total}(\vec{r}) = \vec{e}_i(\vec{r}) + \vec{e}_s(\vec{r}) = 0, \quad \forall \vec{r} \in S \tag{4.1}$$

The equivalent current, $\vec{j}(\vec{r'})$, is defined on the points $\vec{r'}$ over the surface S. Utilizing the Green's function, the scattered field $\vec{e}_s$ is represented by the volume integral over the Green's function weighted by the surface current:

$$\vec{e}_s(\vec{r}) = \iiint_V \underline{\underline{g}}(\vec{r}, \vec{r'}) \vec{j}(\vec{r'}) d\vec{r'} \tag{4.2}$$

where $\vec{r}$ and $\vec{r'}$ are respectively the observation and source points, $\underline{\underline{g}}(\vec{r}, \vec{r'})$ is the free space dyadic Green's functions for the electric field from an electrical current. With the definition for the
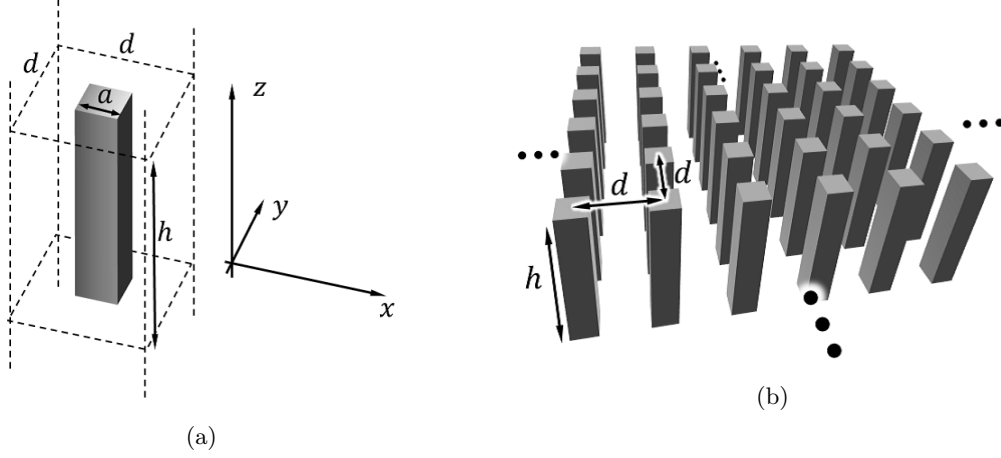
(a)

(b)

Figure 4.1: (a) Unit cell geometry of the wire medium which is placed in (b) a square infinite lattice.

scattered field, the integral equation (IE) is defined over the infinite volume V bounding the entire array of metal vias shown in Fig. 4.1(a):

$$\iiint_V \underline{g}(\vec{r}, \vec{r'})\vec{j}(\vec{r'})d\vec{r'} = -\vec{e}_i(\vec{r}) \quad \forall \vec{r} \in S \,. \tag{4.3}$$

The incident field, $\vec{e}_i(\vec{r})$, is a generic plane wave and thus can be split into its two transverse components, the transverse magnetic (TM) and the transverse electric (TE) wave:

$$\vec{e}_i(\vec{r}) = \vec{e}_{i,TM}(\vec{r}) + \vec{e}_{i,TE}(\vec{r}) = \left(\frac{V_{TM}}{d}\hat{\theta} + \frac{V_{TE}}{d}\hat{\phi}\right)e^{-jk_{x0}x}e^{-jk_{y0}y}e^{jk_{z0}z} \,. \tag{4.4}$$

The propagation constants along the three axis are defined as $k_{x0} = k_0\sin(\theta)\cos(\phi)$, $k_{y0} = k_0\sin(\theta)\sin(\phi)$ and $k_{z0} = k_0\cos(\theta)$, where k_0 is the wavenumber in the homogeneous isotropic medium which hosts the wires. The angles θ and ϕ are the incidence angles for the impinging plane wave.

The field can be projected on the Cartesian coordinate system, which will be used later for the definition of the reflection and transmission coefficients of the wire medium:

$$e_{i,x} = \left(\frac{V_{TM}}{d}\cos(\theta)\cos(\phi) - \frac{V_{TE}}{d}\sin(\phi)\right)e^{-jk_{x0}x}e^{-jk_{y0}y}e^{jk_{z0}z} \tag{4.5}$$

$$e_{i,y} = \left(\frac{V_{TM}}{d}\cos(\theta)\sin(\phi) - \frac{V_{TE}}{d}\cos(\phi)\right)e^{-jk_{x0}x}e^{-jk_{y0}y}e^{jk_{z0}z} \tag{4.6}$$

$$e_{i,z} = -\frac{V_{TM}}{d}\sin(\theta)e^{-jk_{x0}x}e^{-jk_{y0}y}e^{jk_{z0}z} \,. \tag{4.7}$$

37

4.1.2 Current Distribution

The equivalent current distribution $\vec{j}(\vec{r})$ is represented as a sum of the contributions of each wire in the infinite array:

$$\vec{j}(\vec{r}) = \sum_{n_x=-\infty}^{\infty} \sum_{n_y=-\infty}^{\infty} \vec{j}_0(x - n_x d, y - n_y d, z) e^{-jk_{x0}n_x d} e^{-jk_{y0}n_y d}. \tag{4.8}$$

The current distribution of the unit cell can be expressed in terms of an ad-hoc basis function. In general a set of basis functions are used to describe the current distribution, but a single basis function is sufficient for this problem. The wire is assumed to be thin compared to its length and short with respect to the wavelength, thus $h \ll \lambda_{host}$ and $a \ll h$. Under this assumption, the currents on the surfaces in the xy-plane at $h/2$ and $-h/2$ are small compared to the current along $\hat{z}$ and thus they are neglected. The current can be then expressed as

$$\vec{j}_0(\vec{r}) = I_0 b(\vec{r}) \hat{z} \tag{4.9}$$

where $\vec{b}$ is a known distribution while I_0 is an unknown coefficient.

Different basis functions could be used to describe the current distribution along $\hat{z}$. Here the inverse edge singular distribution is used to model the current [49]. The inverse edge singular basis function is defined as

$$b(\vec{r}) = \frac{2}{\pi h} \sqrt{1 - \left(\frac{2z}{h}\right)^2} \, \text{rect}_{[-h/2, h/2]}(z) t(x, y). \tag{4.10}$$

The basis function is comprised of a function dependent only on z and a transverse distribution depended on x and y. The transverse current distribution is given by two rectangular functions which define the surface of the wire:

$$t(x, y) = [\delta(x - a/2) + \delta(x + a/2)] \, \text{rect}_{[-a/2, a/2]}(y) + \tag{4.11}$$
$$[\delta(y - a/2) + \delta(y + a/2)] \, \text{rect}_{[-a/2, a/2]}(x).$$

The normalized basis function is shown in Fig. 4.2a, for a wire with a height of $h = 3$ mm. The Fourier transform of the current distribution is going to be used for the spectral domain method, which can be found in closed form as

$$B(k_x, k_y, k_z) = \frac{J_1\left(\frac{k_z h}{2}\right)}{k_z h} T(k_{xm}, k_{ym}) \tag{4.12}$$

where the Fourier Transform of the transverse distribution is given by

$$T(k_{xm}, k_{ym}) = 2a \left(\cos\left(\frac{k_{xm}a}{2}\right) \text{sinc}\left(\frac{k_{ym}a}{2}\right) + \cos\left(\frac{k_{ym}a}{2}\right) \text{sinc}\left(\frac{k_{xm}a}{2}\right) \right). \tag{4.13}$$
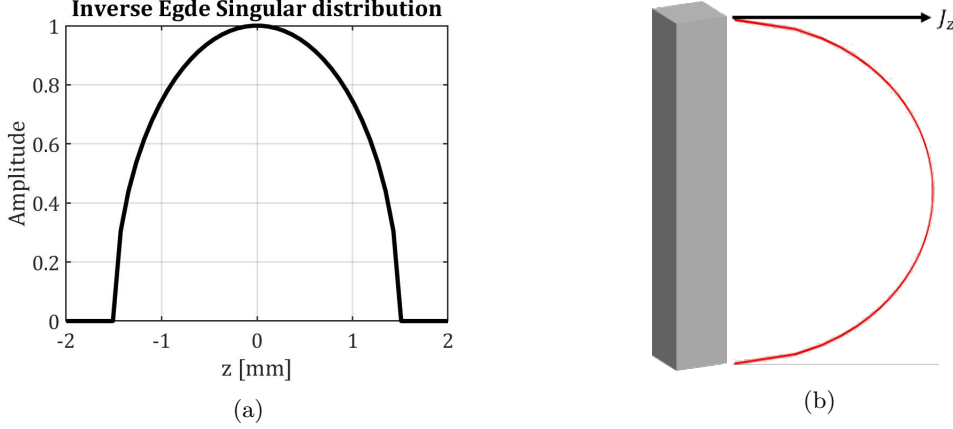
Figure 4.2: Inverse edge-singular basis function of example wire with $h = 3mm$.

4.1.3 Solution of the Integral Equation

The integral equation is solved with the use of spectral domain MoM. By substituting the equivalent current expansion with the basis function into the integral equation leads to:

$$\iiint_V \sum_{n_x=-\infty}^{\infty} \sum_{n_y=-\infty}^{\infty} \underline{\underline{g}}(\vec{r}, \vec{r'}) I_0 b(x' - n_x d, y' - n_y d, z') \hat{z} e^{-jk_{x0}n_x d} e^{-jk_{y0}n_y d} \vec{dr'} = -\vec{e}_i(\vec{r}). \quad (4.14)$$

To solve the integral equation some algebraic steps are required, which are reported in Appendix B. The solution is a integral equation which is in the spectral domain an is only over the wave number in the z-direction:

$$\frac{1}{2\pi d^2} I_0 \int_{-\infty}^{\infty} \sum_{m_x=-\infty}^{\infty} \sum_{m_x=-\infty}^{\infty} B(k_{xm}, k_{ym}, k_z) B(-k_{xm}, -k_{ym}, -k_z) G_{zz}(k_{xm}, k_{ym}, k_z) dk_z$$

$$= -\frac{V_{TM}}{d} \sin(\theta) B(-k_{x0}, -k_{y0}, k_{z0}). \quad (4.15)$$

The function G_{zz} is the zz-component of the dyadic spectral Green's function, which is given by

$$\underline{\underline{G}}(k_x, k_y, k_z) = \frac{j\zeta_0}{k_0} \begin{bmatrix} k_0^2 - k_x^2 & -k_x k_y & -k_x k_z \\ -k_y k_x & k_0^2 - k_y^2 & -k_y k_z \\ -k_z k_x & -k_z k_y & k_0^2 - k_z^2 \end{bmatrix} \frac{1}{k_0^2 - k_x^2 - k_y^2 - k_z^2}. \quad (4.16)$$

To determine the still unknown coefficient I_0, a Galerkin projection is executed. The test function for this projection is the same as the basis function defined in Equation 4.12. This results in an equation for the unknown coefficient I_0 as

$$I_0 = \frac{V_0}{Z_{self}} = \frac{-\frac{V_{TM}}{d} \sin(\theta) B(-k_{x0}, -k_{y0}, k_{z0})}{\frac{1}{2\pi d^2} \int_{-\infty}^{\infty} \sum_{m_x=-\infty}^{\infty} \sum_{m_y=-\infty}^{\infty} B^2(k_{xm}, k_{ym}, k_z) G_{zz}(k_{xm}, k_{ym}, k_z) dk_z} \quad (4.17)$$

39

where V_0 is the forcing term and the self impedance Z_{self} is written in terms of a sum of integrals over k_z for every Floquet mode. A semi-analytical method is developed for the integrals to be computed for Z_{self}. The derivation for the semi-analytical approach is described in Appendix C. The final expression of the self impedance is found as

$$Z_{self} = \int_\infty^\infty B(k_{xm}, k_{ym}, k_z)^2 G_{zz}(k_{xm}, k_{ym}, k_{zm}) dk_z =$$

$$\left(-j\frac{h\zeta k_0}{2} \left[\pi \left(\frac{1}{K^2} \right)^{3/2} I_0(K)^2 - \frac{64 \, _2F_3(1, 2; 3/2, 5/2, 7/2; K^2)}{45\pi} \right] \right. $$

$$\left. +j\frac{2\zeta}{k_0 h} \left[-\pi\sqrt{\frac{1}{K^2}} I_0(K)^2 + \frac{8 \, _2F_3(1, 1; 1/2, 3/2, 5/2; K^2)}{3\pi} \right] \right) T(k_{xm}, k_{ym}), \tag{4.18}$$

where $K = \frac{h^2}{4}(k_{xm}^2 + k_{ym}^2 - k_0^2)$, I_0 is the modified Bessel function of the first kind and $_2F_3$ is the generalized hyper geometric function. This closed form solution is only valid for the higher order modes, that verify the condition $\Re(K^2) > 0$. For the fundamental mode, $m_x = m_y = 0$, $\Re(K^2) < 0$ and thus the integral must still be evaluated numerically.

All parameters for the scattered field are now defined, therefore the reflection and transmission coefficients can be determined.

4.1.4 Reflection and Transmission Coefficients

The radiating scattered field is evaluated from the fundamental mode, $m_x = 0$ and $m_y = 0$. The higher order modes correspond with the reactive field. Therefore, the scattered field at height z can be evaluated with Equation 4.19, where $G_{\chi z}$ is the spectral Green's function which relates the electric current along $\hat{z}$ to the electric field along $\chi = x, y$ or z.

$$e_{s,\chi}(x = 0, y = 0, z) = \frac{I_0}{2\pi d^2} \int_{-\infty}^\infty B(k_{x0}, k_{y0}, k_z) G_{\chi z}(k_{x0}, k_{y0}, k_z) e^{-jk_z z} dk_z \tag{4.19}$$

$$e_{s,\chi}(x = 0, y = 0, z) = \frac{I_0}{2\pi d^2} \int_{-\infty}^\infty B(k_{x0}, k_{y0}, k_z) \left(\frac{-j\zeta}{k_0} \begin{bmatrix} -k_{x0}k_z \\ -k_{y0}k_z \\ k_0^2 - k_z^2 \end{bmatrix} \frac{1}{k_0^2 - k_{x0}^2 - k_{y0}^2 - k_z^2} \right) e^{-jk_z z} dk_z \tag{4.20}$$

The poles of the integral in Equation 4.20 are located at $k_{z0} = \pm\sqrt{k_0^2 - k_{x0}^2 - k_{y0}^2}$. Applying the residue theorem and after some algebraic steps the expression for the scattered field is found as

$$e_{s,\chi}(x = 0, y = 0, z) = \frac{I_0}{2\pi d^2} B(k_{x0}, k_{y0}, k_z) \left(\frac{-j\zeta}{k_0} \begin{bmatrix} -k_{x0}(\pm k_{z0}) \\ -k_{y0}(\pm k_{z0}) \\ k_0^2 - k_z^2 \end{bmatrix} \frac{1}{k_0^2 - k_{x0}^2 - k_{y0}^2 - k_z^2} \right) e^{-jk_z z} dk_z \tag{4.21}$$

Now that the expression for the incident field and the scattered field are known the reflection and transmission coefficients for the TM or TE components, can be found as

$$\Gamma_{Ti} = \frac{e_{s,Ti}(z = h/2)}{e_{i,Ti}(z = h/2)} \tag{4.22}$$

40

$$T_{Ti} = \frac{e_{s,Ti}(z = -h/2) + e_{i,Ti}(z = -h/2)}{e_{i,Ti}(z = h/2)} . \tag{4.23}$$

4.2 Validation of the MoM

For the validation of the method the structure is simulated in a commercial full-wave solver to obtain the reflection and transmission coefficients under generic plane-wave incidence. The geometric parameters of the wire medium are: $d = 0.225\lambda_0$, $a = 0.1d$ and $h = 0.1\lambda_0$, with $f_0 = 10$ GHz. As seen in Fig. 4.3, both the amplitude and phase of the coefficients from the MoM and those obtained by the commercial solver are in agreement.
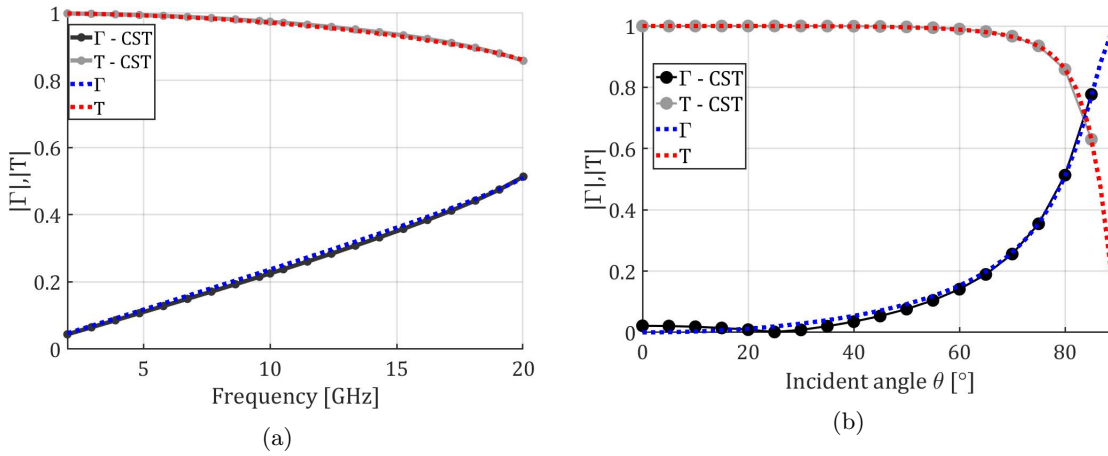
Figure 4.3: Validation of MoM for square wires with commercial solver.

In this chapter a square wire medium was analyzed, but for fabrication in PCB designs cylindrical vias are used. To transfer from the square wire of width a_s to the cylindrical via, the area on the square wire is equated to that of a cylindrical via. From that an equivalent diameter a_c for the cylindrical via is obtained, with the conversion formula:

$$a_c = \sqrt{\frac{4}{\pi}} a_s. \tag{4.24}$$

A comparison is made between the parameters of the square via with the commercial solver CST and the MoM and a simulation with a cylindrical via with the new diameter of the wire in Fig. 4.4. It is seen that the method is valid for the TM-wave, but there is a small TE component present. That TE component is caused by the fact that the wires, because of they are not infinitely thin, can reflect small portions of the x- and y-components of the incident field. The scattering due x- and y-oriented currents is neglected in our model, but is accounted for in the CST simulations in Fig. 4.5, causing a small reflection.

The wire medium was introduced to increase the z-component of the effective permittivity tensor. However, when considering the effective parameters of the wire medium with the use of this
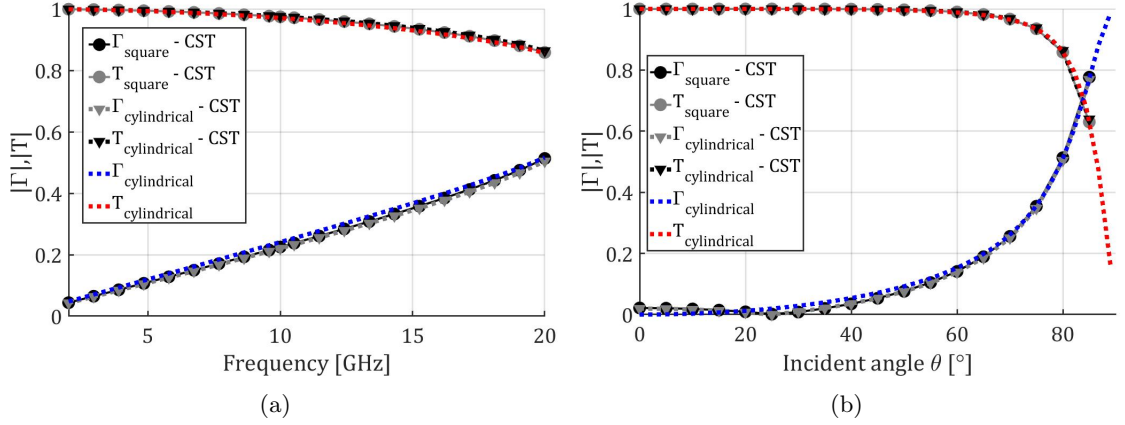
Figure 4.4: Validation equivalent diameter for cylindrical wires with commercial solver.
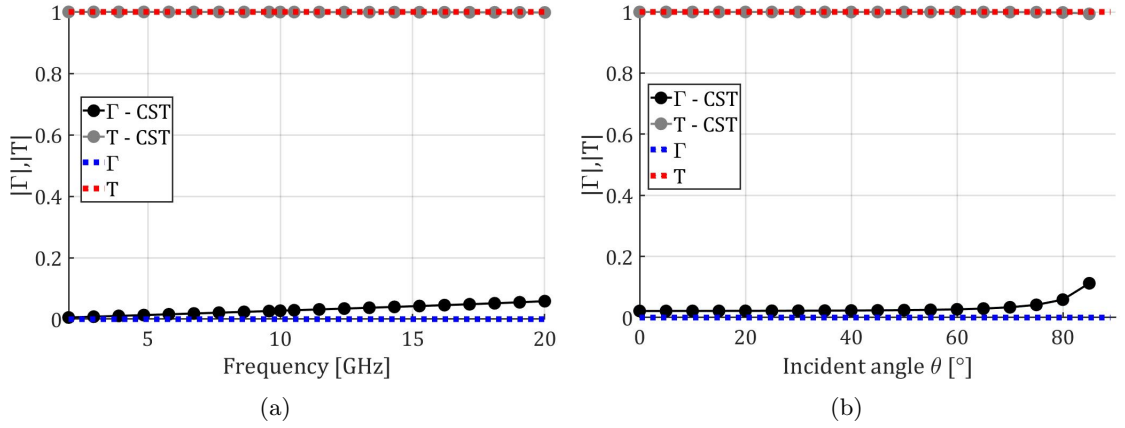
Figure 4.5: Validation of MoM with commercial solver for the TE component of incident waves.

method, it must be noted that no TE component is considered because the assumption that no horizontal currents are present. The result of this assumption is therefore that the homogenization method results in $\varepsilon_x = \varepsilon_y = \varepsilon_{host} = 1$. In addition, no loop currents are present, thus all terms of the effective permeability tensor are unaffected by the wire.

For the example wire presented previously the effective parameters resulting from the MoM are shown in Fig. 4.6. Here the effect is clearly seen and only an increase in ε_z is observed. It is shown that the wire medium offers a way to increase the permittivity along $\hat{z}$, without impacting the other parameters when a is small ($a < 0.02\lambda$). However, from simulations (Fig. 4.5) it is seen that a TE component is present in the reflection and transmission coefficients thus the method is slightly off for ε_x and ε_y.

For the design of the wire medium it is important to know what the key parameters are. Therefore it is necessary to understand the way the parameters d, h and a influence the permittivity.
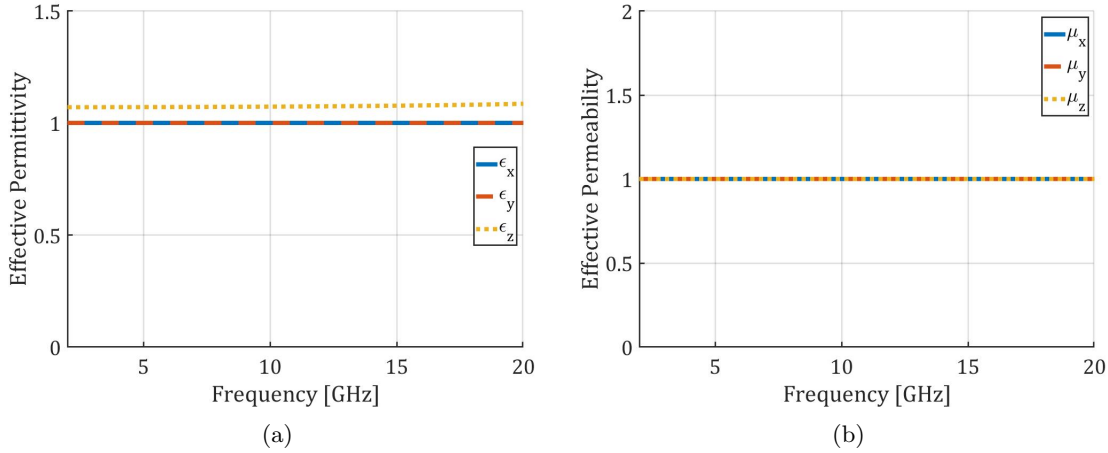
Figure 4.6: Effective (a) permittivity and (b) permeability of the wire medium with $h = 0.1\lambda_0$, $d = 0.225\lambda_0$ and $a = 0.1d$.

Here the focus is on ε_z as it is the effective parameter the wire medium is designed for. The effect of an increase in the thickness a of the wire is shown in Fig. 4.6(a). in addition, the height h is varied in Fig. 4.6(b)and finally the effect of the spacing is shown in Fig. 4.6(c).

From the figures it is clear that decreasing d, thus increasing the density, increases the permittivity significantly, which makes this parameter highly influential. Moreover, increasing the thickness yields also a higher permittivity. However this increase also introduces a larger area which increase the interaction with the TE wave. That interaction is not modeled, thus introduces uncertainty. The thickness is even increased to values larger than 0.1λ, where the horizontal currents cannot be neglected anymore. Lastly, the increase in height also has a positive effect on the permittivity. Increasing the length of the wire brings it closer to the resonance frequency of the wire, that is seen by the rapid increase of the permittivity. Along with the wire, the thickness of the slab increases as well, because the thickness is set as $2h$. Therefore, the major parameters to determine the permittivity are the density and the height, which are also the most convenient to design.

In addition to the change of the parameters of the wire, the wire medium is suspended in a dielectric host medium. The equivalent permittivity of the slab is at least the effective permittivity of the dielectric. Here we add two sections of a thickness $h/2$, one above and one below the wire filled with vacuum. Therefore, the equivalent permittivity is at least the average of the two$((\varepsilon_{r,diel}+1)/2)$. The change of the permittivity of the host medium is shown in Fig. 4.6(d). The higher dielectric constant of the medium results in a higher effective permittivity as expected, but the majority of the ε_z increase is caused by the presence of the dielectric it self with this wire medium. The increase from $\varepsilon_r = 1$ to $\varepsilon_r = 3$ is equivalent to an increase in electrical height of approximate 9%.

43
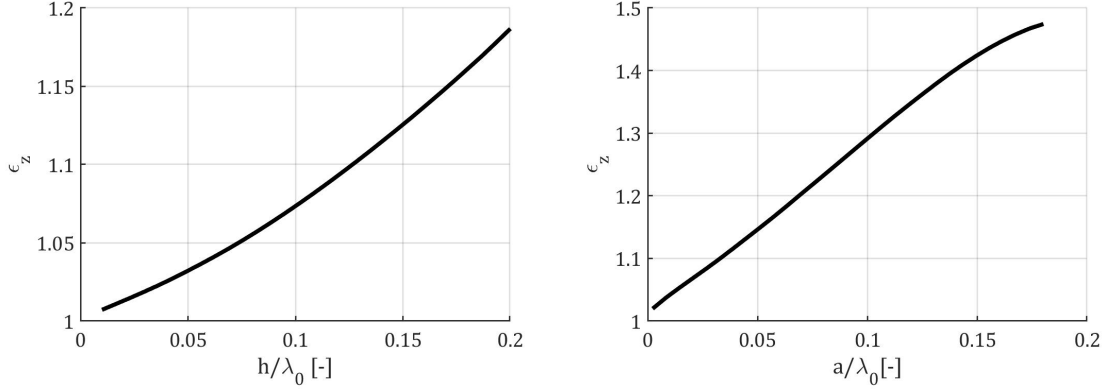
(a) Variation of wire heigth with $d = 0.225\lambda_0$ and $a = d/10$.

(b) Variation of wire thickness with $d = 0.225\lambda_0$ and $h = 0.1\lambda_0$.
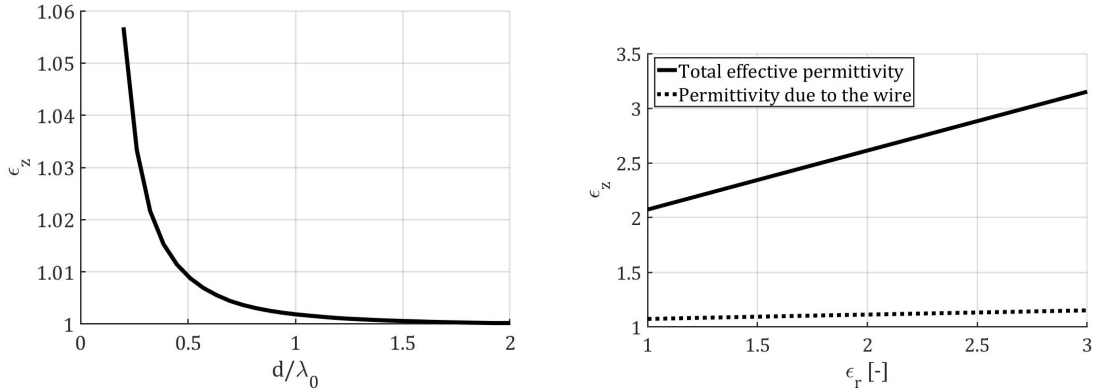
(c) Variation of wire spacing with $a = 0.1\lambda_0$ and $h = 0.1\lambda_0$.

(d) Variation of host medium permittivity with $d = 0.225\lambda_0$, $a = d/10$ and $h = 0.1\lambda_0$.

Figure 4.7: The effect of variation of several parameters of the wire medium on the z-component of the permittivity.

4.3 Top-Hat Loaded Wire Medium

It was shown that the wire medium with a height of $h = 0.1\lambda_0$ is effective, however in previous radome designs [1], [32] and [33] the typical height of dielectric layers to embed the wire medium as vias is limited to as small as $0.025\lambda_0$. This small height reduces the effectiveness of the wire medium as it is one of the two major parameters to increase the permittivity. In addition, the vias require small via pads (with radius $= a/2 + 0.1$mm) at the ends for manufacturing, which will increase the effect of the medium on the other effective parameters. In order to mitigate these undesired consequences of the wire medium on the other effective parameters and to enable manufacturability, the integration of the wires with the horizontal patches of ADLs is investigated, as shown in Fig. 4.8.

44
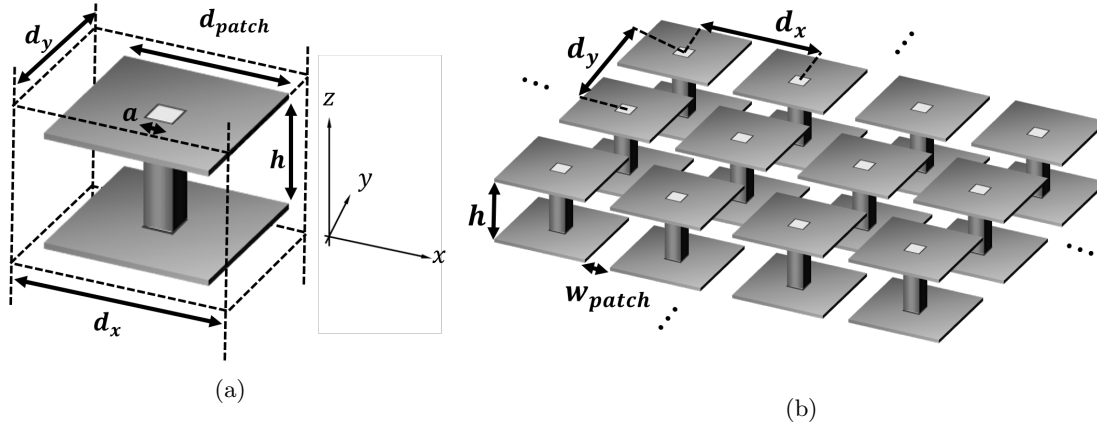
Figure 4.8: (a) Top-hat loaded wire medium geometry of unit cell with (b) the square lattice.

The result is to place the patches at the edges of the wires, which are thus integrated in the design of the ADL as discussed in section 2.2. Since the currents on the patches and on the wire connecting them are orthogonal, the two effects can be treated separately. This means, that the current distribution on the patches that is responsible for the increase of ε_x and ε_y does not interact with the vertical pins. However, the patches still have an effect on the current distribution on the wire.

From simulations it is shown that the patches increase permittivity along $\hat{z}$ due to the presence of the wires. Therefore the patches must alter the current distribution. Moreover, the patch size directly influences the permittivity as seen in Fig. 4.9(a). A similar increase in permittivity is achieved for a wire medium without the patches by increasing the height of the wire. The same permittivity can be reached with a shorter wire with patches instead of increasing the height of the wire. In addition, there is no influence from the wire on the effective permittivity in the x- and y-direction and not on the permeability in general.

The increased permittivity seems to be caused by a change in the current distribution. There is a capacitive loading of the wire as a result of the presence of the patches, so that the wire with patches acts like a longer wire. A current flow as shown in Fig. 4.9(b) is likely present. Therefore, the medium is now called the top-hat loaded wire medium, which was already known from dipole antennas. The capacitive loading increases the electrical length of the wire, i.e. the current at the end of the wire ($z = -h/2$ of $z = h/2$) does not have to be equal to zero. That larger effective height results in a increases of the the z-component of the effective permittivity tensor. Therefore, wires with a smaller physical size can be utilized to achieve the same performance as longer wires.

When integrating this top-hat loaded wire medium structure into an ADL design, the period of the wires, d, is restricted by the period of the patches, p. The top-hat loaded wire medium can thus have a period as small as the period of the patches, however it can then only increase in integer variations of the ADL period: $d = \{p, 2p, 3p, ..., Np\}$, with no specific limit to N but the effect on the permittivity will decrease rapidly. Therefore, it is advised to use the wire medium with the same or very similar period as the horizontal ADL.

In the wire medium considered, the wire length is too small compared to the wavelength, thus the structure is far from the resonance. However, the top-hat loaded wire medium performs as a
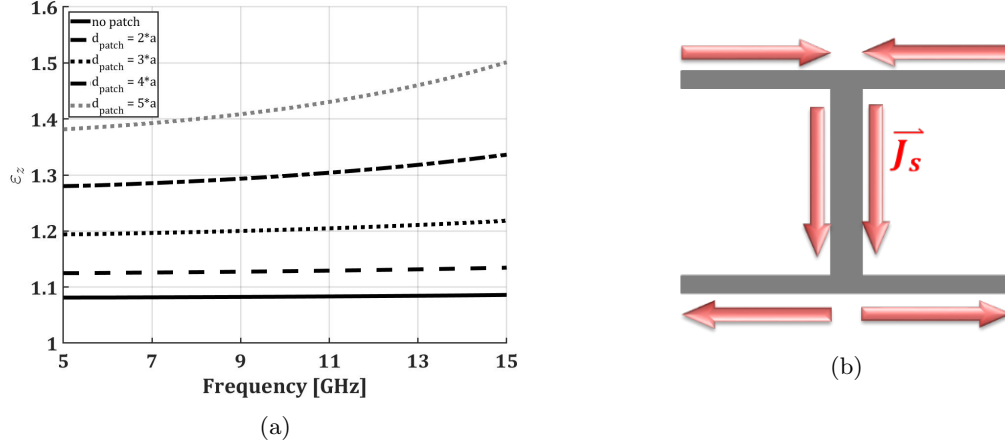
45

Figure 4.9: (a) Permittivity in $\hat{z}$ of Top-hat Loaded wire medium with increasing patch size (b)Presumed current on top-hat loaded Wire Medium.

wire medium with an electrically longer wire, thus a resonance behavior can occur even when the height is not that large compared to the wavelength. The resonance is one of the limitations in the design that puts a constraint on the maximum size of the patch and the height of the wire.

4.4 Improvement of Cross Polarization Levels with Wire Medium

It was seen that the ADL is the cause of the cross polarization level and that the way of reducing that level is by increasing the permittivity in the z-direction, which can be achieved with the wire medium. From the parameter of the ADL, as shown in section 3.3, an ideal value for ε_z was extracted and implemented: $\varepsilon_{z,ideal} = \varepsilon_x \mu_z = 1.9$. That value is integrated in the host medium, which is now anisotropic because $[\varepsilon_x, \varepsilon_y, \varepsilon_z] = [1, 1, \varepsilon_{z,ideal}]$.

As shown above the wire medium can be implemented in two ways: as a wire or the top-hat loaded wire. With the method for the wire medium a design can be obtained by limiting the height of the wire to the available space in-between the patch layers of $d_z \approx 0.57$ mm, therefore a maximum layer height of the wire is set to be $h_{max} = 0.5$ mm. As the height is one of the key parameters to achieve the permittivity, it is hold at its maximum. Thre layers of the wire medium are able to be used. To increase sensibly ε_z, the period of the wire medium must be reduced to 0.4 mm, however this results in a unfeasible thickness for the wire, to satisfy $a/d \ll 1$. Even if this could be manufactured, the medium results in a relatively small ε_z of around 1.3. In addition, with this size of the wire with respect for the periodicity a/d the analysis method may not be representative.

Therefore, the aim is to implement the top-hat loaded wire medium as the contact with the patches increase the electrically seen height, thus increasing the permittivity. Three layer of the top-hat loaded wire medium are implemented in the design, as shown in Fig. 4.10(a). The period of the wires are set equal to the period of the ADL as this maximizes the permittivity. The thickness of the wire is set to a thickness that is able to be manufactured, thus $a = 0.2$ mm which is small

46
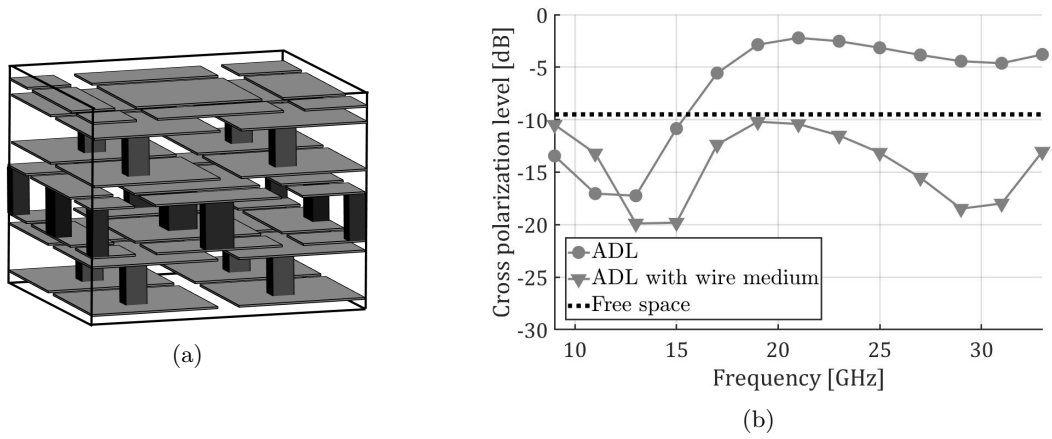
Figure 4.10: (a) Impression of the ADL design with top-hat loaded wire medium and (b) the cross polarization level with the wires implemented, with parameters shown in Tab. 2.1.

compared to the wavelength.

Implementing of the top-hat loaded wire medium clearly provides a better cross polarization level, Fig. 4.10(b). The effectiveness of the wire medium is shown by a cross polarization level decrease of 8 dB with respect to the ADL without vias, seen in Fig. 4.10b, remaining below -10 dB throughout the bandwidth. In the next chapter this wire medium concept will be implemented in a complete design and optimized.

47

Chapter 5

Unit cell design of array

5.1   Preliminary Design

As mentioned in section 1.3, ultra-wideband arrays with low cross polarization are desired for communication applications, especially for the sattelite communication. An array design to cover simultaneous the Ku- and Ka-transmission bands was already performed in [5]. That unit cell design used the ideal δ-gap feeds and an impedance transformer consisting of ADL layers in free space. In this section the unit cell design is shortly discussed and this design evolves during the chapter to include a dielectric layer, the wire medium and all manufacturing layers, such as bonding layers and support layers.

The design starts with the impedance transformer which consists of ADLs. The transformer is used as for wide-angle impedance matching, with the ADLs the free space impedance ($Z_0 = 377\Omega$) is transformed to the feed impedance $Z_{slot} = 80\Omega$. For a design of such impedance matching transformer several possibilities can be used such as: a quarter wave, exponential and Chebyshev transformer. In the design a two-section Chebyshev transformer is implemented, because it satisfies the bandwidth requirement and its total height is smaller than an exponential transformer.

The two sections sections of the transformer are designed with the use of ADLs. From the analytical expresseions discussed in section 2.2 the S-parameters for an incident wave are obtained, Those S-parameters are then used to obtain an equivalent permittivity. The geometric parameters of the ADLs are adapted in order to generate a section such that the equivalent effective parameters are as required from the transformer. An iteration over the design of the sections is performed to account for the change of the permittivity by addition of the other section, this iteration is described in [5]. The procedure is implemented for both sections and specifies all the geometrical parameters for the radome.

Next, the geometric slot parameters are determined be optimizing the parameters for to obtain an input impedance which is matched well to the feed impedance. From that optimization the connected slot array with the transformer and the backing reflector are determined. The distance to the ground plane is reduced as well, when reducing the distance to the ground plane a parallel plate wave is guided in the E-plane of the array between the slot plane and the ground plane, therefore walls in-between adjacent slots are implemented in the backing reflector. These walls are changed to through hole vias when extending the design to a dual polarized array.

With the aim of implementing the top-hat loaded wire medium into the design an alternative
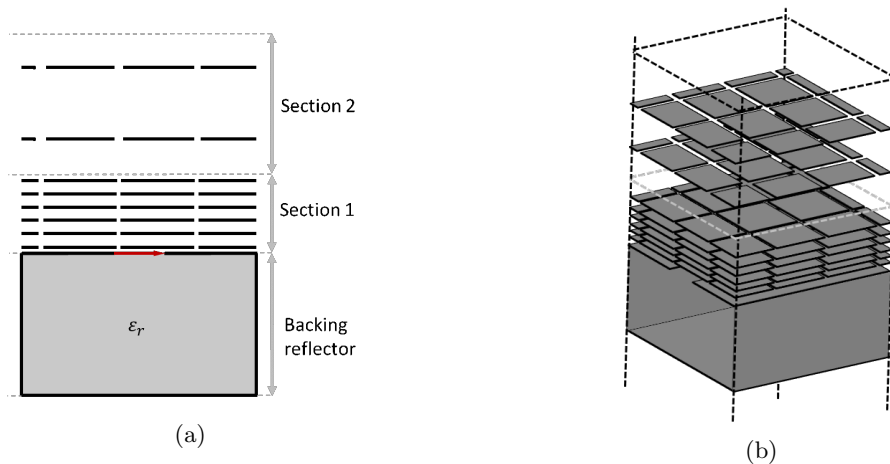
Figure 5.1: (a)side view and (b)3D sketch of the unit cell of the array
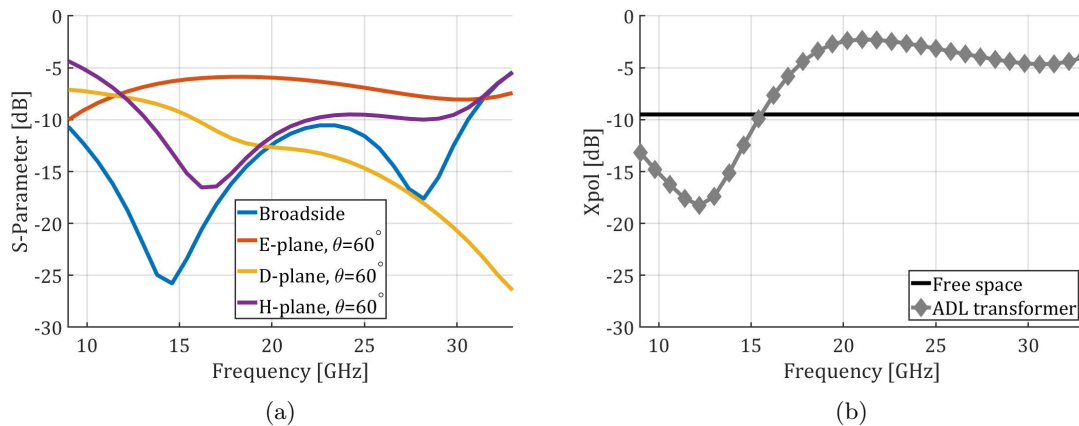
Figure 5.2: (a) Reflection coefficient of the connected slot array design with an ADL in free space and (b) the corresponding Cross polarization level for the D-plane scanning to 60°

design to [5] is obtained with the same transformer. In contrast to the original design, the sections aren't optimized to contain the least number of ADLs, instead the design requires that all patches of the layers are aligned. This requirement is as a result of the desired implementation of the wire medium. In addition, first a single polarizaed connected slot array is considered. The result of this optimization is a transformer with eighth ADLs in free space, a sketch of this design is shown in Fig. 5.1. The geometric parameters of the design are presented in Appendix D in Tab. D.1.

The design obtains the require bandwidth and the desired minimal scan angle of 60°. The reflection coefficients of the array with a feed impedance of $Z_{slot} = 80\Omega$ for broadside and the main planes with scanning to $\theta = 60°$ are presented in Fig. 5.2(a). For broadside the reflection coefficient is lower than -10 dB for the entire band. Moreover, for scanning the array in the two
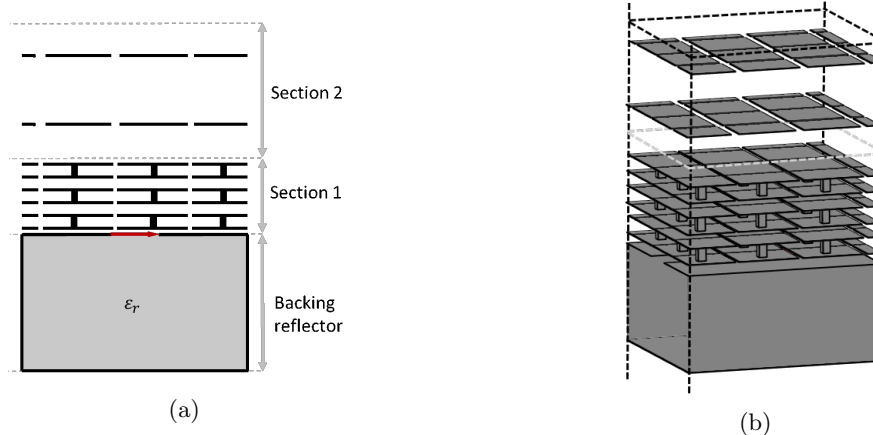
Figure 5.3: (a) top-hat loaded wire medium geometry of unit cell with (b) a 3D sketch.

main planes, the worst reflection coefficient is only -6 dB in the E-plane. However, as mentioned before the cross polarization of this unit cell is to high, which is shown in Fig. 5.2(b) for scanning in the diagonal plane to $\theta = 60°$. The level is easily below -10 dB for the Ku-band. However, the polarization purity is reduced in the Ka-band, where the Xpol level reaches beyond -5dB and for the center frequency even larger. This cross polarization was also seen in the original design, but is not desired. Therefore, the wire medium is implemented in the design.

5.2 Wire Medium in Free Space Design

In order to reduce the cross polarization the wire medium is implemented in the most dense section of the transformer, which is section 1. As that is the most dense section the introduction of the wire medium in that section has the largest effect due to the larger difference between the refraction index n_{TE} and n_{TM}.

No analytical procedure is available yet for assessment of the effect of the top-hat loaded wire medium at this moment, therefore a commercial solver (CST) is used to obtain the S-parameters and the cross polarization of the unit cell. As a starting point, each vertical aligned patch pair is connected with a wire to form three layers of top-hat loaded wires with the same periodicity as the patches, as shown in Fig. 5.3, the rest of the design parameters are not altered.

Using the obtained S-parameters of an isolated section 1, the effective parameters are extracted of this first section without the wire medium(Fig. 5.4(a)), from those parameters it is seen that the section adheres to the characteristics discussed in subsection 2.2.4. The same is extraction is performed with the ADL with the top-hat loaded wire medium(Fig. 5.4(b)). The parameters show that the wire medium only change the z-component of the effective permittivity. It is seen that the permittivity reaches around 2.1, this permittivity is higher than the ideal case where $\varepsilon_{z,ideal} =_x \mu_z \approx 7.9 \cdot 0.24 = 1.9$. That might introduce undesired effects.

The result of the large z-component of the permittivity is that n_{TM} is larger than n_{TE}. This does not have to be a negative result, but a large refraction index for the TM wave results in a shift of the TM_0 mode surface wave to a lower frequency. In case of this design, the resonance of a

50
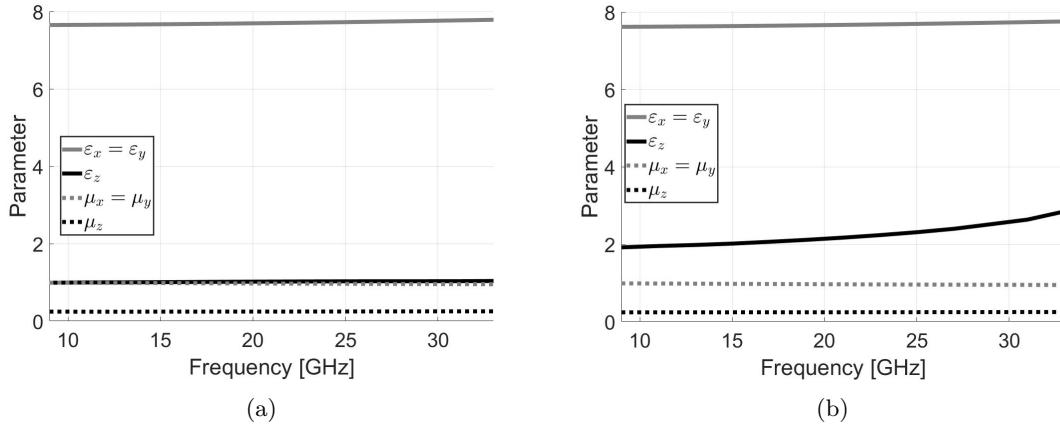
Figure 5.4: Effective parameters of the ADL in section 1 (a) without any wires and (b) with the top-hat loaded wire medium.
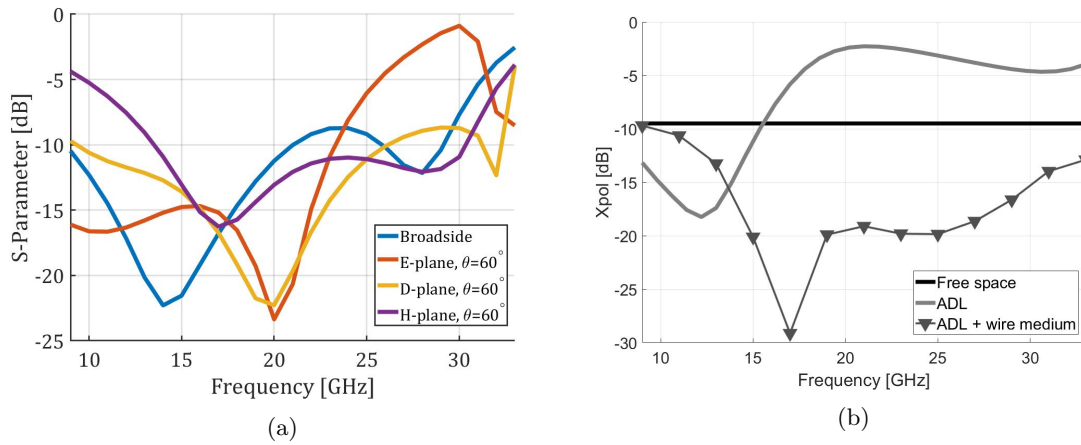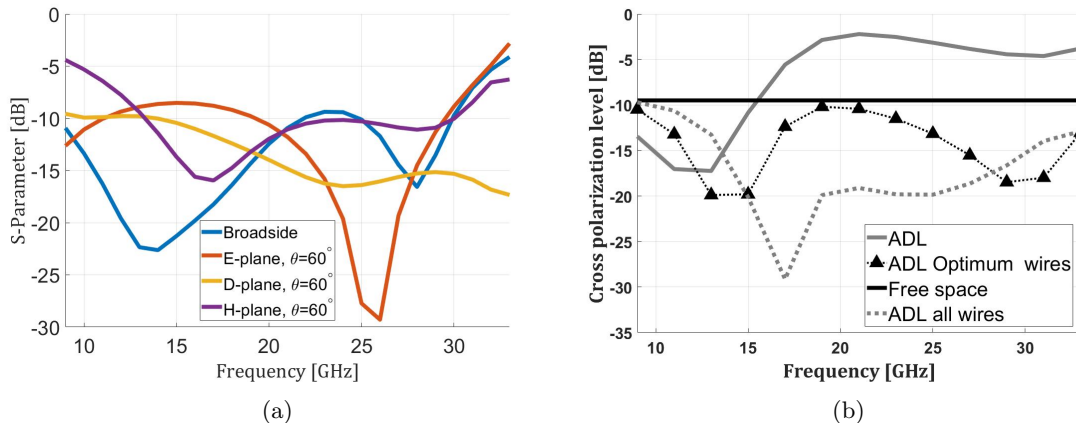

Figure 5.5: (a) S_{11} of the connected slot array with ADL and wire medium and (b) the corresponding Cross polarization level for the D-plane scanning to 60°

strong reflection is observed around 30 GHz(Fig. 5.5(a), this reflection indicates the TM0 surface wave is present, which causes scan blindness. For an design with a smaller scan angle this might be acceptable as the smaller angle pushes the resonance to a higher frequency. However, for this design this resonance is obviously not desired as it introduces scan blindness and provides undesired edge effects. Despite that resonance the cross polarization (D-plane, $\theta = 60°$) is reduced greatly by -10 dB, as shown by Fig. 5.5(b).

In order to reduce the Xpol level while still maintain the scan angle of 60° the z-zomponent of the effective permittivity obtained by the wires must be lowered. The period of the wires medium was shown to be one of the key parameters as well as the height of the wire. However, only the

51
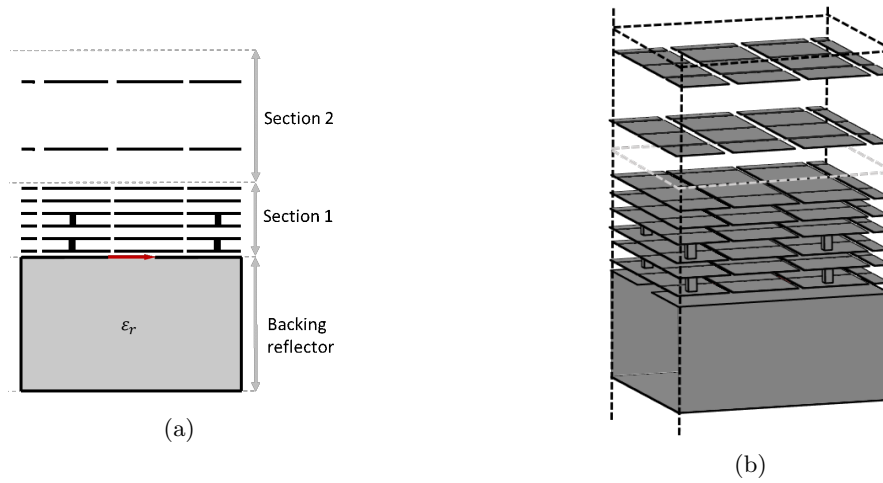
Figure 5.6: (a)A side view of the unit cell using ADLs in free space with optimized via placement and (b) a three dimensional sketch.
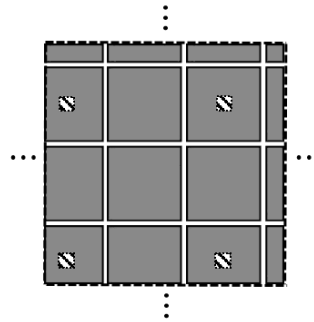
Figure 5.7: Top-view of the location of the vias in the unit cell with optimum wire medium.

period can be altered, because the height is set by the geometrical parameters of the ADL. The period of the wires is thus reduced and optimized with several iterations of simulations in CST. The simulation show that only increasing the period does not yield the lowest cross polarization without the surface wave. Therefore, the number of layers containing the vias is also reduced from three layers to two, as shown in Fig. 5.6. The period of the wires is $p_{wire} = 2p_{adl}/3$, as shown in Fig. 5.7. This placement of the wire provides the spacing with an alternating characteristic. The infinite repetition of the unit cell results in "packets" of four wires placed periodical through the entire structure.

The optimization obtains a permittivity ε_z which is still different from the ideal case as would be desired form equating the refraction index for TE and TM waves, as described in section 3.3. The optimized structure is characterized by a lower permittivity in $\hat{z}$ than ideally would be implemented. In spite of that, the Cross polarization level for the diagonal plane scanning to 60° is still reduced significantly, as shown in Fig. 5.8(b). The cross polarization is lowered by at least 8dB and at some

Figure 5.8: (a) S_{11} of the connected slot array with the optimized wire medium and (b) the corresponding Cross polarization level for the D-plane scanning to 60° with optimised top-hat loaded wire medium

frequencies even around -12 dB. Moreover, the level is reduced to below the -10dB requirement thus satisfies the Xpol requirement. However, a small increase of about 4dB is observed at the low frequencies. That increased level is likely caused by the disperse ADL parameters, at lower frequencies the permittivity in the xy-plane (ε_x and $_y$) are lower, in addition the permeability in z is larger. This change over frequency results in a higher or lower ideal permittivity depending on the relative change between the permittivity and the permeability. In addition, the permittivity induced by the wires decay when reducing the frequency. Nonetheless, the top-hat loaded wire medium is shown to be used to reduce the Xpol of the array in the operating frequencies.

In addition to decreasing the cross polarization, the matching in the E-plane is improved compared to the case without the top-hat loaded wire medium, as shown in Fig. 5.8(b). The improvement is over the entire frequency range, but is largest around 26 GHz. The worst matching is still at the highest operating frequency (31 GHz), however, the reflection coefficient is still below -6dB which means that the design adheres to all the requirements. Thus, the unit cell with the top-hat loaded wire medium is well suited to reduce the cross polarization and provide adequate performance for wide band impedance matching for large scan angles of at least 60°.

5.3   Antenna PCB

The antenna PCB in [1] still used the ideal small gap feed. Th author extended the dual-polarized design to incorperate a feeding structure. The antenna is made by PCB manufacturing therefore separate layers are utilized. The unit cell of the antenna PCB is shown without the radome in Fig. 5.9(a). The antenna PCB consists of 3 major layers: the backing reflector layer, the stripline layer and the micro strip layer. The cavity formed by the backing reflector and the slot plane is shown in Fig. 5.9(b). The design is extended with the integration of the required bonding layers.

The feeding gap of the slots are provided power by a microstrip which runs to the integrated coax. At the other end of the microstrip a capacitive patch is introduced to compensate the influence
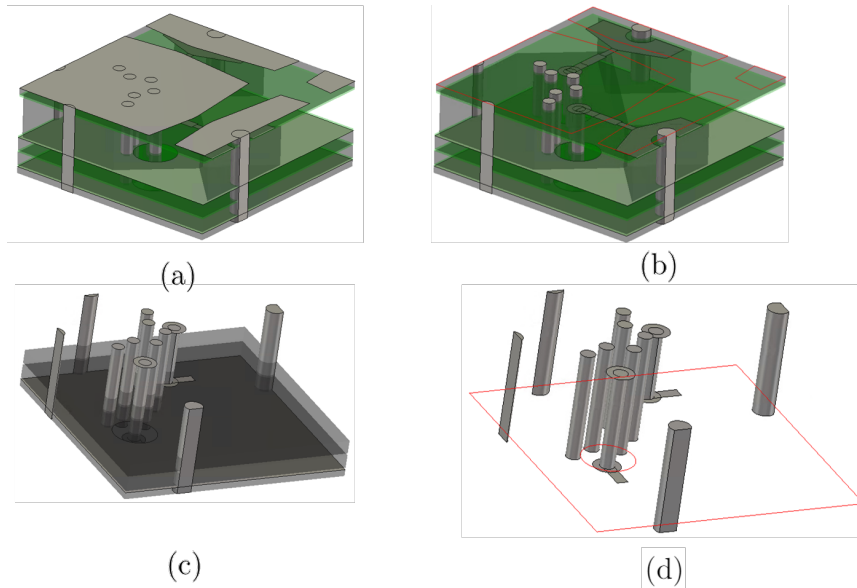
Figure 5.9: Feeding structure of the Unit cell: (a) top view onto the slot plane, (b) backing reflector cavity, (c) stripline layer and (d) microstrip layer.

of the backing reflector. The dielectric in the cavity is cut for about 50% to reduce the relative permittivity of the dielectric of 2.2 to an effective permittivity of around 1.7. To prevent a parallel plate wave mode to propagate in the cavity vias are placed which go through the entire stackup. the three shielding vias of the coax also protrude through the entire PCB stackup.

One of the orthogonal slots is fed by the stripline in the stripline layer. The stripline layer, Fig. 5.9(c), consists of two dielectric slabs with $\varepsilon_r = 2.2$ with the appropriate bonding layer placement. The other slot is fed by the mircostrip loacted at the bottom of the PCB, shown in Fig. 5.9(d), and feeds the slot trough the integrated coax.

5.4 Wire Medium Implementation

The host medium for the ADLs is still considered to bve vacuum. However to be able to manufacture the radome some support structures have to be placed, often made out of foam and thin dielectric slabs, as well as bonding layers. The implementation of these layers ia shown for other designs like [33]. When judging the manufacturability of the design, it first must be noted that vias can't be placed in a foam layer. To place vias, a dielectric layer is made and the vias are implemented later. In the structure of the previous section a dielectric layer is placed in-between the patches to facilitate that requirement. In this section the implementation of such dielectric layer is investigated. Secondly, the vias will be placed to obtain the required cross polarization reduction.
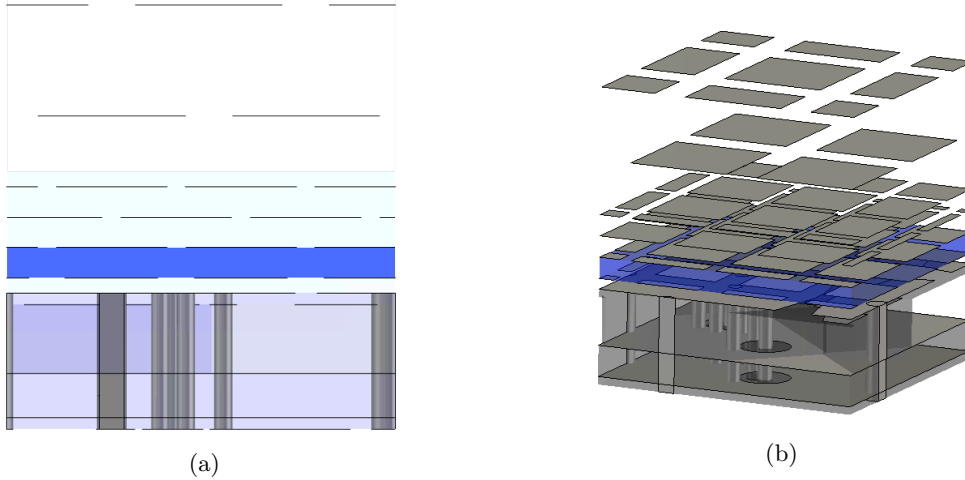
Figure 5.10: Optimized design with dielectric layer introduced in the ADL: (a) a Side view and (b) an three dimensional view of the unit cell with dielectric layer.

5.4.1 ADL with a Dielectric Layer

The first step in the implementation of the dielectric layer is the choice for the material. It is desired to obtain maximum control over the parameters. In addition, the host medium will increase the effect of the wire medium depending on the permittivity, as seen from section 4.2. In addition, a dielectric with a large permittivity may promote surface waves. Therefore, it is desired to use a dielectric with a low dielectric constant. A material which is strong enough and which has a relatively low permittivity compared to other materials is RT/duroid® 5880. This homogeneous isotropic dielectric has a permittivity of only 2.2. With this dielectric layer between the first and second layer the transformer is redesigned. Since the wire medium can only be placed in the dielectric the restriction on the shift for all other layers is loosened. The optimization provided a unit cell with six ADLs as seen in Fig. 5.10 with the parameters presented in section D.2.

Some differences can be observed with respect to the previous design. First, the number of ADLs in the entire structure is reduced from eight to six. This reduction partly caused by allowing a shift in-between the layers, except for the shift between layers 1 and 2. This shift increases the effective permittivity and thus lowers the required number of ADLs. Secondly, the dielectric, in contrast to vacuum as a host medium, already increases the effective permittivity of the section, thus decreasing the dependency on susceptance of the horizontal patches. In addition, the dielectric layer increases the effective permittivity in the slots of the ADL, which increases the susceptance of the layer. Lastly, the first and second section have different periodicity's. This difference can't yet be modeled by the analytical model in section 2.2, the parameters are obtained with full wave simulations. The parameters of the ADL are presented in section D.2.

The reflection coefficient of the unit cell is provided in Fig. 5.11(a). This coefficient shows that the wide angle impedance matching is working well with the dielectric. Similar as with the implementation of the wire medium, an improvement in the E-plane is observed with respect to to the case with out any dielectric or wires. That improvement is caused by the same effective parameter which is changed by the wire medium. The effective parameter $_z$ is increased in both

55
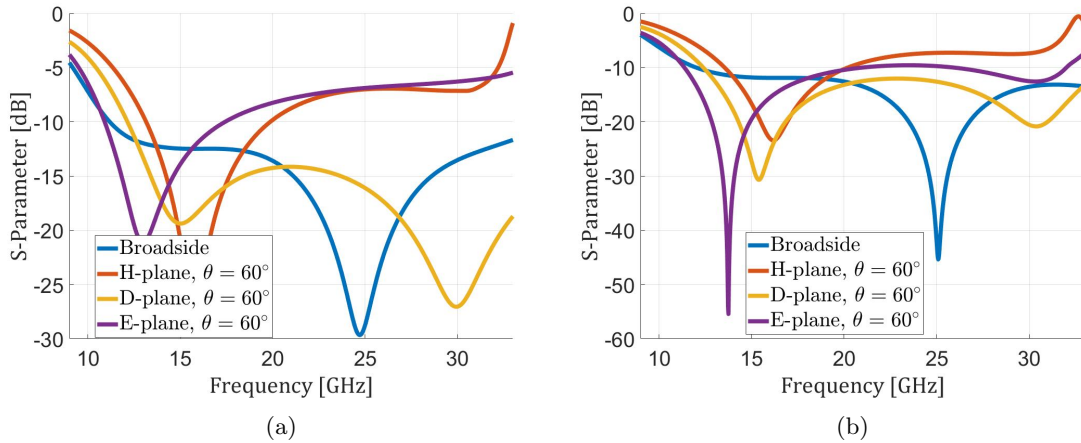
Figure 5.11: S_{11} of the connected slot array topped by the transformer (a) without and (b) with the dielectric slab.
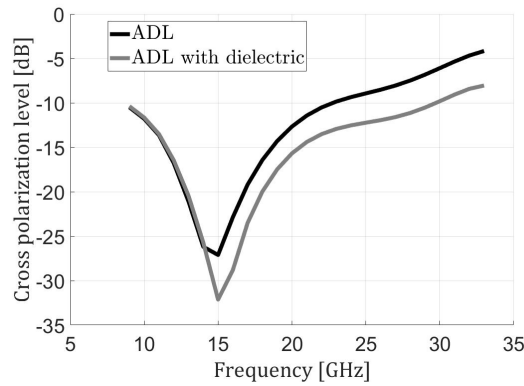
Figure 5.12: Cross polarization level of the designs with and without a dielectric layer of section 5.4.1.

cases, first due to the wire and now by the isotropic dielectric. Therefore, both a dielectric layer and the wire medium can be used to improve the E-plane matching.

Since the z-component of the permittivity is also increased by the dielectric layer, an improvement of the cross polarization is also observed, Fig. 5.12. This improvement doesn't yield a low enough level, thus the wire medium is implemented to increase the polarization purity even further.

5.4.2   Wire Medium in Dielectric Layer

As seen in section 4.2, the dielectric increases the effectiveness of the wire medium. Which was the cause for the design choice to reduce the two layer top-hat loaded wire medium to one layer. The structure is optimized using the commercial solver, that results in a denser medium. The
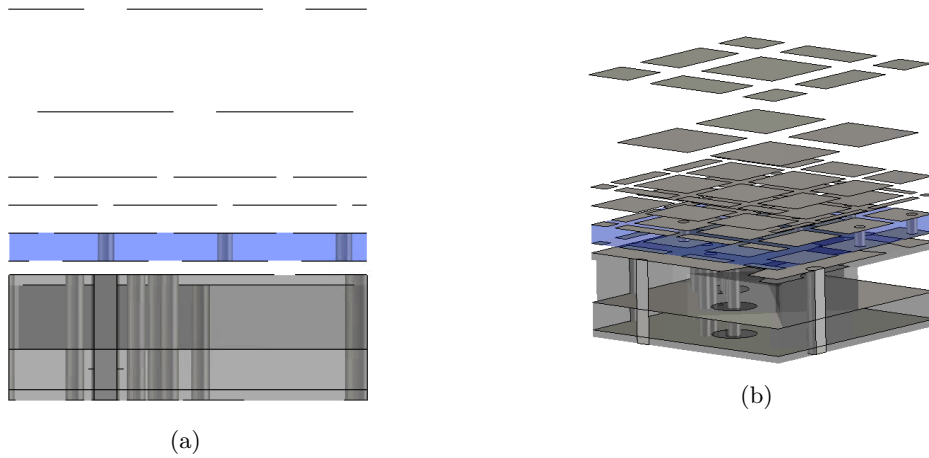
Figure 5.13: (a) Side view and (b) 3D view of the unit cell with dielectric and wire medium.
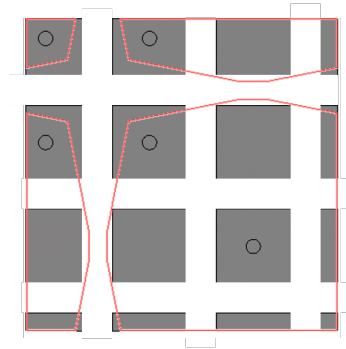
Figure 5.14: Top view off wire placement.

placement of the vias is optimized, as shown in Fig. 5.13. That results in a placements of the vias as schematically shown in figure Fig. 5.14. It is seen that the period of the wires is different than that of the horizontal ADL, only five out of the 9 patches per unit cell contain a via. The slot placement is also shown as a outline. The feeding gap of the slots are placed such that the E-plane of the slot is aliened with a row of patches and the H-plane is in between two patches. That alignment provides the best trade off between reflection coefficients and a reduction of the cross polarization.

The reflection coefficient of the unit cell is shown in Fig. 5.15(a). Comparing the E-plane matching to that with only the dielectric layer an improvement is again observed. In addition, to the resonance in the E-plane one also occurs in the H-plane. This H-plane resonance is observed at 32 GHz and is thus close to the operating frequency. This H-plane resonance is a wave propagating along the slot and was described in [5]. The density of the superstrate near the slot promotes this resonance, therefore the density of the first ADL is kept lower then the layers above.

Considering the cross polarization of the unit cell in the D-plane ($\theta = 60°$), an improvement is

57
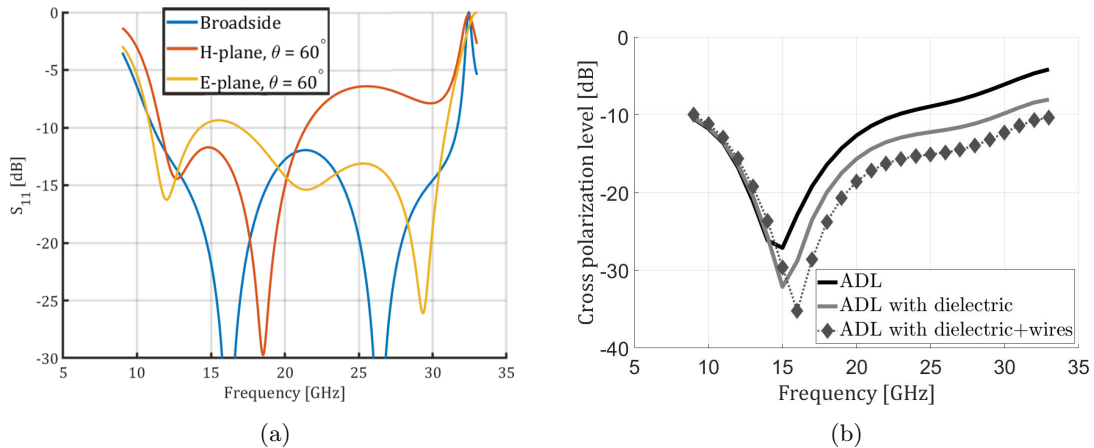
Figure 5.15: S_{11} of the connected slot array topped by an ADL with wire medium (a) without and (b) with the dielectric slab.

observed as well. This improvement is not as large as in the case with the implementation of the wire medium in free space. The amount of decrease is linked to the increase in the z-component of the permittivity. A larger increase may be obtained by adding an additional top-hat loaded wire medium. However, as seen in the E-plane resonance causes a mismatch which is present relatively close to the operating frequency. This mismatch is the TM0 surface mode supported by the structure, an increase of the permittivity to decrease the cross polarization further will eventually result in a shift of the surface wave to inside the operating band.

5.5 Design with Realistic Materials

The next step to fabrication of the ADL is the use of all support structures and manufacturing requirements such as minimal thicknesses and tolerances.

5.5.1 ADL with Realistic Materials

Only adding the one dielectric layer doesn't provide any manufacturability. To fabricate the structure the ADLs need a support structure consisting of a dielectric layer and preferable foam to space the layers. An example of the implementation of such support structure is found in [33]. The materials with their corresponding minimal thicknesses are presented in Tab. 5.1. For the realisation of the design the same materials will be used, in addition to the dielectric mentioned in the previous section.

The horizontal patches require a dielectric substrate to be printed on. The material used here is DuPont Pyralux AP with a thickness of 25 micron. In addition the patch size is limited, the patches have a minimal slot width of 0.1 mm. To fill the spaces in-between the ADLs an material which has a permittivity which is as close of the one of vacuum is desired as this has the least impact on the design. That requirement results in a foam, where air is trapped in a dielectric. The foam of choice is the ROCHACELL® 31HF foam, as it offers a low relative permittivity of 1.045. The
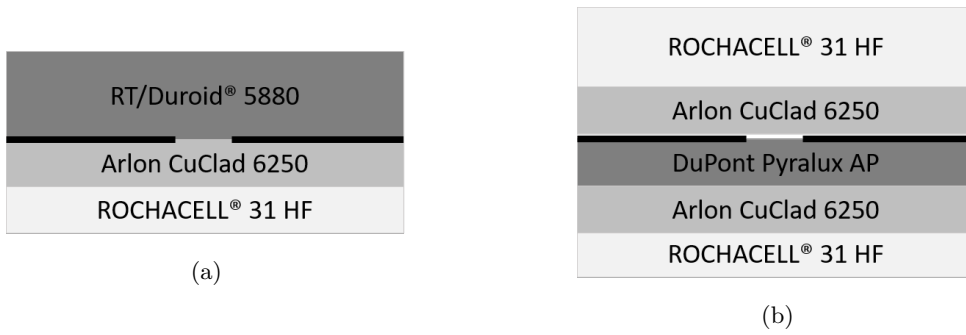
Figure 5.16: Stackup of bonding and support layers for (a) the first two layers and (b) the other layers.
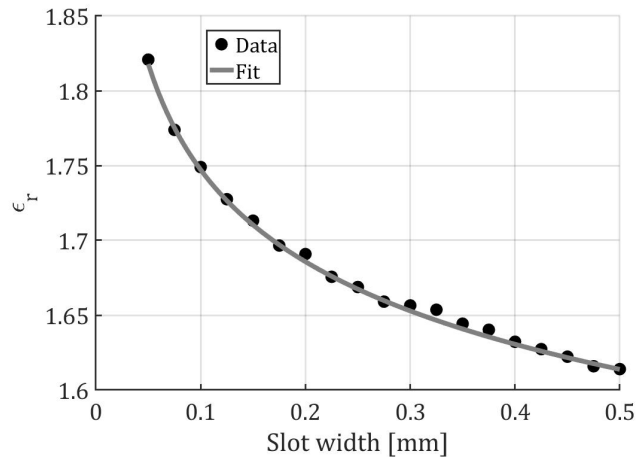
Figure 5.17: Fitting curve for effective permittivity in the slot of a ADL layer in a stakup shown in Fig. 5.16(a).

foam provides a support to space the ADLs with the required distance. The foam, dielectric and patches need to be bounded together. That bonding layer is is Arlon CuClad 6250 with a relative permittivity of 2.32.

As mentioned before, a dielectric near the ADL slot change the effective permittivity which

Table 5.1: Material list

Name	Dielectric constant	Minimal thickness (μm)
Arlon CuClad 6250	2.32	38
ROCHACELL® 31HF	1.045	500
DuPont Pyralux AP	3.4	25
RT/duroid® 5880	2.2	127

59
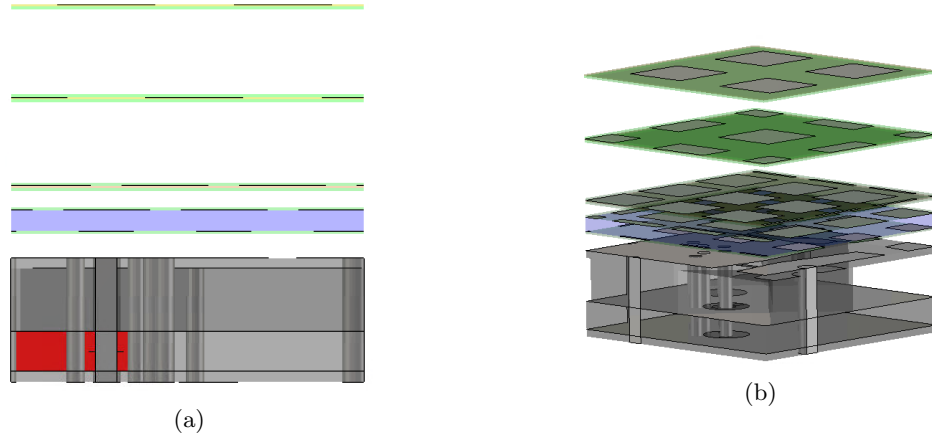
Figure 5.18: (a) Side view and (b) 3D view of the unit cell with dielectric layer and three bonding layers.

increase the supsceptance. This effective permittivity is not simply the average, since the thickness of the layer and the width of the slot both are influential. However, for infinite dielectrics above and below the ADL, the average is a good approximation. In case of the ADL shown in Fig. 5.16(b), a model for the effective permittivity is obtained in [5]. For the case in Fig. 5.16(a), which is for the top and bottom patch of the top-hat loaded wire medium, a model is obtained by the means of a fitting curve after simulations in CST. The effective permittivity is extracted from the S-parameters for two ports along the slot and the permittivity is modeled by Equation 5.1 with w in mm and where $a = 11.39$, $b = -0.005375$, $c = 0.01493$, $d = -0.5765$ and $e = -9.841$. This fitting curve on retrieved data from the solver at 31 GHz is presented in Fig. 5.17.

$$\varepsilon_{eff,fit} = aw^b + cw^d + e \tag{5.1}$$

5.5.2 Obtained Design with Real Dielectrics

The design of the radome is redone with the realistic materials and the required stackup of dielectric layers. The obtained design is presented in Fig. 5.18 with the parameters in section D.3. In contrast to the previous design the ADL structure contains 5 layers. The reduction in the number of layers is achieved by the increased effective permittivity in the slot gap of the ADL. Moreover, the dielectric layers also provide an increase in the effective permittivity of the slab thus smaller patches and less layers can be used to obtain the same effective permittivity.

To evaluating the performance of this design the reflection coefficients are simulated and presented in Fig. 5.19(a). The unit cell performs well at broadside with a reflection coefficient well below -10dB. It is seen that the two reflection coefficients for broadside, which depict the two orthogonal slots, differ significantly at 32 GHz. This deviation is caused by the feeding structure. One polarization is fed by a stripline and the other is fed by a microstrip. The reflection observed at broadside at 32 GHz is a resonance in the stripline layer. For the microstrip fed slot the feed is passed through the stripline layer with a partly closed integrated coax. Therefore, some of the power from the microstrip is also propagating in the stripline layer.
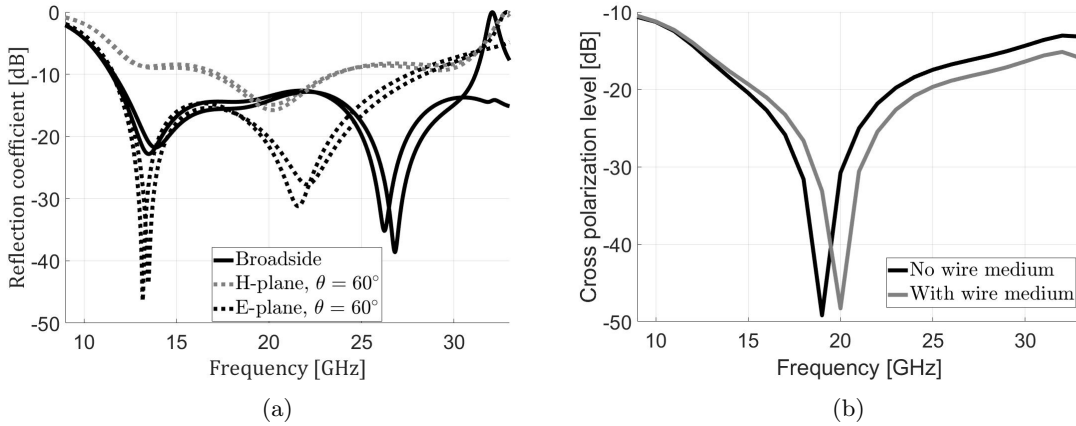
Figure 5.19: (a)Sparameters of the connected slot array with bonding layers and (b) The cross polarization level.

For the H-plane scanning the array is matched with a maximum of -6dB in the operating frequency band. The resonance for the wave propagating along the slot is also visible at 32.5 GHz. Additionally, the resonance of the TM_0 surface wave is observed in the E-plane around the same frequency. The surface wave was not a concern in the design with only the dielectric layer as it was at higher frequencies. The use of the dielectric bonding layers shifts that resonance to a lower frequency because the z-component of the effective permittivity is increased. That effect was also seen when implementing the wire medium.

The cross polarization level of the design only considering the dielectric layer in-between the first two patches reached a maximum of approximately -9dB. By introducing more dielectric it is expected that this level will be reduced even further. That decrease is seen in Fig. 5.19. That figure shows a maximum Xpol level of -13.6 dB in the operating frequency. In addition to the Xpol of the presented unit cell, the figure also contains the Xpol level of the unit cell with the top-hat loaded wire medium implemented. The vias connecting the two patches in the first section cause an additional decrease in the level of -2dB. That reduction is not as large as seen with the ADL in free space. It is expected that the cross polarization has an other component and is not solely a result of the difference in the refraction index. Moreover, the length of the wires are quite small and the patch size is decreased, therefore have only a limited effect.

The design performs well, however the layer heights don't account for the manufacturing constrains. The height of the first foam layer is only 0.3 mm, but the smallest foam layer of merely 0.2 mm is found between the second and third ADL. These layers can't be manufactured, additionally, if they could be manufactured the foam would be to fragile to handle. This leads to the next design where the layer heights are constrained to the height specified in Tab. 5.1.

5.5.3 Obtained Design with Real Dielectrics and Fabrication Limits

Form simulations a new design is obtained which adheres to all manufacturing constrains. The layer heights are large enough and all dimensions are spaced in order to accommodate the fabrication tolerances. Optimizing the array with these constrains a realistic unit cell is obtained, as shown in

(a)

(b)
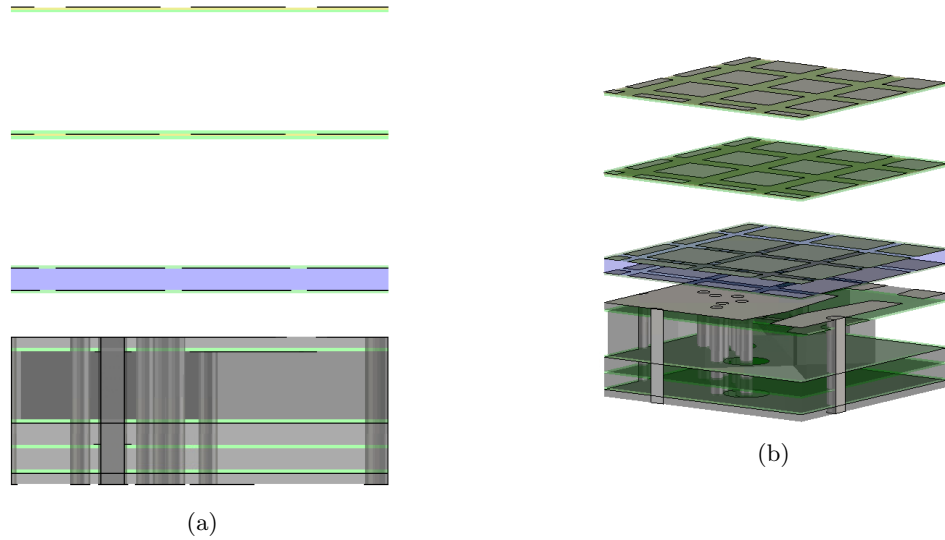
Figure 5.20: (a) Side view and (b) 3D view of the unit cell with dielectric layer and bonding layers.

Fig. 5.20 with the parameters presented in section D.4. The first section of the transform consists now of two layers with smaller gap widths as the setup with three layers didn't adhere to the constrains of the minimum layer height of the foam.

Again the unit cell is assessed by the reflection coefficient and the Xpol level, shown in figure Fig. 5.21. FRom the S-parameter it is seen that the array performs well at the Ku-frequency band, with a reflection coefficient below -10dB even while scanning. However, a degradation of the performance is seen at the Ka-band. This worse performance is limited to the broadside case, as the reflection is still lower then -6dB for scanning. For scanning in the E- and H-plane, the resonances are shifted to a lower frequency.

The fact that the decline is limited to broadside leads to the expectation that the cause of this worse performance is the resonance in the stripline layer which showed to occur only for broadside. The resonance is shifted by about 0.5 GHz downwards. This propagation in the stripline layer couples the two feeds because the orthogonal slot is fed by the other coax extending through this layer. That coupling is also likely to cause the high cross polarization of this design as the coupling would still be present while scanning, which is shown in Fig. 5.21(b). Since the coupling is the likely cause of the increased Xpol, the addition of the wire medium does not yield a reduction of the Xpol at the higher frequencies. However, a reduction of 4 dB is seen at 20 GHz, which indicated that the wire medium does reduce some of the cross polarization.

To investigate if this coupling is the cause of the high Xpol level the stripline and microstrip are removed. The port is therefore located at the beginning of the integrated coax inline with the ground plane. The reflection coefficients for broadside and scanning are provided in Fig. 5.22(a). The resonance at broadside is no longer present and the array is matched well in both the Ku- and Ka-frequency bands. The maximum reflection of -5.9 dB occurs at the lower limit of the Ku-band (28GHz) for the H-plane scanning to $\theta = 60°$. The difference between the desired reflection coefficient and the obtained results differ only slightly(0.1dB), therefore the unit cell is still considered
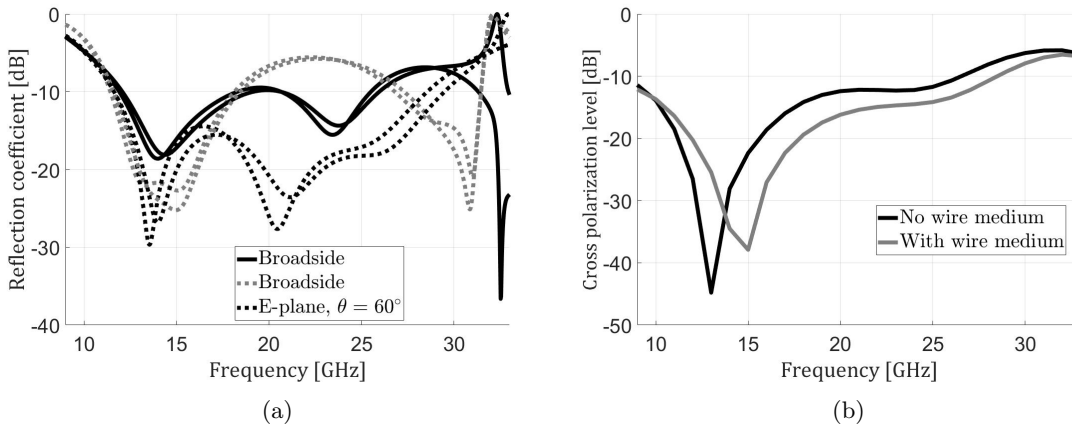
Figure 5.21: (a)S_{11} of the connected slot array without and (b) the cross polarization level with and without the wire medium.

to be matched well and while manufacturing some disturbance in the performance is expected.

Despite the removal of the the stripline layer, the Xpol level is still high as seen in Fig. 5.22(b). The removal of the stripline layer only improved the level by 1dB at 31 GHz. The wire medium might now be more effective in reducing the cross polarization.
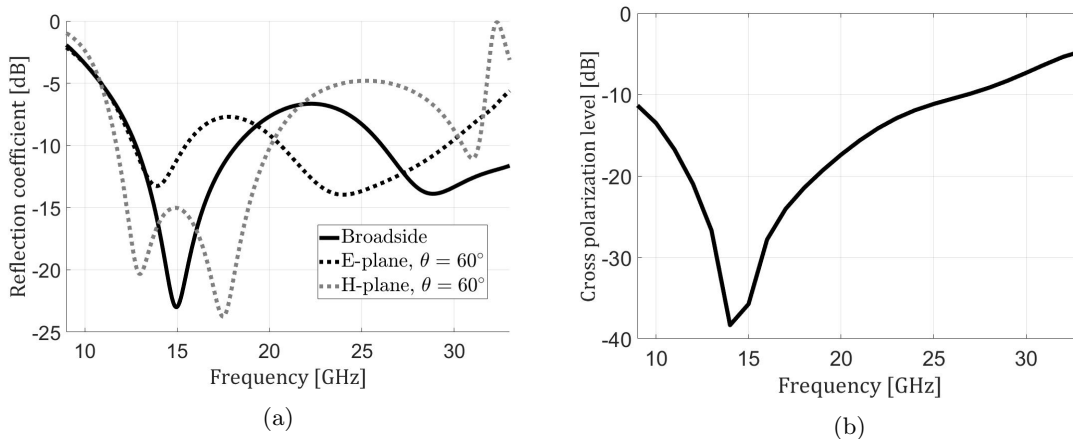
Figure 5.22: (a)S_{11} of the connected slot array fed at ground plane and (b) the cross polarization level.

5.6 Implementation of Wire Medium

In the last design the resonance in the stripline layer didn't seem to be the direct cause for the high cross polarization level (-6dB) at the upper frequency band. Here two cases are considered: the dual-polarized case and a basic single polarized case. The dual-polarized unit cell has the same backing reflector as shown in the feed in Fig. 5.9. However, it is shown that the cross polarization level is still to high. The cause is found in the design of the feed, therefore a single polarized slot with a backing reflector is considered to rigorously prove that the wire medium is effective in a design with all manufacturing constrains.

5.6.1 Dual-Polarized Unit Cell

To reduce the Xpol level of the pervious design the wire medium is implemented on all patches of the ADL, thus $p_{adl} = p_{wire}$ as shown in Fig. 5.23. To eliminate the uncertain factor of the stripline layer the slots are fed by a port at the integrated coax and the ground plane.

The cross polarization obtained with the design is shown in Fig. 5.24. The introduction of the wire medium leads to a slightly lower cross polarization. The effectiveness of the wire medium in this case is small. The cause of the small contribution can be attributed to two factors. Firstly, the height of the wire medium is small with only a wire length of 0.254 mm. In the designs considering free space this height was larger. However a similar decrease with the wire medium is seen with the dielectric slab as seen in subsection 5.5.2. A larger reduction migth be achieved with a larger wire height, however, in creasing that height also decreases the permittivity of the ADL which can only be limited be compensated by adjusting the width of the slot in the ADL. The second factor which increases the cross polarization compared with previous designs is the coupling between orthogonal slots. The S-parameters which describe the coupling are not presented here, but reach values in order of -10 to -12 dB at the higher frequency band. This coupling causes the orthogonal slot to radiate some power and add additional Xpol.

64

(a)   (b)
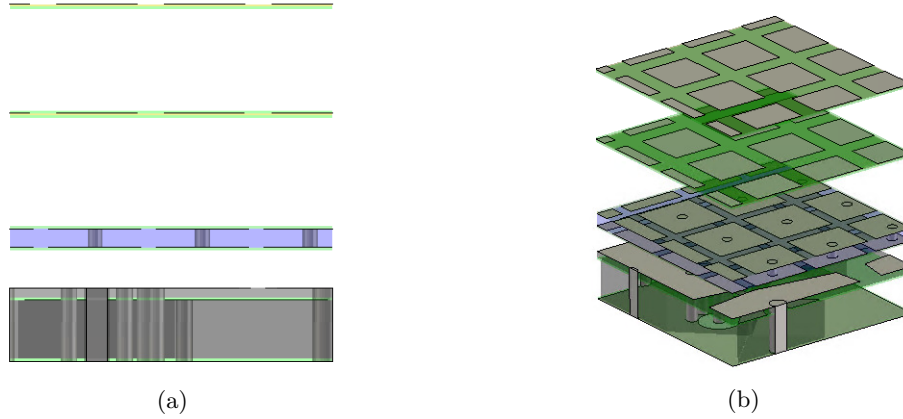
Figure 5.23: (a) Side view and (b) three dimensional view of the unit cell using the ADL with the dielectric layer housing the wire medium and the support materials all conforming to fabrication requirements.
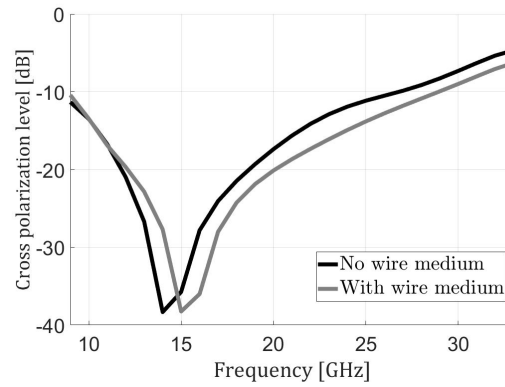
Figure 5.24: Xpol (D-plane $\theta = 60°$) of the unit cell using the ADL with the dielectric layer housing the wire medium and the support materials all conforming to fabrication requirements.

The polarization purity should be improved, but it seems that the cause in no longer only the difference in the refraction index. The cause for the high Xpol level is present in the backing reflector, because the unit cell is fed by at the ground plane. From Fig. 5.9 it is seen that the capacitive patch is close to a grounded via. The non-optimal placement of that via can cause additional coupling. The via is not centered in between two neighboring slots therefore the currents entering the via have different phases and might lead to some radiation in the cavity. In addition, the capacitive patch couples to this via, which in turns re-radiated the power into the cavity of the backing reflector. However, the via can't be simply removed as it would not block the parallel plate wave from propagating in the cavity.

65
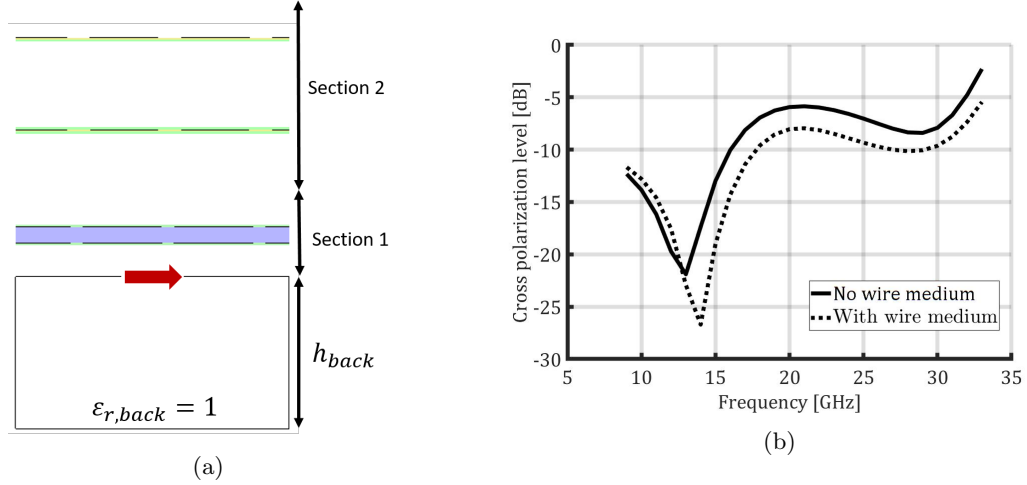
Figure 5.25: (a) Side view of the single polarized unit cell and (b) the corresponding cross polarization using the ADL with the dielectric layer and the support materials all conforming to fabrication requirements with and without wires.

5.6.2 single-polarized case

The complex backing reflector is removed and instead a backing reflector is placed at $h_{back} = \lambda_0/4$, as shown in Fig. 5.25(a). In addition, by reducing the array to a single polarized array the blocking vias are replaced by vertical walls walls again. This step back in the design shows a Xpol level consistent as seen in subsection 5.5.2, see Fig. 5.25(b).

It is clear that a large part of the cross polarization in the previous design was attributed to the coupling of the slots as the cross polarization is lower (3 dB) than in the dual polarized case. In addition, the wire medium results in a Xpol level of around -10 dB. The reduction is not as large as seen in free space designs. This limited reduction is a marker that the wire medium is effective in reducing the level but due to the fabrication constrains the effect is limited. In creasing the distance between the patches, thus increasing the wire length, may result in larger reduction of the Xpol level.

Chapter 6

Conclusion

6.1   Conclusion

The objective of this thesis was to introduce a new class of artificial dielectrics, with non-uniform or non-planar characteristics, with the goal of reducing the cross polarization generated by horizontal artificial dielectrics when used over ultra-wide bandwidths. For communication applications the polarization purity is an important requirement, especially when used in satellite communication.

This novel artificial dielectric considers not only horizontal patches, but also utilizes vias in the structure to support vertical currents. These vertical wires form a so called wire medium and gives an additional degree of freedom to control effective tensor permittivity of the artificial dielectric.

The advantage of this novel method is that the introduction of the wires does not alter the other effective parameters. In addition to increasing the polarization purity, the wire medium aids in the matching performance while scanning in the E-plane. The other effective parameters can be tuned by analytical model already published. The connected slot array and the artificial dielectrics were discussed in chapter 2. Analytical expressions were provided to design a connected slot array with horizontal artificial dielectrics.

In chapter 3 the cross polarization from connected dipole and connected slots were analyzed and compared to an ideal Wheeler current. The analysis showed that the connected slot and connected dipole behave differently because the space above and below the radiating element are coupled differently. In case of a connected slot the two spaces are decoupled because it represents an magnetic current radiating in the presence of an infinite perfectly conducting sheet. On the other hand, the upper and lower space are coupled in case of the connected dipoles, because they represent an electric current in free space. In addition, the use of substrates and superstrates were analyzed, where the coupling or decoupling was observed. Finally in chapter 3, the cross polarization of a dual polarized connected slot with artificial dielectric was analyzed and it was demonstrated that the cross polarization is caused by the difference in the refraction index for the transverse electric (TE) and the transverse magnetic (TM) wave.

The analysis of the wire medium to mitigate the cross polarization was described in chapter 4. A Method of Moments analysis was performed and a closed form expression was found for the higher order modes. In addition to the original wire medium, consisting of only wires, an integration of the wire medium with horizontal artificial dielectrics was introduced. The integration showed that the cross polarization was reduced by the presence of the vias.

Lastly in chapter 5, a design for a dual-polarized connected slot array operating in the Ku- and Ka-frequency bands was presented. The wire medium enhanced the polarization purity and assisted in the matching in the E-plane. However, a trade-off between the excitation of the TM_0 surface wave and the reduction of cross polarization is needed. The design was further developed with the use of real materials required for manufacturing. Moreover, the design did not only use real dielectrics, but also the manufacturing constrains, such as layer height, were taken into account. The use of the wire medium was shown to be effective in reducing the cross polarization. However, additional cause of cross polarization level in the last design is attributed to coupling between the orthogonal slots through the feeding structure. Moreover, the impact of the wire medium is also limited by the manufacturing constraint on the layer height. In creasing the length of the wire results in a increased polarization purity.

6.2   Future Work

The thesis showed a manufacturable method of reducing the cross polarization, however the method is still not complete. There are several possible future contributions to be made:

- For the design to be implemented with the feeding structure, it is required that the coupling is reduced. The high coupling is still a relatively difficult task as completely shielded coax are not feasible as they are too large and the via causing the coupling impacts the design of the corporate feeding network.

- Experimental validation of the design ought to be conducted. The design of the unit cell was part of a lager project on the design of wideband arrays for simultaneous Ka- and Ku-band satellite communication. With in the TeraHertz sensing group a prototype will be further developed and manufactured to validate the use of the wire medium for cross polarization reduction.

- The closed form expressions in chapter 4 are constrained and only consider a wire medium consisting of vertical wires. The design of future wideband arrays with artificial dielectrics is aided with a method of moments analysis of the top-hat loaded wire medium. The challenge with that analysis is that a model must be found, which describe the vertical current and the current on the patch which enters the vertical wire. Efforts have already been made to describe this interaction in [50].

- The current design is already wideband, however for some applications even larger bandwidths (multi-octave) are required. The effect of using the proposed method for large operational bandwidth still has to be researched.

Bibliography

[1] A. J. Van Katwijk, A. Neto, G. Toso, and D. Cavallo, "Design of wideband wide-scanning dual-polarized phased array covering simultaneously both the ku-and the ka-satcom bands," in *2020 14th European Conference on Antennas and Propagation (EuCAP)*. IEEE, 2020, pp. 1–3.

[2] R. Flamini, C. Mazzucco, R. Lombardi, C. Massagrande, F. Morgia, and A. Milani, "Millimeter-wave phased arrays for 5g: An industry view on current issues and challenges," in *IEEE Int. Symp. Phased Array System Technology*, 2019, pp. 1–2.

[3] G. Tavik, C. Hilterbrick, J. Evins, J. Alter, J. Crnkovich, J. de Graaf, W. Habicht, G. Hrin, S. Lessin, D. Wu, and S. Hagewood, "The advanced multifunction rf concept," *IEEE Transactions on Microwave Theory and Techniques*, vol. 53, no. 3, pp. 1009–1020, 2005.

[4] P. W. Moo and D. J. DiFilippo, "Overview of naval multifunction rf systems," in *2018 15th European Radar Conference (EuRAD)*, 2018, pp. 178–181.

[5] A. J. van Katwijk, "Design of a wideband wide-scan connected slot array antenna using artificial dielectrics," Master's thesis, 2019.

[6] P. Gibson, "The vivaldi aerial," in *1979 9th European Microwave Conference*, 1979, pp. 101–105.

[7] L. Lewis, M. Fassett, and J. Hunt, "A broadband stripline array element," in *1974 Antennas and Propagation Society International Symposium*, vol. 12, 1974, pp. 335–337.

[8] D. Schaubert, E. Kollberg, T. Korzeniowski, T. Thungren, J. Johansson, and K. Yngvesson, "Endfire tapered slot antennas on dielectric substrates," *IEEE Transactions on antennas and propagation*, vol. 33, no. 12, pp. 1392–1400, 1985.

[9] J. Shin and D. H. Schaubert, "A parameter study of stripline-fed vivaldi notch-antenna arrays," *IEEE Transactions on Antennas and Propagation*, vol. 47, no. 5, pp. 879–886, 1999.

[10] K. Trott, B. Cummings, R. Cavener, M. Deluca, J. Biondi, and T. Sikina, "Wideband phased array radiator," in *IEEE International Symposium on Phased Array Systems and Technology, 2003.*, 2003, pp. 383–386.

[11] H. Holter, "Dual-polarized broadband array antenna with bor-elements, mechanical design and measurements," *IEEE transactions on antennas and propagation*, vol. 55, no. 2, pp. 305–312, 2007.

[12] D. Schaubert, S. Kasturi, A. Boryssenko, and W. Elsallal, "Vivaldi antenna arrays for wide bandwidth and electronic scanning," in *The Second European Conference on Antennas and Propagation, EuCAP 2007*, 2007, pp. 1–6.

[13] R. W. Kindt and W. R. Pickles, "Ultrawideband all-metal flared-notch array radiator," *IEEE Transactions on Antennas and Propagation*, vol. 58, no. 11, pp. 3568–3575, 2010.

[14] N. Jastram and D. S. Filipovic, "Pcb-based prototyping of 3-d micromachined rf subsystems," *IEEE Transactions on Antennas and Propagation*, vol. 62, no. 1, pp. 420–429, 2014.

[15] V. Sanchez, T. Spence, and M. Cooley, "Broadband additively manufactured array antennas (bamaas) and planar-fed stepped notch (pfsn) arrays," in *Antenna Applications Symposium*, 2015, pp. 520–532.

[16] J. Lee, S. Livingston, and R. Koenig, "A low-profile wide-band (5: 1) dual-pol array," *IEEE Antennas and Wireless Propagation Letters*, vol. 2, pp. 46–49, 2003.

[17] Y.-S. Kim and K. Yngvesson, "Characterization of tapered slot antenna feeds and feed arrays," *IEEE Transactions on Antennas and Propagation*, vol. 38, no. 10, pp. 1559–1564, 1990.

[18] D. Schaubert, J. Shin, and G. Wunsch, "Characteristics of single-polarized phased array of tapered slot antennas," in *Proceedings of International Symposium on Phased Array Systems and Technology*, 1996, pp. 102–106.

[19] D. McGrath, N. Schuneman, T. Shively, and J. Irion, "Polarization properties of scanning arrays," in *IEEE International Symposium on Phased Array Systems and Technology, 2003.*, 2003, pp. 295–299.

[20] B. Veidt, G. J. Hovey, T. Burgess, R. J. Smegal, R. Messing, A. G. Willis, A. D. Gray, and P. E. Dewdney, "Demonstration of a dual-polarized phased-array feed," *IEEE Transactions on Antennas and Propagation*, vol. 59, no. 6, pp. 2047–2057, 2011.

[21] J. T. Logan, R. W. Kindt, and M. N. Vouvakis, "Low cross-polarization vivaldi arrays," *IEEE Transactions on Antennas and Propagation*, vol. 66, no. 4, pp. 1827–1837, 2018.

[22] H. Wheeler, "Simple relations derived fom a phased-array antenna made of an infinite current sheet," *IEEE Transactions on Antennas and Propagation*, vol. 13, no. 4, pp. 506–514, 1965.

[23] D. McGrath and C. Baum, "Scanning and impedance properties of tem horn arrays for transient radiation," *IEEE Transactions on Antennas and Propagation*, vol. 47, no. 3, pp. 469–473, 1999.

[24] B. A. Munk, *Finite antenna arrays and FSS*.   John Wiley & Sons, 2003.

[25] Hansen, "Linear connected arrays [coupled dipole arrays]," *IEEE Antennas and Wireless Propagation Letters*, vol. 3, pp. 154–156, 2004.

[26] A. Neto and J. Lee, ""infinite bandwidth" long slot array antenna," *IEEE Antennas and Wireless Propagation Letters*, vol. 4, pp. 75–78, 2005.

[27] J. P. Doane, K. Sertel, and J. L. Volakis, "A wideband, wide scanning tightly coupled dipole array with integrated balun (tcda-ib)," *IEEE Transactions on Antennas and Propagation*, vol. 61, no. 9, pp. 4538–4548, 2013.

[28] W. F. Moulder, K. Sertel, and J. L. Volakis, "Ultrawideband superstrate-enhanced substrate-loaded array with integrated feed," *IEEE Transactions on Antennas and Propagation*, vol. 61, no. 11, pp. 5802–5807, 2013.

[29] M. H. Novak and J. L. Volakis, "Ultrawideband antennas for multiband satellite communications at uhf–ku frequencies," *IEEE Transactions on Antennas and Propagation*, vol. 63, no. 4, pp. 1334–1341, 2015.

[30] S. S. Holland, D. H. Schaubert, and M. N. Vouvakis, "A 7-21 ghz dual-polarized planar ultrawideband modular antenna (puma) array," *IEEE Transactions on Antennas and Propagation*, vol. 60, no. 10, pp. 4589–4600, 2012.

[31] J. A. Kasemodel, C.-C. Chen, and J. L. Volakis, "Wideband planar array with integrated feed and matching network for wide-angle scanning," *IEEE Transactions on Antennas and Propagation*, vol. 61, no. 9, pp. 4528–4537, 2013.

[32] W. H. Syed, D. Cavallo, H. T. Shivamurthy, and A. Neto, "Wideband, wide-scan planar array of connected slots loaded with artificial dielectric superstrates," *IEEE Transactions on Antennas and Propagation*, vol. 64, no. 2, pp. 543–553, 2015.

[33] D. Cavallo, W. H. Syed, and A. Neto, "Connected-slot array with artificial dielectrics: A 6 to 15 ghz dual-pol wide-scan prototype," *IEEE Transactions on Antennas and Propagation*, vol. 66, no. 6, pp. 3201–3206, 2018.

[34] D. Cavallo, "Connected array antennas: Analysis and design," Ph.D. dissertation, Electrical Engineering, 2011.

[35] A. Neto and S. Maci, "Input impedance of slots printed between two dielectric media and fed by a small-gap," *IEEE Antennas Wireless Propag. Lett*, vol. 3, no. 1, pp. 113–116, 2004.

[36] A. Neto, D. Cavallo, G. Gerini, and G. Toso, "Scanning performances of wideband connected arrays in the presence of a backing reflector," *IEEE Transactions on Antennas and Propagation*, vol. 57, no. 10, pp. 3092–3102, 2009.

[37] A. Neto and J. J. Lee, "Ultrawide-band properties of long slot arrays," *IEEE Transactions on Antennas and Propagation*, vol. 54, no. 2, pp. 534–543, Feb 2006.

[38] D. Cavallo, W. H. Syed, and A. Neto, "Closed-form analysis of artificial dielectric layers—part i: Properties of a single layer under plane-wave incidence," *IEEE Transactions on Antennas and Propagation*, vol. 62, no. 12, pp. 6256–6264, Dec 2014.

[39] D. Cavallo, W. H. Syed, and A. Neto, "Closed-form analysis of artificial dielectric layers—part ii: Extension to multiple layers and arbitrary illumination," *IEEE Transactions on Antennas and Propagation*, vol. 62, no. 12, pp. 6265–6273, Dec 2014.

[40] D. Cavallo and C. Felita, "Analytical formulas for artificial dielectrics with nonaligned layers," *IEEE Transactions on Antennas and Propagation*, vol. 65, no. 10, pp. 5303–5311, Oct 2017.

[41] D. Cavallo and R. M. van Schelven, "Closed-form analysis of artificial dielectric layers with non-periodic characteristics," in *2019 13th European Conference on Antennas and Propagation (EuCAP)*, March 2019, pp. 1–5.

[42] D. Cohen and R. Shavit, "Bi-anisotropic metamaterials effective constitutive parameters extraction using oblique incidence s-parameters method," *IEEE Transactions on Antennas and Propagation*, vol. 63, no. 5, pp. 2071–2078, May 2015.

[43] A. J. Van Katwijk and D. Cavallo, "Analysis and design of connected slot arrays with artificial dielectrics," in *2019 IEEE International Symposium on Phased Array System & Technology (PAST)*. IEEE, 2019, pp. 1–5.

[44] D. A. Frickey, "Conversions between s, z, y, h, abcd, and t parameters which are valid for complex source and load impedances," *IEEE Transactions on microwave theory and techniques*, vol. 42, no. 2, pp. 205–211, 1994.

[45] A. Ludwig, "The definition of cross polarization," *IEEE Transactions on Antennas and Propagation*, vol. 21, no. 1, pp. 116–119, 1973.

[46] H. Wheeler, "Simple relations derived fom a phased-array antenna made of an infinite current sheet," *IEEE Transactions on Antennas and Propagation*, vol. 13, no. 4, pp. 506–514, July 1965.

[47] W. E. Kock, "Metallic delay lenses," *Bell System Technical Journal*, vol. 27, no. 1, pp. 58–82, 1948.

[48] R. E. Collin, *Field theory of guided waves*. John Wiley & Sons, 1990, vol. 5.

[49] C. Butler, "General solutions of the narrow strip (and slot) integral equations," *IEEE Transactions on Antennas and Propagation*, vol. 33, no. 10, pp. 1085–1090, 1985.

[50] H. Thippur Shivamurthy, "On the design and analysis of micro-metric resolution arrays in integrated technology for near-field dielectric spectroscopy," Ph.D. dissertation, Electrical Engineering, 2020.

Appendix A

Homogenization with Reflection and Transmission coefficients

With the homogenization procedure the parameters of an equivalent permittivity and permeability for a structure are determent. Those parameters are then used to simulate a homogeneous dielectric material with those parameters which behaves the same as the structure which is investigated.

The effective permittivity of an arbitrary structure with a thickness of d can be determined from its reflection and transmission coefficients [42]. As often is done, the incident wave is split into a TE and TM component, because the structure behaves different for plane waves of those different polarization's. In addition, the behavior varies also with the incident angle. Using these relations of the polarization and the incident angle the S-parameters are determent for the TE- and TM-polarization, for incident plane waves from broadside ($\theta_0 = 0°$) and a certain angle θ_1.

$$\eta_{TE} = \pm \sqrt{\frac{\left(1 + S_{11}^{TE}\right)^2 - \left(S_{21}^{TE}\right)^2}{\left(1 - S_{11}^{TE}\right)^2 - \left(S_{21}^{TE}\right)^2}} \sec \theta$$

$$\eta_{TM} = \pm \sqrt{\frac{\left(1 + S_{11}^{TM}\right)^2 - \left(S_{21}^{TM}\right)^2}{\left(1 - S_{11}^{TM}\right)^2 - \left(S_{21}^{TM}\right)^2}} \cos \theta$$

$$n_{TE} = \sqrt{\left(\frac{\log |\zeta^{TE}| + j\left[\angle\left(\zeta^{TE}\right) + 2\pi m\right]}{-jk_0 d}\right)^2 + \sin^2 \theta}$$

$$n_{TM} = \sqrt{\left(\frac{\log |\zeta^{TM}| + j\left[\angle\left(\zeta^{TM}\right) + 2\pi \bar{m}\right]}{-jk_0 d}\right)^2 + \sin^2 \theta,}$$

In the last two equations m and $\bar{m}$ are integers and as mentioned before, d is the thickness of the structure. The parameters ζ are described as:
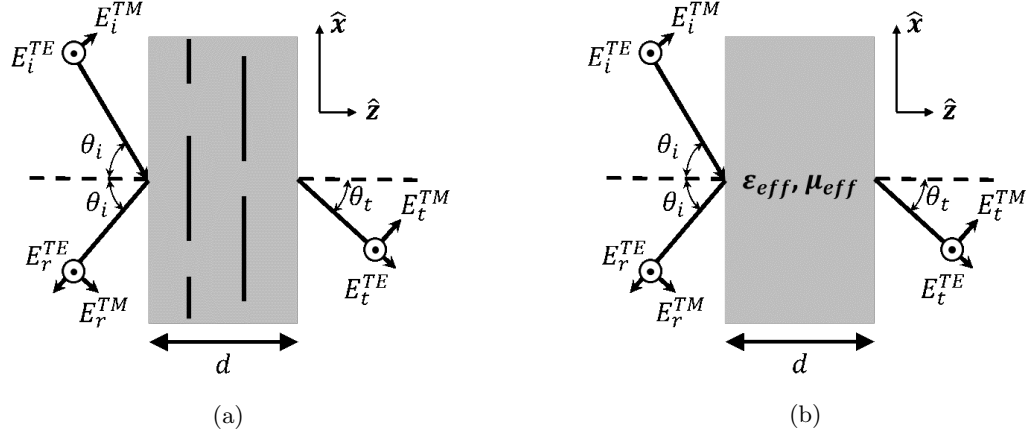
Figure A.1: Example of (a) an ADL slab and (b) its homogeneous equivalent dielectric.

$$\zeta^{TE} = \frac{S_{21}^{TE}}{1 - S_{11}^{TE} \left(\eta^{TE} \cos\theta - 1\right) / \left(\eta^{TE} \cos\theta + 1\right)}$$

$$\zeta^{TM} = \frac{S_{21}^{TM}}{1 - S_{11}^{TM} \left(\eta^{TM} / \cos\theta - 1\right) / \left(\eta^{TM} / \cos\theta + 1\right)}.$$

With the values for the refraction index, n_{TE} and n_{TM}, along side the normalized wave impedances η_{TM} and η_{TE} the the effective permittivity and permeability for the xy-plane are extracted by:

$$\varepsilon_x = \left. \frac{n_{TE}}{\eta_{TE}} \right|_{\theta=0},$$

$$\varepsilon_y = \left. \frac{n_{TM}}{\eta_{TM}} \right|_{\theta=0},$$

$$\mu_x = \left. (n_{TE}\eta_{TE}) \right|_{\theta=0},$$

$$\mu_y = \left. (n_{TM}\eta_{TM}) \right|_{\theta=0} + \frac{\xi_0^2}{\varepsilon_z}.$$

In the previous extraction the term ξ_0 is the couplings constant, but for structures such as an ADL slab or a dielectric slab it can be assumed there is no coupling between the TE and TM wave. Therefore it can be assumed that $\xi_0 = 0$. However, the parameters can't be evaluated yet, because m and $\bar{m}$ are still unknown. These terms indicate different branches for determining two sets of

74

longitudinal parameters, for both ε_z and μ_z given by

$$\varepsilon_z^{(1)} = \varepsilon_x \frac{\sin^2 \theta}{\sin^2 \theta - (n^{TM})^2 + (n^{TM}|_{\theta=0})^2}$$

$$\varepsilon_z^{(2)} = \frac{\sin^2 \theta}{(n^{TM}\eta^{TM})|_{\theta=0} - \varepsilon_x/(\eta^{TM})^2}$$

$$\mu_z^{(1)} = \frac{\sin^2 \theta}{(n^{TE}/\eta^{TE})|_{\theta=0} - \mu_x/(\eta^{TE})^2}$$

$$\mu_z^{(2)} = \mu_x \frac{\sin^2 \theta}{\sin^2 \theta - (n^{TE})^2 + (n^{TE}|_{\theta=0})^2}.$$

By equating the two sets of parameters the correct value for m and $\bar{m}$ are found.

$$\varepsilon_z^{(1)} = \varepsilon_z^{(2)}$$

$$\mu_z^{(1)} = \mu_z^{(2)}.$$

Appendix B

Solving the Integral Equation for the Wire Medium

In this appendix the integral equation from section 4.1.3 is calculated.

$$\iiint_V \sum_{n_x=-\infty}^{\infty} \sum_{n_y=-\infty}^{\infty} I_0 b\left(x' - n_x d, y' - n_y d, z'\right) g(\vec{r}, \vec{r'}) e^{-jk_{x0}n_x d} e^{-jk_{y0}n_y d} d\vec{r'} = -\vec{e}_i(\vec{r})$$

The spatial Green's function $g(\vec{r}, \vec{r'})$ can be written as the inverse Fourier transform of the spectral Green's function $G(k_x, k_y, k_z)$.

$$g(\vec{r}, \vec{r'}) = \frac{1}{(2\pi)^3} \iiint_{-\infty}^{\infty} G(k_x, k_y, k_z) e^{-jk_x(x-x')} e^{-jk_y(y-y')} e^{-jk_z(z-z')} dk_x dk_y dk_z$$

The integral then becomes:

$$\int_{n_x d-a/2}^{n_x d+a/2} \int_{n_x d-a/2}^{n_x d+a/2} \int_{-h/2}^{h/2} \sum_{n_x=-\infty}^{\infty} \sum_{n_y=-\infty}^{\infty} I_0 b\left(x' - n_x d, y' - n_y d, z'\right)$$

$$\left[\frac{1}{(2\pi)^3} \iiint_{-\infty}^{\infty} G(k_x, k_y, k_z) e^{-jk_x(x-x')} e^{-jk_y(y-y')} e^{-jk_z(z-z')} dk_x dk_y dk_z \right] \tag{B.1}$$

$$e^{-jk_{x0}n_x d} e^{-jk_{y0}n_y d} dx' dy' dz' = -e_i(r)$$

Performing change of variables $x' = x' - n_x d$ and $y' = y' - n_y d$:

$$\frac{1}{(2\pi)^3} \int_{-a/2}^{a/2} \int_{-a/2}^{a/2} \int_{-h/2}^{h/2} \sum_{n_x=-\infty}^{\infty} \sum_{n_y=-\infty}^{\infty} I_0 b\left(x', y', z'\right)$$

$$\left[\iiint_{-\infty}^{\infty} G(k_x, k_y, k_z) e^{-jk_x(x-x'-n_x d)} e^{-jk_y(y-y'-n_y d)} e^{-jk_z(z-z')} \right] \tag{B.2}$$

$$e^{-jk_{x0}n_x d} e^{-jk_{y0}n_y d} dx' dy' dz' dk_x dk_y dk_z = -e_i(r)$$

$$\frac{1}{(2\pi)^3} \int_{-a/2}^{a/2} \int_{-a/2}^{a/2} \int_{-h/2}^{h/2} \sum_{n_x=-\infty}^{\infty} \sum_{n_y=-\infty}^{\infty} I_0 b\left(x', y', z'\right)$$

$$\iiint_{-\infty}^{\infty} G(k_x, k_y, k_z) e^{-jk_x(x-x')}$$

(B.3)

$$e^{-jk_y(y-y')} e^{-jk_z(z-z')} e^{j(k_x-k_{x0})n_x d} e^{j(k_y-k_{y0})n_y d} dx' dy' dz' dk_x dk_y dk_z = -\vec{e}_i(\vec{r})$$

Rearranging the terms the Fourier transform of the basis function can be observed:

$$\frac{I_0}{(2\pi)^3} \left[\int_{-a/2}^{a/2} \int_{-a/2}^{a/2} \int_{-h/2}^{h/2} b\left(x', y', z'\right) e^{-jk_x x'} e^{-jk_y y'} e^{-jk_z z'} dx' dy' dz' \right]$$

$$\iiint_{-\infty}^{\infty} \sum_{n_x=-\infty}^{\infty} \sum_{n_y=-\infty}^{\infty} G(k_x, k_y, k_z) e^{-jk_x x} e^{-jk_y y} e^{-jk_z z}$$

(B.4)

$$e^{j(k_x-k_{x0})n_x d} e^{j(k_y-k_{y0})n_y d} dk_x dk_y dk_z = -\vec{e}_i(\vec{r})$$

It follows that:

$$\frac{I_0}{(2\pi)^3} B(k_x, k_y, k_z) \iiint_{-\infty}^{\infty} \sum_{n_x=-\infty}^{\infty} \sum_{n_y=-\infty}^{\infty} G(k_x, k_y, k_z)$$

(B.5)

$$e^{-jk_x x} e^{-jk_y y} e^{-jk_z z} e^{j(k_x-k_{x0})n_x d} e^{j(k_y-k_{y0})n_y d} dk_x dk_y dk_z = -\vec{e}_i(\vec{r})$$

Using the Poisson formula, where $k_{xm} = k_{x0} - \frac{2\pi m_x}{d}$ and $k_{ym} = k_{y0} - \frac{2\pi m_y}{d}$, along with the observation that B only has a z-component.

$$\sum_{n_x=-\infty}^{\infty} e^{j(k_x-k_{x0})n_x d_x} = \frac{2\pi}{d_x} \sum_{m_x=-\infty}^{\infty} \delta\left(k_x - k_{xm}\right)$$

$$\sum_{n_y=-\infty}^{\infty} e^{j(k_y-k_{y0})n_y d_y} = \frac{2\pi}{d_y} \sum_{m_y=-\infty}^{\infty} \delta\left(k_y - k_{ym}\right)$$

$$\frac{I_0}{(2\pi)^3} \int_{-\infty}^{\infty} B(k_x, k_y, k_z) G_{zz}(k_x, k_y, k_z)$$

$$\frac{2\pi}{d_x} \sum_{m_x=-\infty}^{\infty} \delta\left(k_x - k_{xm}\right) \frac{2\pi}{d_y} \sum_{m_y=-\infty}^{\infty} \delta\left(k_y - k_{ym}\right)$$

(B.6)

$$e^{-jk_x x} e^{-jk_y y} e^{-jk_z z} e^{j(k_x-k_{x0})n_x d} e^{j(k_y-k_{y0})n_y d} dk_x dk_y dk_z = -\vec{e}_i(\vec{r})$$

Where

$$G(k_x, k_y, k_z) = \frac{j\zeta_0}{k_0} \begin{bmatrix} k_0^2 - k_x^2 & -k_x k_y & -k_x k_z \\ -k_y k_x & k_0^2 - k_y^2 & -k_y k_z \\ -k_z k_x & -k_z k_y & k_0^2 - k_z^2 \end{bmatrix} \frac{1}{k_0^2 - k_x^2 - k_y^2 - k_z^2}$$

(B.7)

$$\frac{I_0}{(2\pi)^3} \int_{-\infty}^{\infty} B(k_x, k_y, k_z) G_{zz}(k_x, k_y, k_z)$$

$$\frac{2\pi}{d_x} \sum_{m_x=-\infty}^{\infty} \delta\left(k_x - k_{xm}\right) \frac{2\pi}{d_y} \sum_{m_y=-\infty}^{\infty} \delta\left(k_y - k_{ym}\right) \tag{B.8}$$

$$e^{-jk_x x} e^{-jk_y y} e^{-jk_z z} dk_x dk_y dk_z = -\vec{e}_i(\vec{r})$$

$$\frac{I_0}{2\pi d^2} \int_{-\infty}^{\infty} \sum_{m_x=-\infty}^{\infty} \sum_{m_y=-\infty}^{\infty} B(k_{xm}, k_{ym}, k_{zm}) G_{zz}(k_{xm}, k_{ym}, k_{zm})$$

$$e^{-jk_{xm} x} e^{-jk_{ym} y} e^{-jk_{zm} z} dk_z = -\vec{e}_i(\vec{r}) \tag{B.9}$$

Appendix C

Closed Form Expression of the Integral for the Self Impedance of the Wire Medium

The self-impedance for the inverse edge-singular basis function involves the calculation of integrals as the following:

$$\int_{-\infty}^{\infty} B(k_z)B(-k_z)G_{zz}(k_{xm}, k_{ym}, k_z)dk_z$$

With the Fourier transform of the basis function:

$$B(k_x, k_y, k_z) = \frac{J_1\left(\frac{k_z h}{2}\right)}{k_z h} 2a \left(\cos\left(\frac{k_x a}{2}\right)\operatorname{sinc}\left(\frac{k_y a}{2}\right) + \cos\left(\frac{k_y a}{2}\right)\operatorname{sinc}\left(\frac{k_x a}{2}\right) \right) \hat{z}$$

Splitting the basis function into a component dependent of k_z

$$\frac{J_1\left(\frac{k_z h}{2}\right)}{k_z h}$$

and a component which is constant

$$2a \left(\cos\left(\frac{k_x a}{2}\right)\operatorname{sinc}\left(\frac{k_y a}{2}\right) + \cos\left(\frac{k_y a}{2}\right)\operatorname{sinc}\left(\frac{k_x a}{2}\right) \right).$$

The integral is performed only with the dependency on k_z, therefore:

$$B(k_z)B(-k_z) = B(k_z)^2 = \left(\frac{J_1\left(\frac{k_z h}{2}\right)}{k_z h} \right)^2$$

With the z-component of the Spectral Green's function (G_{zz}) the integral which needs to be solved is:

$$j\frac{4\zeta}{k_0 h^2} \int_{-\infty}^{\infty} \frac{J_1^2\left(\frac{k_z h}{2}\right)}{k_z^2} \frac{k_0^2 - k_z^2}{k_0^2 - k_{xm}^2 - k_{ym}^2 - k_{zm}^2} dk_z$$

79

The integral is split into two parts:

$$j\frac{4\zeta}{k_0h^2}\int_{-\infty}^{\infty}\frac{J_1^2\left(\frac{k_zh}{2}\right)}{k_z^2}\frac{k_0^2}{k_0^2-k_{xm}^2-k_{ym}^2-k_{zm}^2}dk_z - j\frac{4\zeta}{k_0h^2}\int_{-\infty}^{\infty}\frac{J_1^2\left(\frac{k_zh}{2}\right)}{k_0^2-k_{xm}^2-k_{ym}^2-k_{zm}^2}dk_z$$

The first integral

$$\int_{-\infty}^{\infty}\frac{J_1^2\left(\frac{k_zh}{2}\right)}{k_z^2}\frac{k_0^2}{k_0^2-k_{xm}^2-k_{ym}^2-k_{zm}^2}dk_z$$

With a change of variable:

$$\frac{k_zh}{2}=x, \frac{dx}{dk_z}=h/2, dk_z=\frac{2}{h}dx$$

Which results in:

$$\int_{-\infty}^{\infty}\frac{J_1^2\left(x\right)}{\left(\frac{4}{h^2}x^2\right)\left(k_0^2-k_{xm}^2-k_{ym}^2-\frac{4}{h^2}x^2\right)}\frac{2}{h}dx$$

$$\frac{2}{h}\int_{-\infty}^{\infty}\frac{J_1^2\left(x\right)}{\left(\frac{-16}{h^4}x^2\right)\left(x^2+\frac{h^2}{4}\left(k_{xm}^2+k_{ym}^2-k_0^2\right)\right)}dx$$

Introducing a new variable $K=\frac{h^2}{4}\left(k_{xm}^2+k_{ym}^2-k_0^2\right)$ an expression for the integral is found:

$$-\frac{h^3}{8}\int_{-\infty}^{\infty}\frac{J_1^2(x)}{(x^2(x^2+K^2))}dx = -\frac{h^3}{8}\left[\pi\left(\frac{1}{K^2}\right)^{3/2}I_1(K)^2-\frac{64\,_2F_3(1,2;3/2,5/2,7/2;K^2)}{45\pi}\right]$$

This integral is only valid for $\Re(K^2)>0 \vee K^2 \notin \mathbb{R}$, which means it is valid for all m_x and m_y except for the fundamental mode($m_x=m_y=0$). That mode still has to be evaluated numerically. In the integral $J_1(x)$ is the first Bessel function of the first kind, I_1 is the modified Bessel function of the first kind and $_2F_3$ is the generalized hyper geometric function with two sets of parameters with the first set containing two values and the second set contains three parameters.

The second integral

$$\int_{-\infty}^{\infty}\frac{J_1^2\left(\frac{k_zh}{2}\right)}{k_0^2-k_{xm}^2-k_{ym}^2-k_{zm}^2}dk_z$$

For the second integral a similar procedure is performed. With the same change of variable:

$$\frac{k_zh}{2}=x, \frac{dx}{dk_z}=h/2, dk_z=\frac{2}{h}dx$$

Which results in:

$$\frac{2}{h}\int_{-\infty}^{\infty}\frac{J_1^2\left(x\right)}{\left(-\frac{4}{h^2}\right)\left(x^2+\frac{h^2}{4}\left(k_{xm}^2+k_{ym}^2-k_0^2\right)\right)}dx$$

Introducing the same variable $K=\frac{h^2}{4}\left(k_{xm}^2+k_{ym}^2-k_0^2\right)$ an expression for the integral is found:

$$-\frac{h}{2}\int_{-\infty}^{\infty}\frac{J_1^2(x)}{x^2+k^2}dx = -\frac{h}{2}\left[-\pi\sqrt{\frac{1}{K^2}}I_1(K)^2+\frac{8\,_2F_3(1,1;1/2,3/2,5/2;K^2)}{3\pi}\right]$$

This integral has the same limitation as the first integral, so: $\Re(K^2) > 0 \vee K^2 \notin \mathbb{R}$.

The total integral Combining the two integrals with $K = \frac{h^2}{4}\left(k_{xm}^2 + k_{ym}^2 - k_0^2\right)$:

$$
j\frac{4\zeta}{k_0 h^2}\left(k_0^2 \int_{-\infty}^{\infty} \frac{J_1^2\left(\frac{k_z h}{2}\right)}{k_z^2\left(k_0^2 - k_{xm}^2 - k_{ym}^2 - k_{zm}^2\right)} dk_z - \int_{-\infty}^{\infty}\frac{J_1^2\left(\frac{k_z h}{2}\right)}{k_0^2 - k_{xm}^2 - k_{ym}^2 - k_{zm}^2} dk_z\right) =
$$

$$
-j\frac{h\zeta k_0}{2}\left[\pi\left(\frac{1}{K^2}\right)^{3/2}I_1(K)^2 - \frac{64\,_2F_3(1,2;3/2,5/2,7/2;K^2)}{45\pi}\right]
$$

$$
+j\frac{2\zeta}{k_0 h}\left[-\pi\sqrt{\frac{1}{K^2}}I_1(K)^2 + \frac{8\,_2F_3(1,1;1/2,3/2,5/2;K^2)}{3\pi}\right]
$$

The complete integral with accounting for all terms with $m_x \neq 0$ and $m_y \neq 0$ is given by:

$$
\int_{-\infty}^{\infty} B(k_z)B(-k_z)G_{zz}(k_{xm}, k_{ym}, k_z)dk_z =
$$

$$
\left(-j\frac{h\zeta k_0}{2}\left[\pi\left(\frac{1}{K^2}\right)^{3/2}I_1(K)^2 - \frac{64\,_2F_3(1,2;3/2,5/2,7/2;K^2)}{45\pi}\right]\right.
$$

$$
+j\frac{2\zeta}{k_0 h}\left[-\pi\sqrt{\frac{1}{K^2}}I_1(K)^2 + \frac{8\,_2F_3(1,1;1/2,3/2,5/2;K^2)}{3\pi}\right]
$$

$$
2a\left(\cos\left(\frac{k_x a}{2}\right)\operatorname{sinc}\left(\frac{k_y a}{2}\right) + \cos\left(\frac{k_y a}{2}\right)\operatorname{sinc}\left(\frac{k_x a}{2}\right)\right)
$$

Appendix D

Design parameters of the Unit cell design

In this appendix the simulation parameters of the slot and the ADL are presented. For the distance d_z the first and last value depict the additional space below and above the the first and last ADL of that section respectively.

D.1 Parameters of of Unit cell with ADL in Free Space

The unit cell simulated in CST has the parameters as shown in Tab. D.1.

Table D.1: Parameters of of Unit cell with ADL in Free Space

Parameter	Value
f_0	31 GHz
$d_x = d_y$	$0.45\lambda_0$
Slot and backing reflector	
w_{slot}	$1\ mm$
δ_{slot}	$3\ mm$
h_{back}	$0.25\lambda_0$
$\varepsilon_{r,back}$	1
ADL section 1	
p	$dx/3$
w	$[0.204, 0.102, 0.102, 0.102, 0.102, 0.102]\ mm$
s	$[0, 0, 0, 0, 0]\ mm$
d_z	$[0.1135, 0.227, 0.227, 0.227, 0.227, 0.227, 0.1135]\ mm$
ADL section 2	
p	$dx/3$
w	$[0.17, 0.17]\ mm$
s	$0\ mm$
d_z	$[0.65, 1.21, 0.65]\ mm$
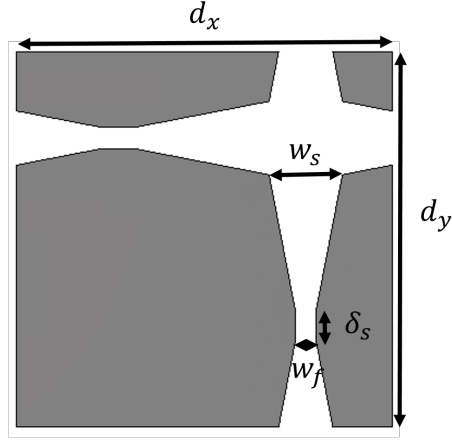
Figure D.1: Slot plane parameters for the dual polarized connected slot array.

D.2 Parameters of Unit Cell with ADL with Dielectric Layer

For the dual polarized unit cell, the slot parameters are defined as shown in Fig. D.1. All values of the parameters of the slot and the ADL are shown in Tab. D.2.

Table D.2: Simulation parameters of the dual polarized unit cell with ADL and a dielectric layer

Parameter	Value
f_0	31 GHz
$d_x = d_y$	$0.45\lambda_0$
Slot and backing reflector	
w_s	$0.85\ mm$
w_f	$0.25\ mm$
δ_s	$0.4\ mm$
h_{back}	$0.99\ mm$
$\varepsilon_{eff,back}$	± 1.7
ADL section 1	
p	$dx/3$
w	$[0.41, 0.205, 0.205, 0.205]\ mm$
s	$[0, 0.5, 0.5]\ mm$
d_z	$[0.17, 0.34, 0.34, 0.34, 0.17]\ mm$
ADL section 2	
p	$dx/3$
w	$[0.53, 0.53]\ mm$
s	$0.5p$
d_z	$[0.62, 1.24, 0.62]\ mm$

83

D.3 Parameters of Unit Cell using ADL with Dielectric Layers and Bonding layers

For the dual polarized unit cell with support and bonding layers the values of the parameters of the slot and the ADL are shown in Tab. D.3.

Table D.3: Parameters of Unit Cell using ADL with Dielectric Layers and Bonding layers

Parameter	Value
f_0	31 GHz
$d_x = d_y$	$0.45\lambda_0$
Slot and backing reflector	
w_s	$0.85 \ mm$
w_f	$0.25 \ mm$
δ_s	$0.4 \ mm$
h_{back}	$0.99 \ mm$
$\varepsilon_{eff,back}$	± 1.7
ADL section 1	
p	$dx/3$
w	$[0.41, 0.205, 0.205, 0.205] \ mm$
s	$[0, 0.5, 0.5] \ mm$
d_z	$[0.17, 0.34, 0.34, 0.34, 0.17] \ mm$
ADL section 2	
p	$dx/3$
w	$[0.53, 0.53] \ mm$
s	$0.5p$
d_z	$[0.62, 1.24, 0.62] \ mm$

D.4 Parameters of Unit Cell Using Four ADL with Dielectric Layers and Bonding layers

For the dual polarized unit cell with support and bonding layers the values of the parameters of the slot and the ADL are shown in Tab. D.4.

Table D.4: Parameters of Unit Cell Using Four ADLs with Dielectric Layers and Bonding layers

Parameter	Value
f_0	31 GHz
$d_x = d_y$	$0.45\lambda_0$
Slot and backing reflector	
w_s	$1\ mm$
w_f	$0.2\ mm$
δ_s	$0.2\ mm$
h_{back}	$0.99\ mm$
$\varepsilon_{eff,back}$	± 1.7
ADL section 1	
p	$dx/3$
w	$[0.2, 0.1]\ mm$
s	$0\ mm$
d_z	$[0.5, 0.254, 0.82]\ mm$
ADL section 2	
p	$dx/3$
w	$[0.53, 0.53]\ mm$
s	$0.5p$
d_z	$[0.73, 1.46, 0.73]\ mm$

List of Figures

List of Tables